Robert Winkler, Mag.art. BSc

Implications of Precursor Dynamics on Nanostructures during Focused Electron Beam Induced Deposition

MASTER THESIS

For obtaining the academic degree
Diplom-Ingenieur

Master Programme of
Technical Physics

Graz University of Technology

Supervisor:

Ao.-Univ.-Prof. Dipl.-Ing. Dr. techn. Werner Grogger

Institute of Electron Microscopy and Nanoanalysis

Co-Supervisor:

Dipl.-Ing. Dr. techn. Harald Plank

Graz, December 2013

Abstract

Focused electron beam induced deposition (**FEBID**) is a clever direct-write tool for the fabrication of functional nanostructures. A diverse range of novel application concepts have been demonstrated by taking advantage of the achievable reduced length scales as well as chemical and / or structural peculiarities of FEBID deposits. However, to provide reproducibility and high-fidelity shapes on the nanoscale, one has to consider and control an enormous number of parameters.

This thesis investigates the influence of molecular gas dynamics on the deposition process. In particular, a directional gas flux component is found, caused by the geometrical setup which influences the surface dynamics in a first and the deposit shape in a second step. By comparing different patterning strategies, beam parameters and gas flux situations, the influences of surface diffusion and direct adsorption from the gas phase could successfully be separated. This, in turn, allowed to reveal a geometrical shadowing effect on the nanoscale which can strongly disrupt the intended morphology. The experimental results were complemented by dynamic simulations of the growth process and by numerical calculations concerning the diffusion behaviour.

After understanding the gas dynamic effects, the influences from different patterning strategies were investigated which revealed different types of surface shapes in dependency on the local balance between precursor molecules and potentially dissociating electrons. Based on these findings, counterstrategies were successfully developed to improve the shape performance of FEBID structures.

In a final step, we used the gained knowledge to fabricate free standing 3D nano-architectures in a direct write manner to demonstrate the capabilities of focused electron beam induced deposition on the nanoscale.

Kurzfassung

Fokussierte Elektronenstrahl induzierte Abscheidung (focused electron beam induced deposition, **FEBID**) ist ein raffiniertes direktes Schreib-Werkzeug, um Nanostrukturen herzustellen. Eine vielfältige Palette neuartiger Anwendungen wurde mittlerweile demonstriert, indem die Vorzüge der erreichbaren reduzierten Längenskala als auch der chemischen und / oder strukturellen Besonderheiten von FEBID-Abscheidungen ausgenützt werden. Allerdings müssen eine enorme Zahl an Faktoren berücksichtigt und kontrolliert werden, um Reproduzierbarkeit zu gewährleisten und ein zuverlässiges Formverhalten zu erzielen.

Diese Diplomarbeit untersucht die Einflüsse der molekularen Gasdynamik auf den Abscheidungsprozess. Im speziellen wurde eine, durch den geometrischen Aufbau bedingte, gerichtete Gasfluss-Komponente gefunden, welche in einem ersten Schritt die Oberflächendynamik und in weiterer Folge die Abscheidungsform beeinflusst. Indem unterschiedliche Scan-Strategien, Strahlparameter und Gasfluss-Verhältnisse verglichen wurden, konnten die Einflüsse der Oberflächendiffusion und der direkten Adsorption aus der Gasphase erfolgreich voneinander getrennt werden. Das wiederum erlaubte es, einen geometrischen Schatteneffekt im Nanometermaßstab aufzuzeigen, der die beabsichtigte Morphologie total zerstören kann. Die experimentellen Ergebnisse wurden durch dynamische Simulationen des Wachstumsprozess und durch numerische Berechnungen die Diffusionsparameter betreffend ergänzt.

Nach der Analyse der Effekte durch die Gasdynamik wurden die Einflüsse unterschiedlicher Scan-Strategien untersucht, was, in Abhängigkeit von der lokalen Balance zwischen Precursor-Molekülen und potentiellen spaltenden Elektronen, unterschiedliche Arten an Oberflächenformen aufzeigte. Basierend auf diesen Ergebnissen wurden erfolgreiche Gegenstrategien entwickelt, um das Formverhalten von FEBID-Strukturen zu verbessern.

In einem letzten Schritt wurde das erlangte Wissen ausgenützt, um freistehende 3D Nano-Architekturen in direkter Schreibweise herzustellen, was die Leistungsfähigkeit der Technik der fokussierten Elektronenstrahl induzierten Abscheidung auf der Nanoskala demonstriert.

Acknowledgements

My sincere thank goes to all the persons, which were supporting me during my thesis. In first place I want to thank Prof. Dr. Ferdinand Hofer as the head of our institute for giving me the opportunity to write this thesis.

I want to express my gratitude to Prof. Dr. Werner Grogger for being my supervisor and his trust in this project.

My heartfelt thank goes to Dr. Harald Plank, my co-supervisor, not only for the amazing scientific support, but especially for the personal engagement and enthusiasm, for trusting and motivating me and making my work at the institute to such a joyful experience.

My colleagues at the FELMI-ZFE are responsible for a delightful atmosphere, so it was a pleasure to work together. In particular I want to thank the members of the workgroup S³ for integrating me not only in their group, but also in their lives.

I would like to express a special thanks to Dr. Christian Gspan and DI Roland Schmied, who have bad luck, to be my roommates at the institute. They were my first place to go for all small or tricky problems and I really appreciate their help. In the same context I want to thank DI Angelina Orthacker for her permanently help and for providing her smart interlacing engine.

My gratitude also goes to those persons, who supporting me at the dual beam and atomic force microscope, namely Martina Dienstleder, DI Thomas Ganner, DI Roland Schmied, Martin Stermitz and Sebastian Rauch.

A great thank I want to send to our partners at the EMPA (Swiss Federal Laboratories for Materials Science and Technology, Thun), Aleksandra Szkudlarek and Dr. Ivo Utke for the calculations concerning diffusion parameters and to Dr. Jason Fowlkes and Prof. Dr. Philip Rack (Oak Ridge National Laboratory and University of Tennessee) for the great growth simulations.

At last, I want to dedicate this work to my family. Their permanently support, patience and love made it possible at all.

Table of Contents

List of abbreviations

AFM	…	*atomic force microscope*
BPP	…	*bulk patterning point*
BSE	…	*back scattered electrons*
CPP	…	*corner patterning point*
DBM	…	*dual beam microscope*
DE	…	*diffusion enhanced*
DRR	…	*deposit related replenishment*
DT	…	*dwell time*
EPP	…	*edge patterning point*
ETD	…	*Everhart Thornley detector*
FEBID	…	*focused electron beam induced deposition*
FEG	…	*field emission gun*
FIB	…	*focused ion beam*
FIBID	…	*Focused ion beam induced deposition*
FSA	…	*fast scan axis*
FWHM	…	*full width at half maximum*
GFR	…	*gas flux replenishment*
GFS	…	*gas flux simulation*
IL	…	*interlacing*
ILD	…	*interlacing distance*
MTL	…	*mass transport limited*

PE	…	*primary electrons*
PoP	…	*point pitch*
PSD	…	*position sensitive detector*
RRL	…	*reaction rate limited*
RT	…	*refresh time*
SE	…	*secondary electrons*
SEM	…	*scanning electron microscopy*
SDR	…	*Surface diffusion replenishment*
SI	…	*spiral-in*
SO	…	*spiral-out*
SP	…	*serpentine*
SRR	…	*surface related replenishment*
SSA	…	*slow scan axis*
TEM	…	*transmission electron microscopy*
TET	…	*total exposure time*
TLD	…	*through the lens detector*
UHV	…	*ultra high vacuum*

1 Introduction and Motivation

An ongoing main trend in science and technology is the downscaling of structure sizes. Miniaturization of electronic devices is of great interest in order to enhance efficiency, computing power and integration density. However, as the objects get smaller and smaller, new techniques are necessary which are capable to reliably produce the desired structures. This, in turn, entails challenges during fabrication since effects which are negligible for macroscopic structures but can be significant on nanoscale.

A novel and increasingly important technique is focused electron beam induced deposition (**FEBID**), which utilize a finely focused electron beam to produce structures on the sub-10 nm scale[1,2] by the local dissociation of physisorbed precursor molecules from the gas phase. A big advantage to other nanotechnologies is the maskless direct write character even on non-flat surfaces without pre- or post-treatments (e.g. with photoresists). Furthermore, varying the precursor gases enable different functionality of the deposited (nano)structures (e.g. conductive, semi-conducting, insulating, magnetic, …) allowing a variety of applications from optical[3] towards mechanical or gas sensing[4] applications.

However, there are still some disadvantages and problems to solve. At the moment, the deposition speed with FEBID cannot compete with other nanotechnologies that are used for industrial production. Another problem is the partly poor purity of the deposited material, which restricts the functionality.[5] To solve this disadvantage, a lot of work is in progress even at our institute, ranging from fundamental issues like purification or new precursor materials towards the development of new application concepts.

Another problem is the missing high-fidelity on the nanoscale which can be the knock-out criteria for e.g. optical applications like plasmonic filters. Preliminary work at the FELMI comprised proximity effects of single lines[6] which broaden the desired structures as complex interplay of electron behaviour in solids and molecular dynamics on the substrate surface. As a next step, this master thesis focuses on shape performance of 3D deposits as required for most of the potential applications. Although a lot of work has been done during the last decade, many fundamental issues are not understood yet due to the enormous number of influencing factors. This thesis examines the effects of the gas dynamics during FEBID and its nanoscale consequences on the growth modes. The results are supported by calculations and simulations from our partners at the EMPA (Switzerland) and the Oak Ridge National Laboratories (USA).

2 Instrumentation

2.1 Dual Beam microscope

2.1.1 Components

A dual beam microscope (**DBM**) combines a scanning electron microscope (**SEM**) and a focused ion beam microscope (**FIB**) within one device. An additional value of this alliance is the simultaneous usage of an imaging technique (SEM) during the sputtering process with the FIB. For this reason, both particle beams have to be focused on the same spot on the surface (0).

The FIB is most frequently used to fabricate thin lamellas (< 50 nm) from a selected specimen area for **TEM** investigations. To transfer the lamella to a TEM-grid, it has to be lifted out and glued to the grid. For this purpose, gas injection systems (**GIS**) and a micromanipulator are installed.

With the GIS, it is possible to use the DBM for the deposition of material. This technique was utilized for the experimental part of the thesis. When the ion beam is employed to dissociate the injected precursor gas, one speaks of **FIBID** (Focused Ion Beam Induced Deposition), in case of the electron beam it is called **FEBID** (Focused Electron Beam Induced Deposition).

Figure 1 shows the main components of the DBM at the FELMI. As this thesis does not use the ion beam at any point, we will reduce a detailed description to the contributing components.
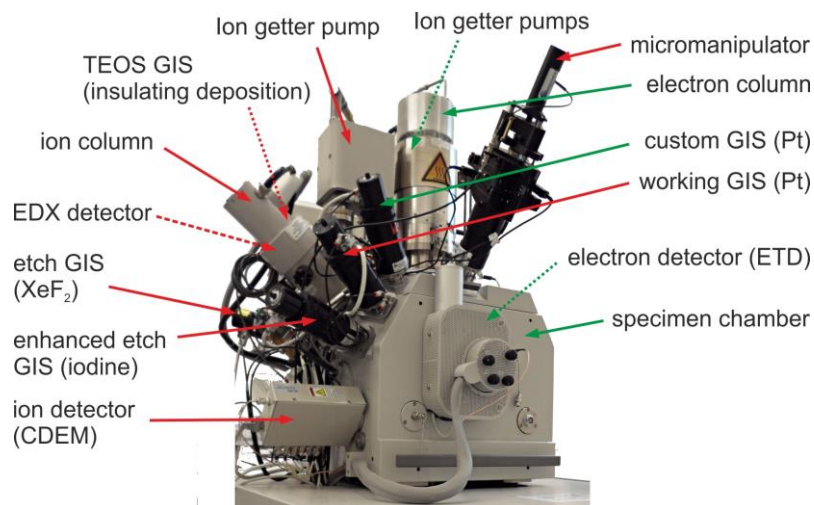

Figure 1: dual beam microscope (FIB Nova 200, FEI company) at the FELMI-ZFE. The green arrows illustrate components used for this thesis, dashed arrows indicate the position of components not visible in the picture. Ion column and electron column include an angle of 52°. The vacuum in the specimen chamber is provided by roughing pumps and a turbomolecular pump. Ion getter pumps generate enhanced vacuum in the columns. For detection of interaction products, a CDEM detector (ions), an ETD (electrons), a TLD (electrons) and an EDX-detector (X-rays) are available. For deposition and etching purpose, five gas injection systems with different gas types are integrated. With the help of micromanipulator, mechanical and electrical interaction with the sample is possible.

Eucentric height: the ion beam and the electron beam are focused at a certain spot. The user has to move the specimen surface to exactly this point in order to work in focus with both beams. This working distance is termed eucentric height, which is the distance between the pol piece of the last lens of the electron column and the specimen.[7]

At our system the working distance is about 5 mm. On the one hand side a smaller working distance would be more beneficial for the resolution, on the other hand there has to be space for GIS, micromanipulator and detectors as well.[8]

When the eucentric height is aligned correctly, the custom GIS, which has been used throughout the experiments has a distance to the surface of about 180 μm.

2.1.2   Vacuum system

To avoid scattering of electrons and ions at gas molecules in the chamber and to reduce contaminations on the surface, high vacuum is necessary.[7] As some components need even an ultrahigh vacuum (electron source and ion source), there are different vacuum pumps to provide the necessary pressure levels.

For the evacuation of the electron column and ion column, ion getter pumps are applied (Figure 1). The vacuum for the chamber is initially produced by roughing pumps, and after a reduced pressure is reached supported by a turbomolecular pump. A Penning-Pirani vacuum-meter measures the pressure about the principle of changing thermal conductivity with the number of gas molecules.

The chamber pressure for the experiments was about 10^{-5} mbar with open gas valves.

2.1.3   Scanning electron microscopy

Optical microscopes have the drawback of a limited resolution due to the limited wavelength. As electrons can be described as waves as well, their wavelength can get very small. The De Broglie-wavelength λ depends on the acceleration voltage U, the mass of the electron m (which has to be relativistic corrected for very high voltages), the electron charge q and the Planck constant h[9]:

$$\lambda = \frac{h}{\sqrt{2qmU}}$$

Usually, acceleration voltages up to 30 kV are applied, therefore the theoretical wavelength is only about 7 pm. Practically the final resolution is much worse due to lens errors.

Figure 2 shows the way of the electrons through the column schematically. The main components (source, lenses and detectors) will be discussed in the following chapters.
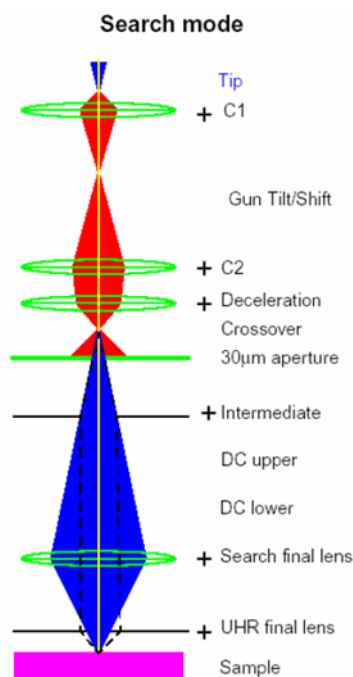
Figure 2: electron column of the used DBM. A tip emits electrons, these are focused with a system of lenses on the sample. For the ultra high-resolution mode (UHR) an additional lens (UHR final lens) is switched on. Above the objective lens (search final lens) two sets of deflection coils are arranged pairwise. They enable scanning of a sample area.[10]

2.1.3.1   Electron source

Three concepts for electron emitters are possible, each of them beneficial for different requirements. _Thermionic emitter:_ a tungsten filament or LaB_6-crystal is heated up and by that the work function energy barrier is overcome, so the electrons can escape the tip. This source has low demands concerning vacuum and provides the highest currents but with the drawbacks of low brightness, large energy spread and short lifetime.[7]

Cold field emitter: when a high voltage (about 10 V/nm) is applied to a tip with a very fine radius, electrons are emitted due to quantum mechanical tunnelling. Field emission guns (**FEG**) have the highest brightness and smallest probe size, and therefore the best resolution is possible. However, the cold emitter is not as stable as other emitters. The beam current is limited and a higher vacuum is necessary.[7]

Schottky emitter: in a Schottky emitter both mechanism are used: an electrical field reduces the work function, additionally the source is heated and electrons can overcome the potential walls. A ZrO_2 coating further reduces the work function to 2.7 eV.[11] A good brightness and source diameter are achieved and the relative high beam current is very stable in comparison to a cold FEG.[7] Our DBM is equipped with such a Schottky emitter.

2.1.3.2 Electron lenses

As described in 2.1.3, the wavelength does not limit the achievable resolution. Unfortunately, lens aberrations determine the final resolution so that the spot size is only a few nm (Figure 3). The most important lens errors are the spherical aberration, chromatic aberration and astigmatism. The latter can be corrected with a set of octupole lenses.[7]
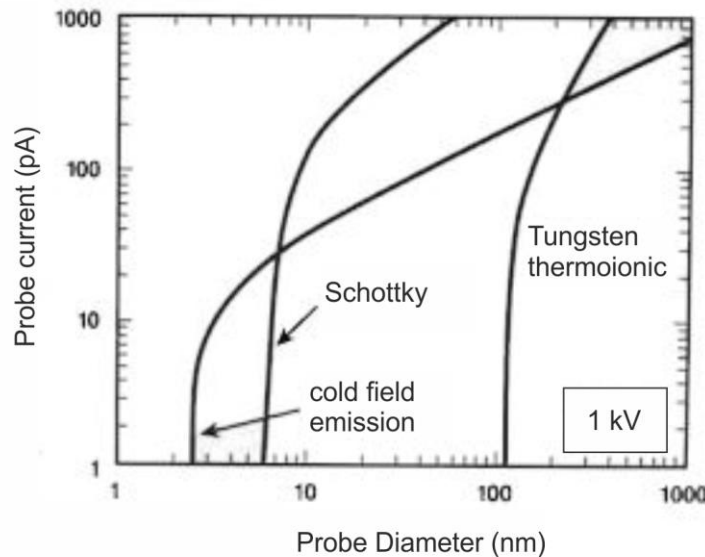

Figure 3: probe diameter as function of the probe current at an acceleration voltage of 1 kV for different types of electron sources.[7]

To reduce the source diameter, magnetic lenses are used. In a magnetic field, the Lorentz force acts on the electrons and affects their trajectories. In a SEM, several lenses and apertures are available (Figure 2). In contrast to optical lenses, the strength of an electrostatic lens can be adjusted continuously by changing the current through the coils.

2.1.4 Interaction of electrons with matter

When a primary electron (**PE**) hits the surface, it interacts with the specimen atoms in several possible ways.

Electrons that are scattered elastically in great angles can exit the surface again. They are called backscattered electrons (**BSE**) and have energies up to the primary energy.

For inelastic scattering the electrons are deflected in small angles and lose portions of energy until they are stopped in a maximum depth called the penetration depth. The penetration depth strongly depends on the atomic number and the primary energy of the electrons.[7] Figure 4 shows Monte Carlo simulations of the electron trajectories for two different materials used in this thesis.
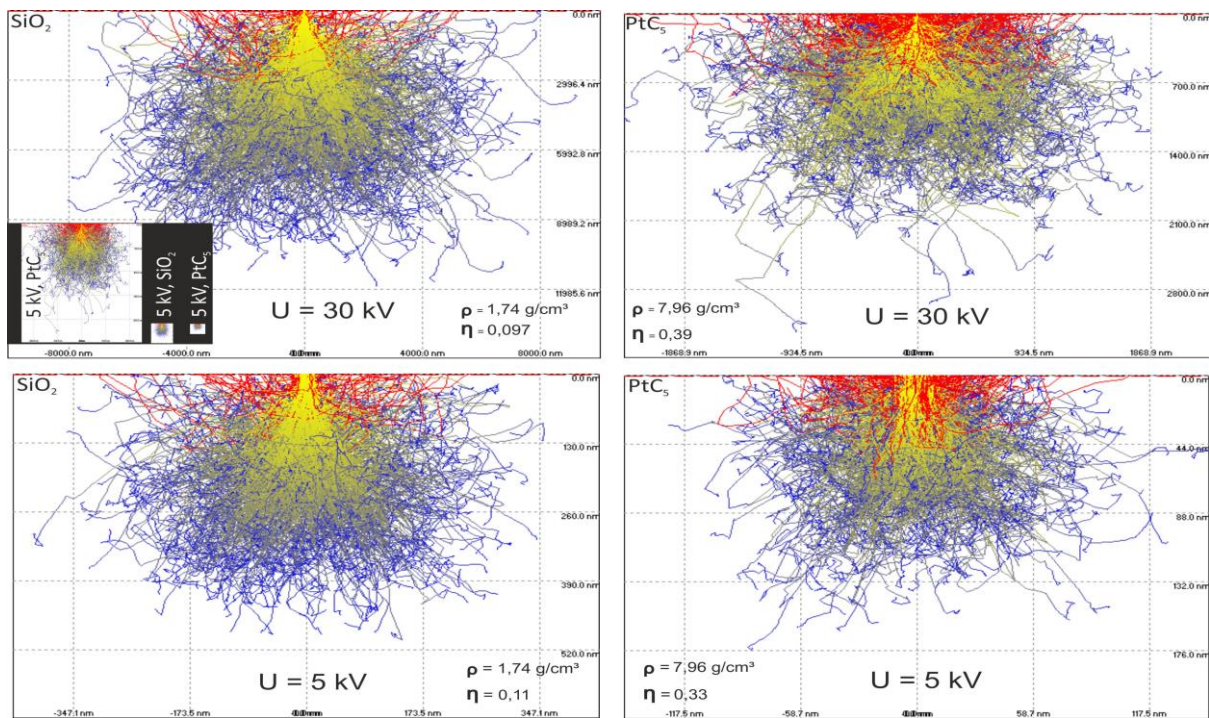
Figure 4: simulated trajectories[12] for different substrate material: SiO₂ (left) and PtC₅ (right) at acceleration voltages of 30 kV (top) and 5 kV (bottom). The yellow trajectories indicate electrons with high energies, electrons, which finally lost all energy within the bulk are shown blue. Electrons that left the surface again (BSE) are displayed red. The ratio between BSE and PE is called backscattering coefficient η. η and the density ρ are also shown for each situation. Please note the different length and depth scales for each picture; the insert (top left) shows the real size proportions of the three other cases in relation to the 30 kV, SiO₂ simulation.

On their way through the material, PE and BSE can lose energy by kicking out electrons of their atomic shells[7]. Secondary electrons (**SE**) origin from weakly bound electrons and can be generated by PE (in that case they are called **SE₁**), by BSE (→**SE₂**), or by forward scattered electrons (**FSE→SE₃**). SE are produced within the whole interaction volume, but due to their low energy (< 50 eV, see Figure 5) they are only detectable when their birthplace is close to the surface.

When an inner shell electron is kicked out, the atom gets in an excited state and two competitive mechanisms are possible to get rid of the released energy[7]: the first is the Auger process, where the energy is transmitted to an electron, which can leave the atom. This process is beneficial for lighter elements. The range of Auger electrons (**AE**) is rather short. The second mechanism is the generation of characteristic X-rays. Here the energy is emitted as a characteristic X-ray photon. Further effects are generation of electron/hole pairs in semiconductors, cathodoluminescence, X-ray bremsstrahlung and excitation of phonons.[13]
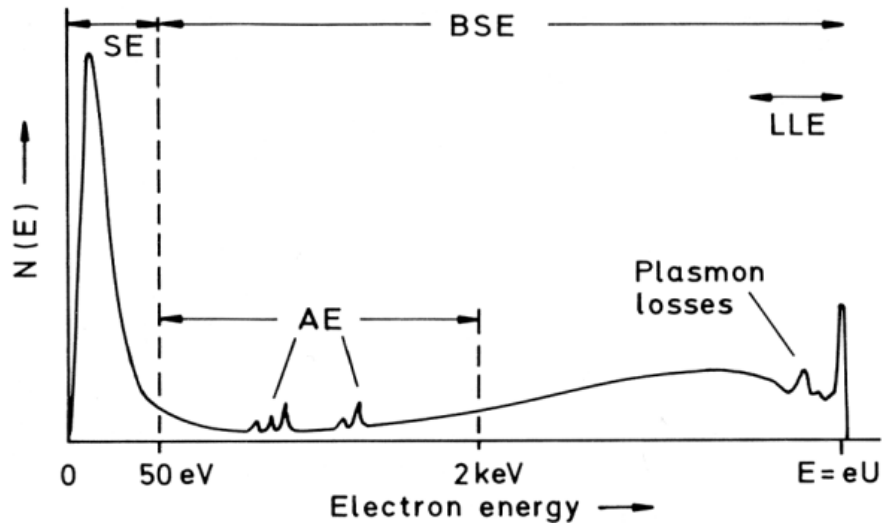
Figure 5: different kinds of electrons and their energies. Per definition electrons below 50 eV are called SE. Auger electrons (AE) have element specific energies. Low loss electrons (LLE) are BSE, which have lost only little energy (e.g. plasmon excitation).[13]

2.1.5 Detectors

As different signals origin from the interaction of particle with the specimen, different types of detectors are possible.

The generated X-rays can be collected energy dispersive (EDX-detector) or wavelength dispersive (WDX-detector), photons generated by a recombination of electron-hole pairs are evaluated with the cathodoluminescence – technique. These techniques enable a chemical analysis of the specimen.

When ions impinge on the surface, the sputtered material can be detected as well (SIMS, CDEM).

The most important signals arise from the electrons, which exit the specimen again. Several detector designs are possible, the following sections describe the two detector types of our DBM at the FELMI.

2.1.5.1 Everhart-Thornley detector

Our dual beam system uses an Everhart-Thornley detector (**ETD**) to capture electrons. When a low energy electron exits the surface, a biased collector grid affects it. By selecting a positive bias the grid attracts the electrons and especially the SE with low energy are sucked in. In contrast by using a negative bias, these low energy SE are repelled and only the high energetic BSE can overcome the applied potential barrier and enter the detector.[7]
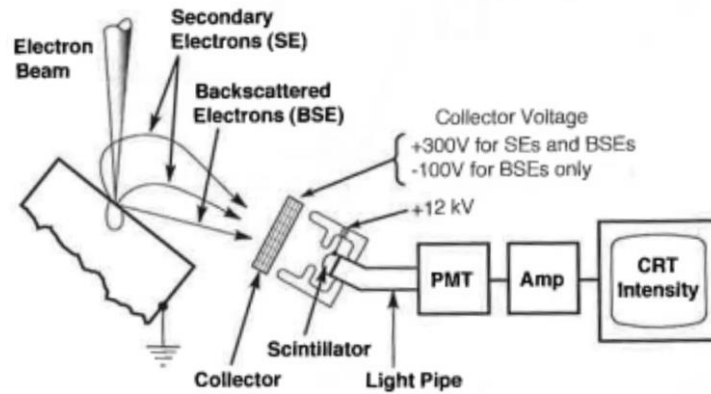
Figure 6: Everhart-Thornley detector for detecting electrons[7]

Once an electron has passed the grid it is strongly accelerated to a scintillator. There, one electron generates many electron-hole pairs. The recombination of these pairs produces photons. A light pipe conducts them onto a photocathode that generates typical 1-10 photoelectrons. A photomultiplier amplifies the number of photoelectrons and a comfortable signal can be measured.[7]

The ETD is tilted with respect to the specimen surface, therefore, for electrons which do not directly face the collector grid it is more difficult to reach the detector. This leads to a minor yield of SE coming from these areas (e.g. backside of a barrier), the resulting points get darker and according to our optical experiences a three-dimensional impression is given.[7]

2.1.5.2 *Through-the-lens detector (TLD)*

The through-the-lens detector (**TLD**) is located above the objective lens, so the SE coming from the specimen have to travel back through the objective lens to reach the detector. In order to get to the scintillator, a high positive bias (+10 kV)[7] is applied and the SE_1 and SE_2 are attracted. Due to the influence of the magnetic field in the objective lens they follow spiral trajectories.[7]

The BSE cannot reach the detector due to their quite uninfluenced straight trajectories. However, material contrast is still observable, due to the generation of SE_2 by BSE.[7]

2.2 Atomic force microscopy (AFM)

2.2.1 Working principle

Atomic Force Microscopy (**AFM**) is a surface sensitive scanning probe technique, with which even atomic resolution is possible.[14] A piezoelectric-based motion system brings a flexible cantilever with a thin tip at its end very close to the surface. In dependency of the distance to the surface attractive or repulsive forces are acting on the tip and lead to a bending of the cantilever. This bending can be measured optical or capacitive and converted into different properties (e.g. height, phase, conductivity) depending on the working mode.

2.2.1.1 Forces

When the tip approaches the surface, different forces are acting. In a distance greater than 10 nm the electrostatic and magnetic forces are dominating. Below 10 nm the Van-der-Waals force attracts the tip. Closer to the surface, a strong repulsive force due to the Pauli-principle prevents an overlap of the orbitals and a further approach of the tip.[15]

Most imaging modes of the AFM operate in a distance of 10 nm and below and the resulting potential is approximated by the Lennard-Jones potential (Figure 7, blue line):

$$V_{Lennard-Jones} = V_{repulsive} + V_{Van\,der\,Waals} = \frac{a}{r^{12}} - \frac{b}{r^6}$$

with the distance r to the surface and the constants a and b.[15]
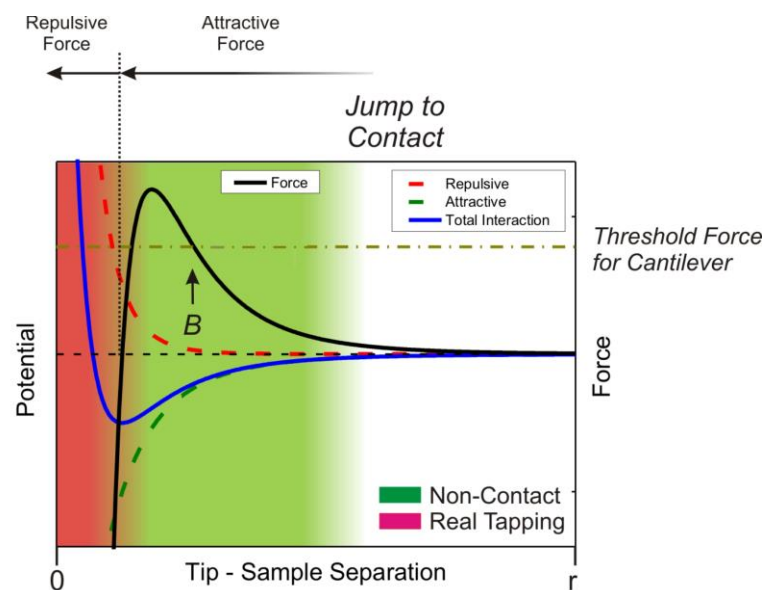

Figure 7: attractive forces (green line), repulsive forces (red line) and resulting potential (blue line, Lennard-Jones potential) in the AFM. The black curve shows the force on the tip: above the dashed black line, the force is attractive, below repulsive. The intersection point B of the force curve with the threshold force of the cantilever (green dot-dashed line) marks the jump to contact distance. For the non-contact mode the tip remains in the attractive force regime (green area), whereas for the contact and tapping mode the tip enters the repulsive regime as well (red area).[15]

2.2.2 Components

Figure 8 shows the used microscope (Dimension 3100 microscope, Bruker AXS) for the AFM-measurements. The most important component is the scan head, which is presented in more detail in Figure 9. The deflection of the cantilever is measured optically in this system by means of deflection of a laser beam on a position sensitive detector (**PSD**).
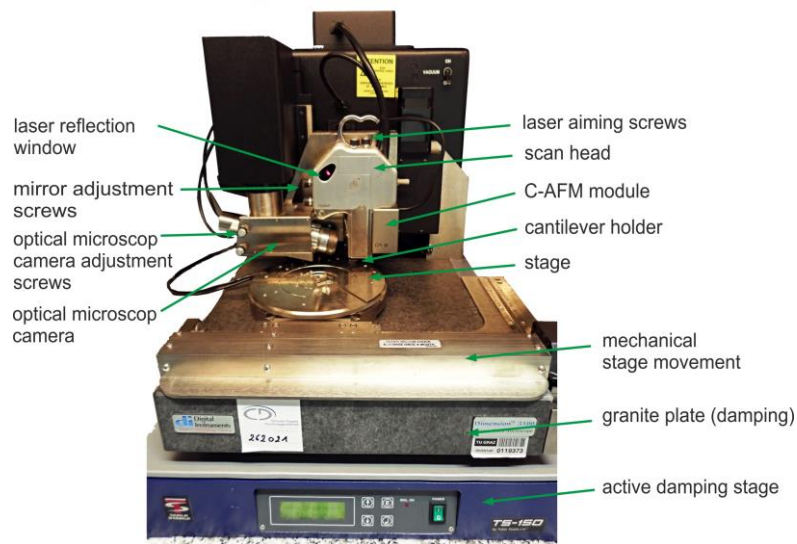
Figure 8: AFM (Dimension 3100 microscope, Bruker AXS, operated with a Nanoscope IVa controller and equipped with a XYZ Hybrid scan head). To avoid disturbing oscillations the system is built on a heavy granite plate and additionally damped with an active damping stage. For navigation on the sample a digital optical microscope is installed.
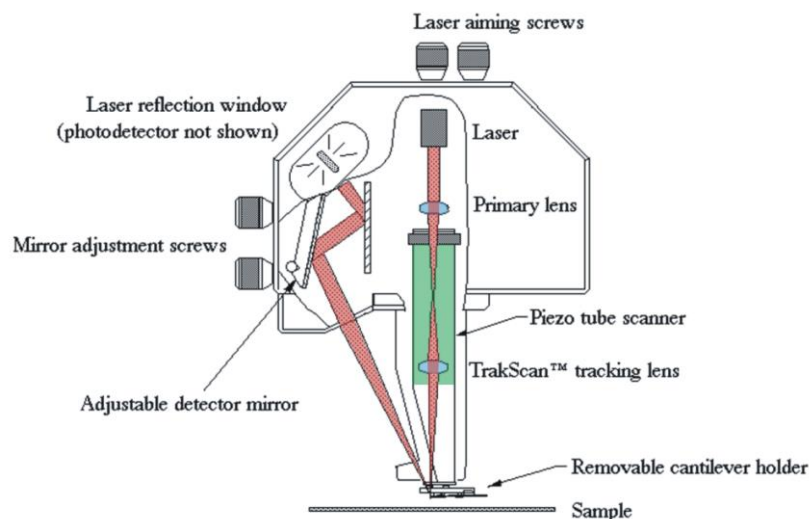

Figure 9: scan head in detail. A lens system focuses the laser beam on the cantilever. The user has to select the exact position with two laser aiming screws. Adjustable mirrors forward the reflected laser beam onto a position sensitive photo detector (PSD). When the cantilever is deflected due to surface forces, the laser spot is shifted to a different point on the PSD.[15]

2.2.2.1   Motion system

A mechanical stage enables a rough movement of the specimen to the measurement site (Figure 8). For a precise motion in the picometer range during the measurement, an accurate positioning system is essential. This is possible with piezoelectric crystals, which expand and contract, respectively when a bias is applied. A common construction type is a tube scanner presented in Figure 10.
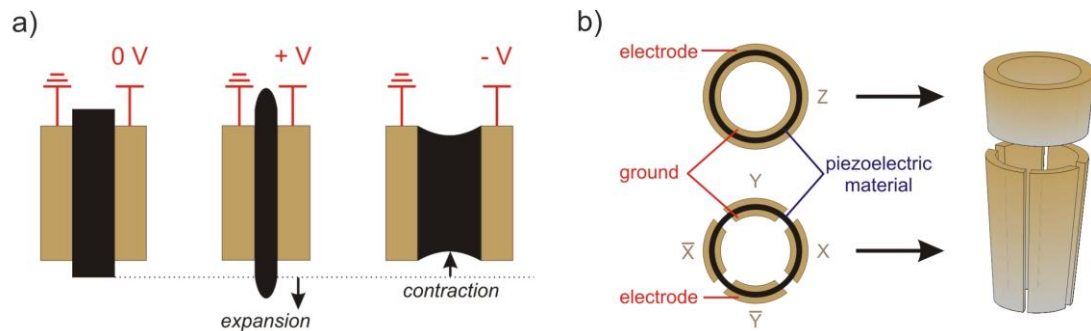
Figure 10: Principle of a tube scanner. Due to the piezoelectric effect, the tube is contracted and expanded, respectively when voltage is applied (a). There is a separate crystal for the height component, the movement in x and y-direction is coupled (b).[15]

2.2.2.2 Cantilever and tip

As seen before, different forces F are acting on the tip and bend the cantilever for a distance z. In this context the spring constant k of the cantilever is of main interest according to Hooke´s law (F = kz). There are many different cantilever types available, differing in spring constant, geometry, tip shape, material and functionality. Depending on the operating mode, different types of cantilever are required. Figure 11 shows one type of cantilever for tapping mode used for the experiments (Olympus OMCL TS-240, resonance frequency ~ 70 kHz), additionally Olympus OMCL TS-160 cantilever with a resonance frequency of about 330 kHz were utilized.
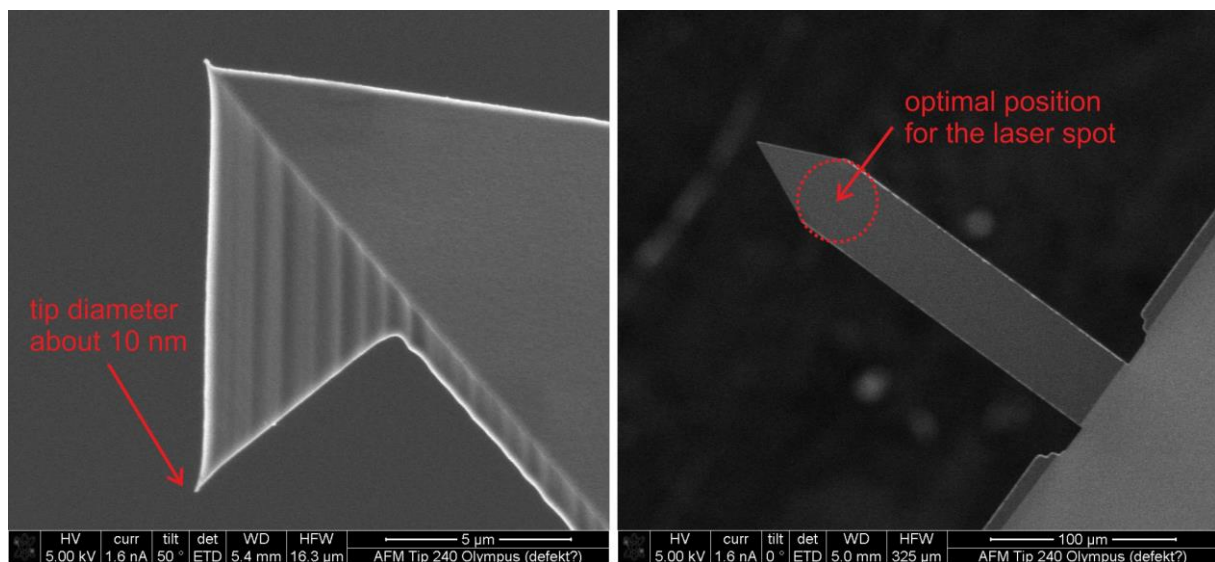

Figure 11: SEM image of a used tip (left, side view) on a cantilever (top view) Olympus OMCL TS-240. The laser spot should be positioned within the red dashed circle to enhance sensitivity.

Cantilevers for optical detection systems are covered with a high reflective layer. The cantilever itself is mounted on a removable cantilever holder (Figure 9).

As the final image is a convolution of the surface with the tip, the geometric tip shape strongly affects the possible resolution. Some tip related problems are shown in Figure 12.
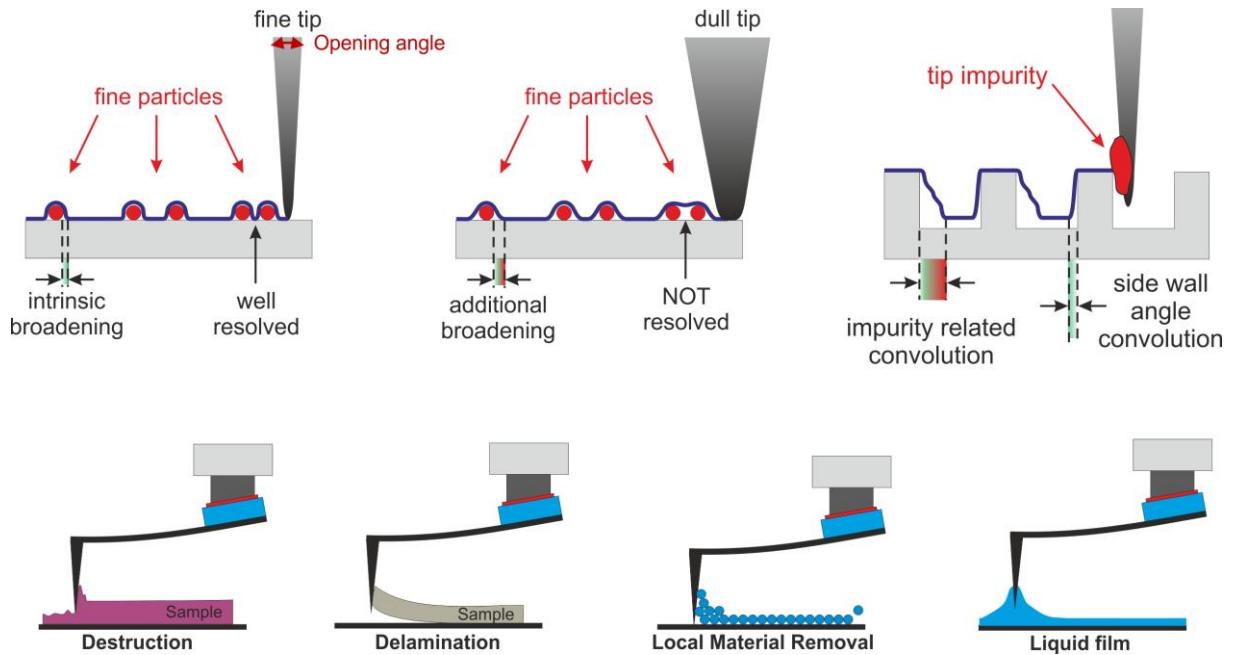

Figure 12: some possible problems during AFM measurements. Geometrical problems with dull or contaminated tips (top row) limit the resolution, especially for steep high sidewalls. Bottom row: possible unwanted impacts on and of the sample during the measurements in contact mode (destruction, delamination, local material removal) or in tapping mode (liquid film meniscus). [15]

2.2.3   Imaging modes

Numerous variants of imaging modes have been developed (constant height mode, constant force mode, intermittent mode, conductive AFM, chemical AFM, …), we will concentrate in the operating mode used for this thesis.

2.2.3.1   Tapping mode

For the tapping mode a piezoelectric crystal excites oscillations in the cantilever, so the tip periodically taps on the surface.[16] This operating mode is gentler to the surface, however problems with capillary forces due to a contamination liquid layers may occur (cf. Figure 12, bottom row).
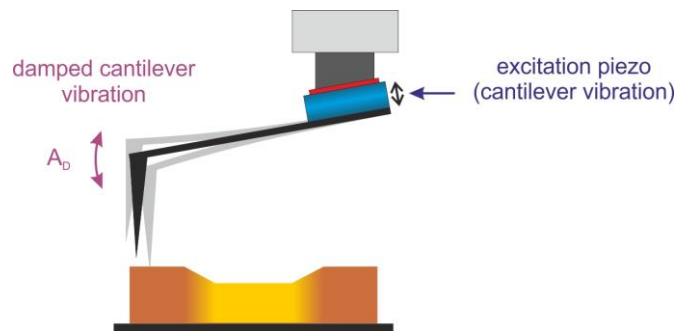
Figure 13: tapping mode. A piezoelectric crystal induces oscillations of the cantilever at its resonance frequency. The oscillation amplitude is damped when the surface is approached. Additionally the resonance frequency shifts and a phase lag occur.[15]

After an automatic tuning procedure, the cantilever oscillates with its resonance frequency. When the tip interacts with the surface related forces, two effects occur: First, the undisturbed amplitude is damped; and second, a phase lag between exciting oscillation and cantilever oscillation can be measured. From the first effect, height information can be achieved by adjusting the distance to the surface in such way that at any time the same amount of damping is provided. From the latter a phase image can be taken. As this phase shift also depends on the local surface material, a material contrast can be seen.[14,15]

3 FEBID

3.1 Concept

Focused electron beam induced deposition (**FEBID**) is a direct write technique in a SEM or a FIB, where an electron beam locally decomposes precursor molecules. The non-volatile parts stay on the surface and build up a deposit.

In principle, it is also possible to use ions to induce a dissociation of the precursor molecules. This technique is termed focused ion beam induced deposition (**FIBID**). The fundamental process is similar to FEBID, but the properties of the resulting deposits differs (e.g. volume growth rate, shape, resistivity). In terms of spatial resolution, FEBID is preferable.[17]
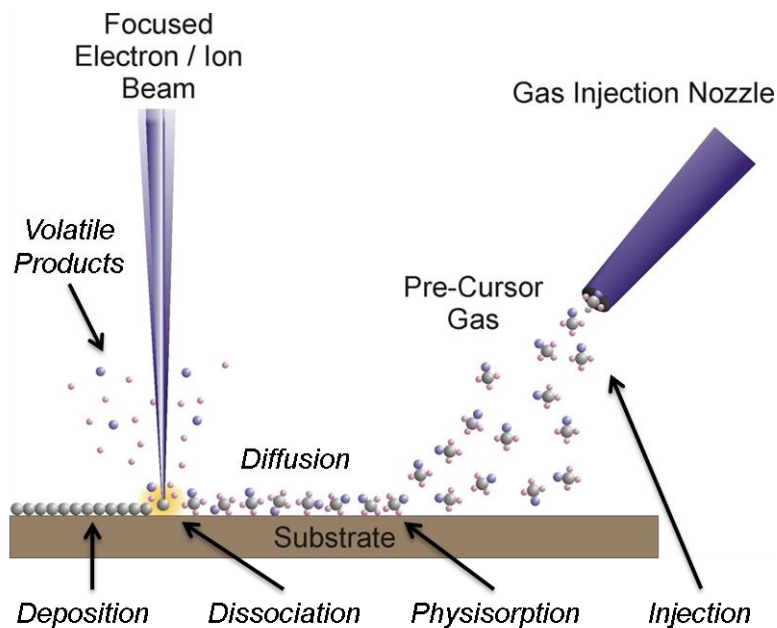
Figure 14: working principle of the FEBID/FIBID process.[15]

Figure 14 illustrates the steps of the deposition process: a nozzle of a gas injection system (**GIS**) is brought very closely to the surface and inserts permanently a special precursor gas. The gas molecules physisorb at the substrate, diffuse on the surface and desorb again after a mean residence time. When these adsorbed precursor molecules are exposed to electrons, they can be dissociated into volatile parts, which are pumped away by the vacuum system, and a non-volatile part, which are deposited on the surface.[17]

The main advantages of FEBID are the applicability to even non-flat surfaces down to the nanoscale without post treatment. The main disadvantages are the poor metal content of the deposit and the broadening of the structures.[18]

3.1.1 Dissociation mechanism

As mentioned before, the precursor molecules are dissociated because of the particle impingement. A closer look at the dissociation cross sections for different electron energies reveals, that most of the precursors are cracked up by electrons with an energy of a few eV[18], thus by SE. This process is called dissociative electron attachment (**DEA**). Depending on the used precursor complex incomplete decomposition takes place and only parts of the molecular groups are split off (Figure **16**).

For energies in the range of the ionisation energy, the dissociation mechanism is referred to dissociative ionisation (**DI**). However, due to the high number of SE in the range of 3 eV[7] the DEA mechanism dominates over the DI. The PE hardly contribute to the dissociation process as their dissociation cross section is too low.[17,19] The exact dissociation energies depend on the used precursor complex.

3.1.2 Working regime

A central term in discussion of FEBID processes is the working regime. It reflects the ratio between the number of dissociating electrons and precursor molecules as described in literature.[5,17,20,21] One can distinguish between two extreme conditions:

- Mass transport limited (**MTL**): In this working regime, more dissociating electrons than precursor molecules are available.
- Reaction rate limited (**RRL**): In contrast, in this working regime, more precursor molecules than electrons are present.

The diffusion enhanced (**DE**) regime condition is located in between MTL and RRL. In that working regime all molecules within the exposed beam spot are consumed, however molecules from the proximity can replenish the depletion by diffusion.

Depending on the working regime, different single dot shapes appear.[22] They are shown in Figure 33.

There are also strong indications, that the working regime influences the chemistry of the deposition.[5,17,23] Because of the lack of electrons in the RRL working regime, the precursor molecules are not fully dissociated. Many ligands remain on the central atom; therefore, the purity of the intended deposit suffers. In contrast, by the supplying MTL condition, the surplus electrons lead to a polymerization of the split-off-ligands and again unwanted fragments are integrated in the deposit. The purification of FEBID deposits is currently of main interest in the community[5,24-26] and topic of ongoing work at our institute.

3.1.3 Adsorption rate model

Theoretically, the adsorption rate model can describe the changing coverage of precursor molecules.[22,27] The number of adsorbates is given to the following equation, where the first term is related to the adsorbtion process (*s – sticking probability, J- molecular flux, n_0 – number of molecules in a complete monolayer*), the second to the desorbtion (*τ – average residence time of molecules*),

the third describes the decomposition (σ – *net cross section*, $f(r)$ – *beam distribution*) and the fourth the diffusive contributions (D – *surface diffusion coefficient*).

$$\frac{\partial n(r,t)}{\partial t} = sJ\left(1 - \frac{n(r,t)}{n_0}\right) - \frac{n(r,t)}{\tau} - \sigma f(r)n(r,t) + D\left(\frac{\partial^2 n(r,t)}{\partial r^2} + \frac{1}{r}\frac{\partial n(r,t)}{\partial r}\right)$$

The calculation of the surface diffusion coefficient D (see section 4.1.3.2) is of main interest for this thesis, as surface diffusion is an important part to describe the gas dynamics.

3.2 Applications

Due to the advantages of FEBID in comparison to other techniques (e.g. small deposit size, no restriction to flat surfaces, no post treatment necessary) several application have been developed, reaching from passive devices such as lithography-mask repair[28,29], advanced scanning probe microscopy probes[30,31], nano optics[3,32] towards active devices like strain sensor,[23,33] magneto-logic applications[34-37] or gas sensor, as recently developed at the FELMI.[4]

As a proper shape performance can be a knock-out criterion for further applications, it is necessary to get control of the morphology. This topic is one of the main challenges beside the purification and search for new precursor molecules.

3.3 Technical Setup

3.3.1 Gas injection system

For inserting different precursor gases, we have installed several gas injection systems (**GIS**) at our FIB Nova 200. A small reservoir of solid precursor material is heated up to its boiling point and the molecules can stream out through a nozzle when the gas valve is opened. To provide a high local coverage at the surface on the one hand side and stable vacuum conditions on the other hand at the same time, one has to bring the nozzle as close to the surface as possible. Therefore, the nozzle is inserted pneumatically to a pre-defined point in space. For a defined height above the specimen, the user has to lift the stage to the eucentric height (2.1.1).

Several nozzle types are available (Figure 15), in our DBM the GIS has a nozzle with the straight tube design.
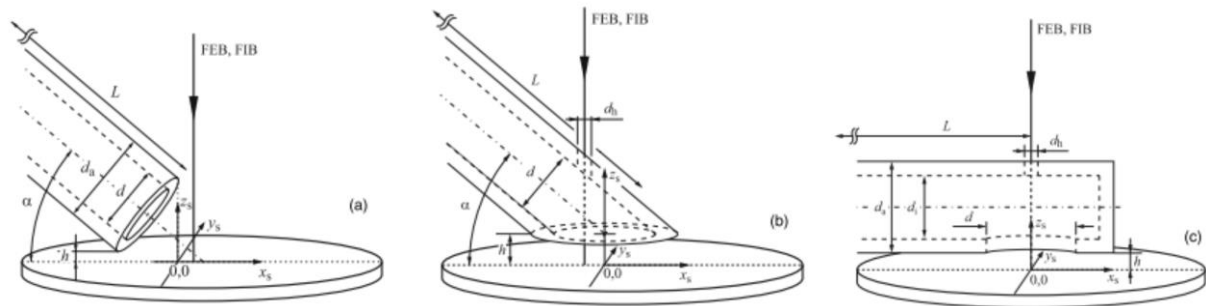
Figure 15: different gas nozzle types: a) straight tube nozzle; b) bevelled nozzle with entrance hole on the top; c) doubly perforated nozzle design with access and exit hole.[38]

The most important parameters for the alignment are the height h to the lower edge of the nozzle (180 μm at our system), the angle α (52 ° at our system) and the position of the deposition site. Latter is discussed in more detail in the result section. Other GIS related settings in our FIB are the outer and inner nozzle diameter (830 μm and 500 μm, respectively).

3.3.2 Precursor

In the meantime, many different precursor complexes are available. In most cases, they consist of hydrocarbons or other volatile groups attached to a central element (e.g. Pt, Au, Si, W, Fe).[39]

The demands on the precursors limit the number of possible materials for FEBID: First, the precursor has to physisorb at the surface well, further the complex should decompose completely under electron exposure and in addition, boiling point, toxicological and economical considerations play a role.[17] For most of the precursor compounds the second factor limits the purity, especially the carbon contamination is the main problem. Purification efforts and the usage of carbon-free precursors are in progress at our institute right now.

For our experiments we used a platinum based organic precursor namely trimethyl(methylcyclopentadienyl)-platinum(IV) (MeCpPt^{IV}Me$_3$). The GIS reservoir was heated up to 45 °C for at least 30 minutes before the open the gas valve.
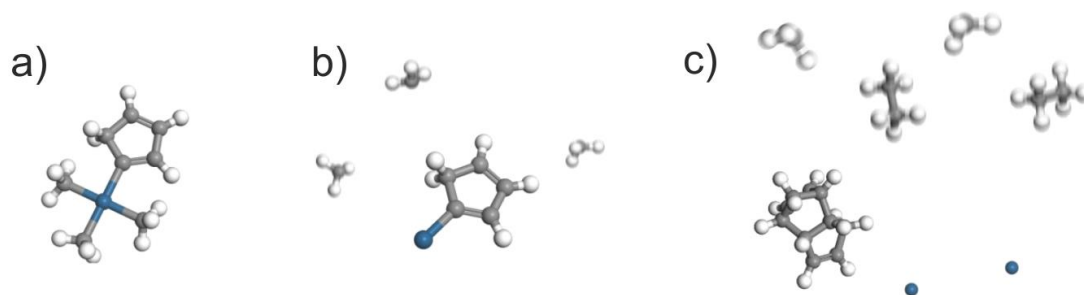

Figure 16: chemical structure of the used precursor molecule MeCpPt^{IV}Me$_3$ (a). Three CH3 groups and a cyclopentadienyl ring surround the central platinum atom (blue). In the most beneficial scenario, one electron detaches all groups from the central atom. Incomplete dissociation is typical for RRL conditions (b).

By providing more electrons (MTL), polymerization of the splintered ligands takes place (c). In both latter cases, this leads to an unwanted implantation of hydrocarbons to the deposit.[15]
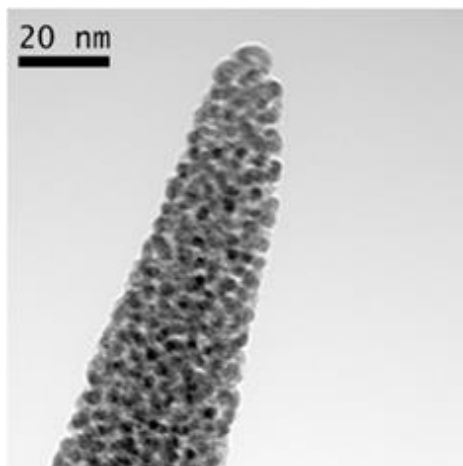

Figure 17: TEM bright field image of a typical FEBID deposit. The dark speckles are platinum grains embedded in a carbon matrix. The content of platinum is only 15 %.[40]

3.4 Patterning details

There are three possibilities to control the motion of the electron beam.

Patterning engine: the FIB Nova 200 has an integrated patterning program, with which defined shapes (rectangles, circles, lines and polygons) can be processed. Additional, the user has the possibility to select, among other parameters, the point pitch, dwell time per point, number of loops and refresh times in a very easy way.[41]

Bitmap: the FEI-patterning engine is also able to use uploaded bitmaps for processing. The bitmap must have the format of 24-bit in RGB-modus, where the value of the blue colour channel defines the dwell time (**DT**) for a pixel (starting from 0 linear to the selectable maximum dwell time for the blue-value maximum 255).[41]
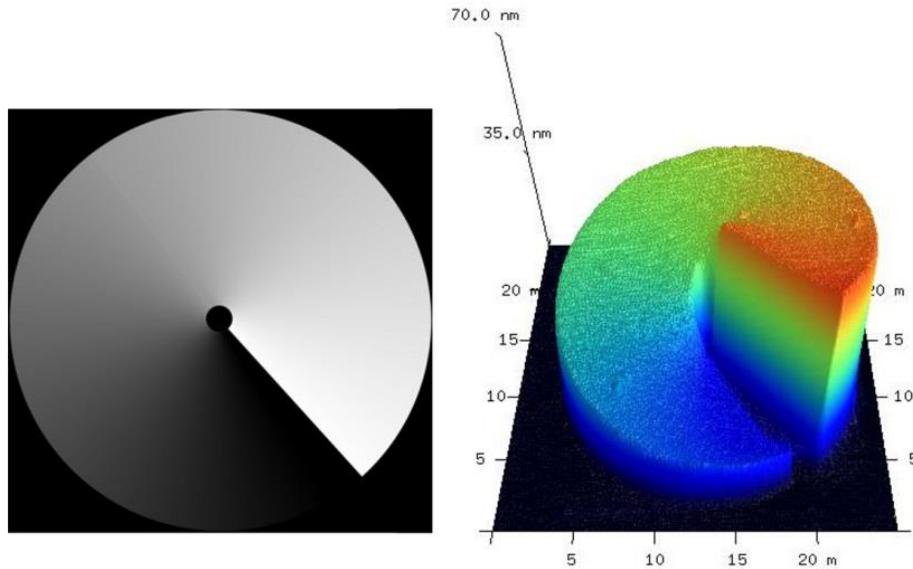
Figure 18: fabrication of a spiral phase plate for plasmonic TEM-investigations: Bitmap (left) and thereby fabricated deposit (right, AFM 3D-height-image).

1.) **Stream file:** the mentioned methods have the advantage to be very intuitive and relatively easy to use. However, they have the drawback, that the user is not able to customize the patterning especially when complex patterning is needed. In that case, it is necessary to use stream files.

A stream file is a text-file with the file extension "str" in which all information for the beam motion is embedded. One can simply manipulate the content (and therefore the beam movement) by open the stream file (e.g. with a text editor) and change the values.

The structure of a stream file is represented in the following[41]:

```
s16
1          ⎤
7          ⎦  header
1 0 0
250000 3952 4004
10000 65535 0
10000 4004 4056 0    ⎫ command lines
10000 4056 4056 1    ⎬
10000 4056 4004      ⎭
10000 4056 3952
```

The letter "s" in the first line defines the file as a stream file. The addition "16" is referred to the maximum pixel resolution (16 bit). In the second line, one can select the number of passes. The number in the third line indicates the number of following command lines and is restricted to 8 millions.[42]

The first column of the command lines belongs to the dwell time in unit of 0.1 µs. Maximum dwell time per pixel is limited to 25 ms (equates the number 250000 in the stream file). The second and the third column contain the pixel coordinates X and Y respectively. The forth column is optional and reserved for beam banking (value 0 = blanked beam, 1 = not blanked).[42]

3.4.1 Stream file generator

With the stream file method we are able to control the beam motion according to our own purpose.

For generating individual patterning strategies automatically, a console application has been written (C++, CodeBlocks 10.05).[43] The executable strategies are explained in the following section.

The translation from real dimensions into pixel is related to the magnification so one first has to know the used magnification during the experiments and the window size (maximized window/minimized window; switch with F5) before running the generator.

Please note the magnification couples with the screen resolution of the microscope display. Therefore, a set up of the stream file generator has to be done for every microscope individually.

Due to the apparently problems with the appropriate blanking of the electron beam a starting and endpoint respectively have been introduced. In our experiments they have the same pixel coordinates (X = 0; Y = 3536) and a dwell time of 0.1 µs. The position of starting/endpoint should be controlled before the usage, on the one hand side the point should not be inside of footprint area, neither too far away from the first patterning point due to the finite speed of the beam movement. As mentioned before (3.4) one can simply change their pixel coordinates to suitable values. If no starting or endpoint is needed, an extra generator is provided too.

There are several special patterning strategies realized with the stream file generator:

3.4.1.1 Raster

Figure 19 shows the patterning sequence of a raster strategy schematically.
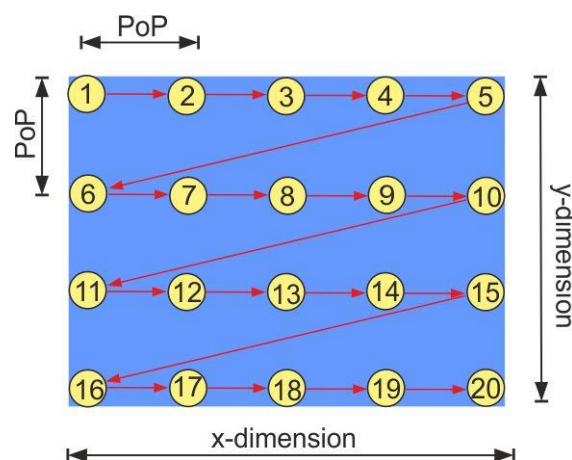

Figure 19: raster strategy. The numbers and the red arrows indicate the sequence of patterning.

The user can select the distance between two consecutive patterning points (Point pitch, **PoP**) and the dimension of the rectangle (X-dimension, Y-dimension).

In addition, there are two modes available for realizing the total exposure time (**TET**) per patterning point: 1) full beam, and 2) chopped beam. In the former case, the beam stays for the whole dwell time (DT, user input) at a patterning point.

In the chopped beam-modus the user can split the total exposure time into shorter time portions (DT). The electron beam illuminates a pixel for that dwell time, before proceeding to the next pattern point. To achieve the desired total exposure time, the beam jumps back to the beginning (20→1, see Figure 19). Depending on the ratio between dwell time and total exposure time there are several such loops required.

3.4.1.2   Serpentine
Figure 20 shows the patterning sequence for serpentine strategy schematically.
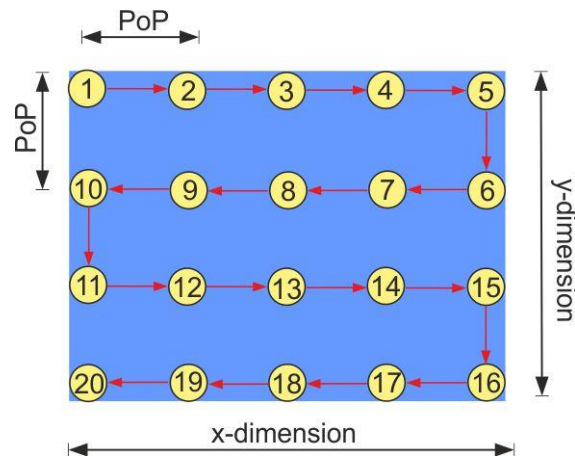
Figure 20: serpentine strategy (SP)

Similar to the raster strategy, the user select X- and Y-dimension and the point pitch. The full beam/chopped beam-modes are available too (as described above).

3.4.1.3   Interlacing
Figure 21 shows the patterning sequence for interlacing strategy in full beam modus schematically.

The interlacing strategies (**IL**) use a comparatively large distance (interlacing distance **ILD**) to consecutive patterning points. When one frame is finished (point 1-9 in Figure 21) the frame is shifted for one PoP in X-direction. After exposure of all patterning points within a line (point 27 in Figure 21) the interlacing frame starts from the beginning but is shifted in y-direction for one PoP.

Continuing this procedure, finally all patterning points are addressed and the same final point pitch as in the other strategies is achieved.
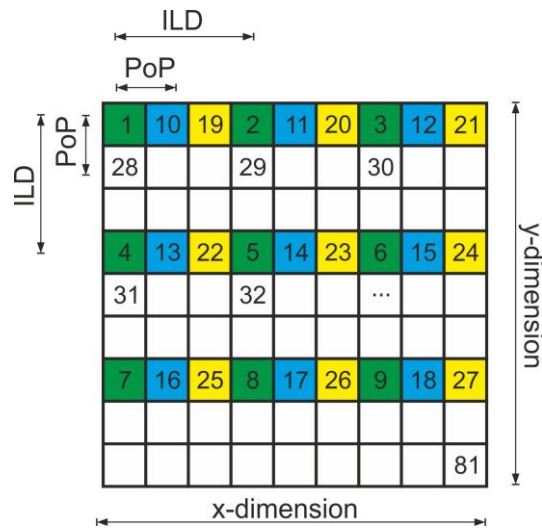
Figure 21: interlacing strategy (IL) with full beam (schematically). The numbers indicate the patterning sequence. Green squares belong to frame 1, blue and yellow squares to frame 2 and 3 respectively. The square with the number 81 indicates the last point of the interlacing pattern.[44]

In contrast to raster and serpentine strategy, there are two possibilities to perform a chopped beam modus with an interlacing strategy (see Figure 22):

- Serial interlacing: by performing several loops, the total exposure time for each point of one frame is achieved before proceeding to the next frame.
- Parallel interlacing: all points of the deposition footprint are exposed for one DT before proceeding to next loop.
-

Figure 22: Interlacing strategy in chopped modus: serial interlacing (left) and parallel interlacing (right). The numbers indicate the patterning sequence.[44]

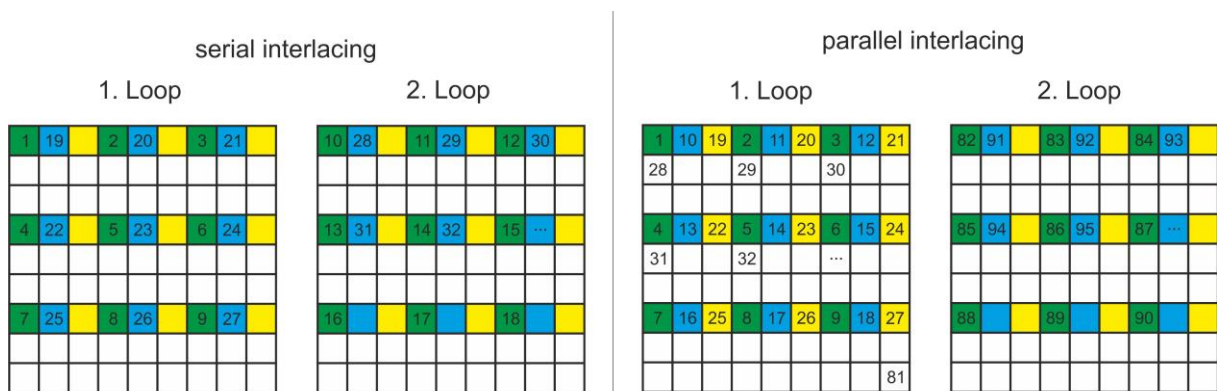It should be noted, that the interlacing distance has to be a multiply of the point pitch. In addition, the X- and Y-dimension have to be a multiply of the interlacing distance. Otherwise, the ratio is rounded down and the footprint gets smaller than intended. Orthacker et al.[45] have presented a generator that eliminates this problem (**SIL**-engine).

The interlacing approach is beneficial for e.g. milling of temperature sensitive materials[45] due to longer recovery times for the proximity of a patterning point. For FEBID, the surface has more time to replenish with precursor molecules by means of surface diffusion before the beam returns to the sector again.[5]

3.4.1.4 Spiral-inward (SI)

Figure 23 shows the patterning sequence for the spiral-inward strategy (**SI**).
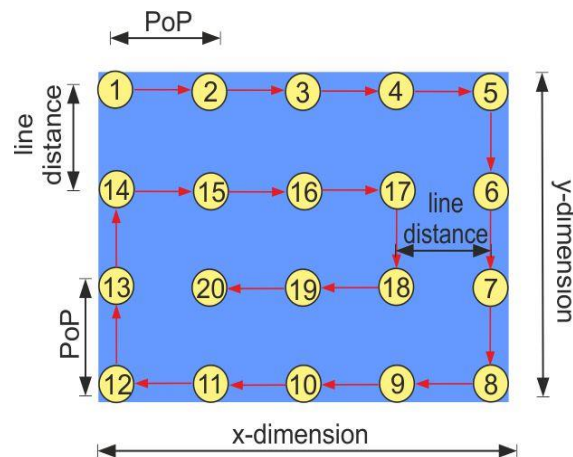
Figure 23: spiral-inward (SI)

Again, the spiral-inward strategy can be performed in full beam modus or in chopped modus. The spiral direction moves clockwise towards the center. To get the later used mirrored pattern (anti-clockwise) the original spiral-inward stream file was manipulated with Excel (multiply the X coordinate with -1 and shifting for the maximum X-pixel value).

In an advanced version, one can select the distance between two parallel patterning lines individually (strategy name: "spiral-inward with variable line distance"). This strategy is also available as full beam and chopped beam version.

3.4.1.5   *Spiral-outward (SO)*

Figure 24 shows the patterning sequence of the spiral-outward strategy (**SO**).
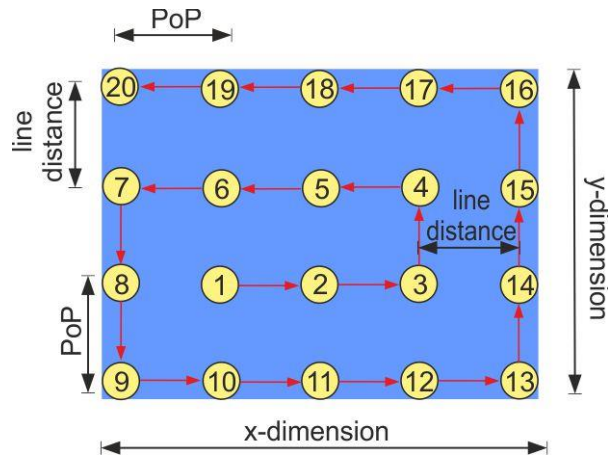
Figure 24: spiral-outward (SO)

For the spiral-outward strategy, the same chain of patterning points as for spiral-inward are used, but in contrast, the starting and endpoint are exchanged. Therefore, the patterning direction is anti-clockwise.

Analogous to the spiral-inward four versions are possible:

1) Full beam
2) Chopped beam
3) Full beam with variable line distance
4) Chopped beam with variable line distance

3.4.1.6   *Strategies for freestanding 3D structures*

By adequate selection of patterning parameter (beam current, voltage, point pitch, total exposure time) it is possible, to fabricate freestanding nanostructures (4.3). In the stream file generator the following strategies are implemented:

a) Single Pillar

By selecting the option "single pillar" one single pixel (X = 0, Y = 3000) is exposed for a certain total exposure time (user input). The selected TET is automatically partitioned into packages of 10 ms. This very primitive strategy however is very useful, because the maximum dwell time per command line in a stream file is limited to 25 ms.

An alternative approach for a greater number of pillars is the self-written console application "Einzelpunkte". Here the user has the possibility to decide the coordinates and TET for several pillars individually. In contrast to the "Single pillar"-strategy one has to count the number of command lines

in the generated stream file (with e.g. Origin or Excel) and then to change the third line in the file (replacement character = "1234") to the correct value.
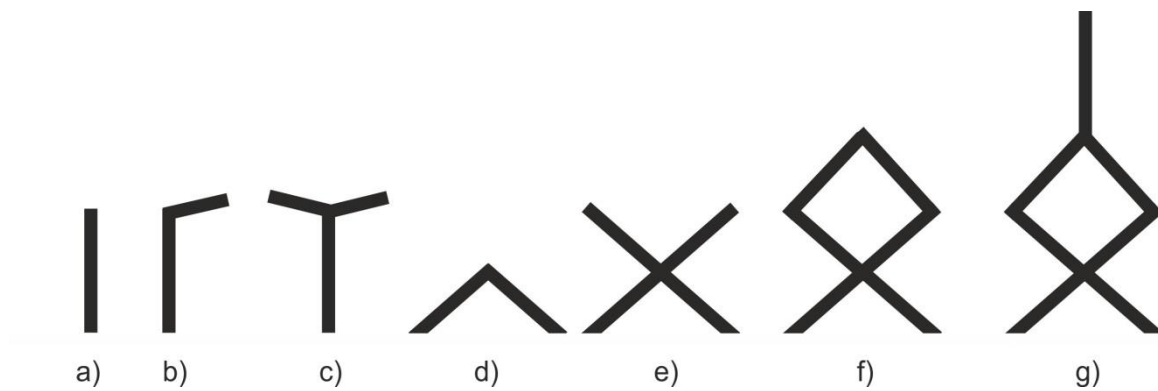

Figure 25: freestanding structures (side view): a) single pillar; b) diving board; c) T; d) bridge; e) double-bridge; f) triple-bridge; g) triple-bridge with antenna

b) Diving board

The option "diving board" creates a single pillar as described before and adds a line afterwards (Figure 25b). For FEBID-application the slope of the line strongly depends on the process parameter. This strategy is very beneficial for parameter testing (4.3.2.3).

c) T

Similar to the diving board this strategy creates a line on the top of the pillar, but with the difference, that the top bar is supported by the pillar at its middle point.

Here, a slightly different patterning approach is used: The beam jumps alternating from one point to the opposite T-branch. This procedure is preferable, otherwise the second branch might not start on the top of the pillar due to drift problems.

An additional plus of this alternating point approach is the doubled refresh time for each point.

In reality, real freestanding horizontal bars are very hard to achieve, so in most cases the "T" looks more like a "Y" (Figure 25c)..

d) Bridge

In top view, this strategy simply creates a horizontal line. The patterning sequence is again alternating: After finishing point 1 at the left end the electron beam jumps to the right end, afterwards back to the left. Continuing this procedure, the middle points have to meet at the same point, even when strong drift appears.

If the process parameter (dwell time, point pitch, current, voltage) are adequate, the resulting structure gets a freestanding Λ (Figure 25d).

With the option "number of bridges" it is possible to add further branches/bridges (Figure 25e,f).

e) Bridge with antenna

This strategy adds a pillar in the middle of the bridge/multiple bridges (Figure 25g).

f) Circle

In top view, this strategy simply creates a circle or a circular arc. The patterning sequence is not alternating. If the process parameter (dwell time, point pitch, current, voltage) are adequate, the resulting structure is a freestanding spring.

g) Circle on pillars

This strategy fabricates a stream file with two pillars which are connected by a circular arc on top. In contrast to the ordinary circle, the point sequence is alternating to overcome problems with drift and enhance the replenishment.

4   Experiments and Results

The aim of this this thesis was to gain improved fundamental understanding of the FEBID process with respect to gas dynamics and the correlation with the shape performance. Therefore, 3D-deposits were fabricated in the dual beam microscope (**DBM**) subsequently investigated via atomic force microscopy (**AFM**). The obtained morphologies show manifold characteristic in dependency on beam process parameters, patterning strategies and gas injection system (**GIS**) arrangements.

The first issue investigated in this thesis, concerns the influence of the molecular gas flux. Chapter 4.1 reveals the GIS alignment as crucial element with respect to the deposit shape performance. The experimental setup allows decoupling of gas flux adsorption and surface diffusion during molecular replenishment. Furthermore, geometrical shadowing effects (4.1.3.3) could be assigned to be responsible for many morphological problems on the nanoscale.
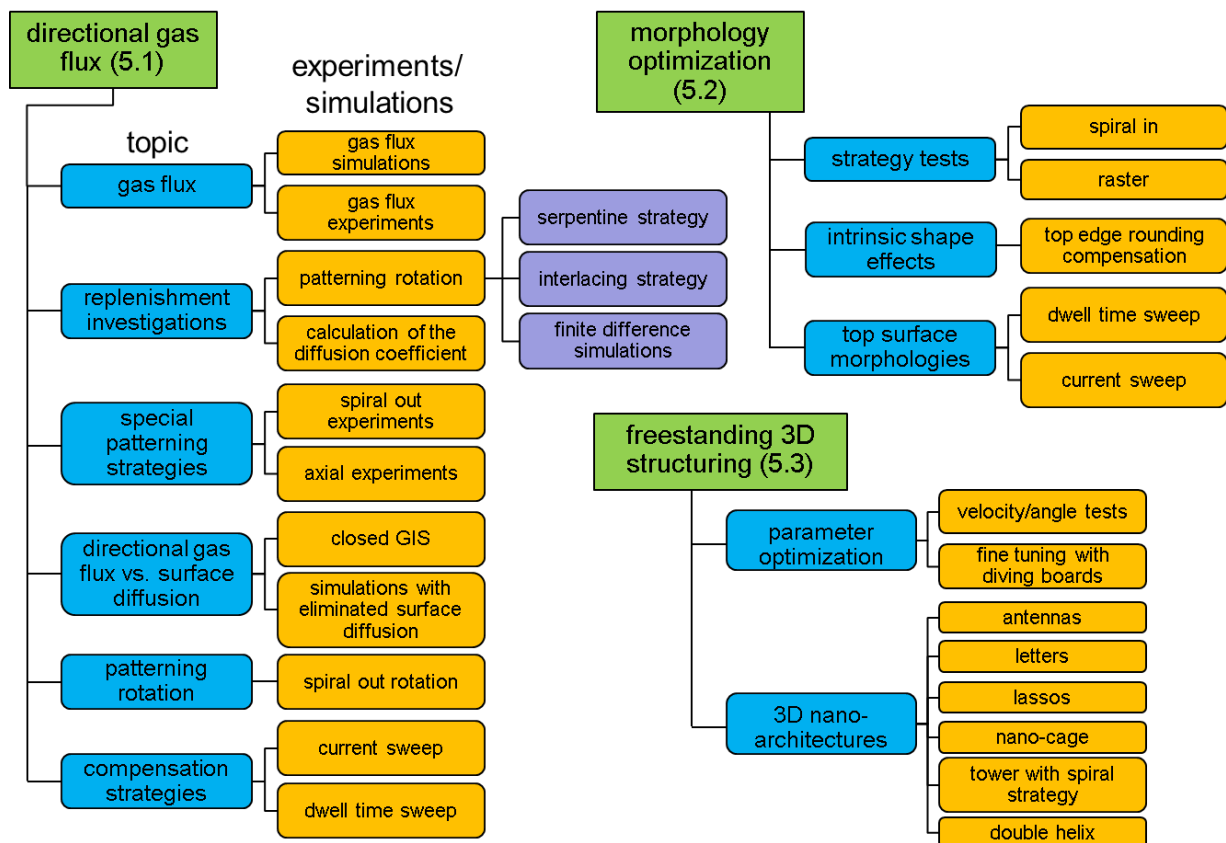
Figure 26: overview of the conducted experiments, simulations and calculations. The green boxes represent the three main aspects of this master thesis further split into subtopics given in blue. The golden and purple fields show detailed experimental variations, simulations and calculations. Please note, some experiments are used for the interpretation in many different chapters, but only listed at their first appearance in the text.

Based on these fundamental investigations, we focused on the optimization of deposit shapes (4.2). As a first step, intrinsically unavoidable effects like the lateral base broadening (4.2.2.1) and top edge

rounding (4.2.2.1) have been identified. For the latter, a compensation procedure was successfully introduced (4.2.2.3) revealing improved shape performance by means of edge sharpness. Together with the systematic parameter variation results in chapter 4.1, we could derive ideal process parameter ranges for high-fidelity deposits on the nanoscale.

Due to the deep insight in molecular dynamics and its variation during growth we could finally implement real 3D nanofabrication with complex shapes (4.3) which are of great interest for novel sensing concepts.[46]

For orientation, Figure 26 gives an overview of the different experiments and simulations conducted in each chapter.

4.1 Directional gas flux

The main idea of this section is to answer the question, whether the GIS alignment affects the resulting deposit shapes. To investigate that, we start with a gas flux simulation to get an idea of the coverage distribution by the gas nozzle (4.1.1). After that, the theoretically predictions are verified by real experiments (4.1.2). The findings enable us to define a gas flux vector and its X/Y components (4.1.2.2), which will be very helpful for further discussion.

Experiments using different scan directions (4.1.3.1) and considerations concerning the fundamental replenishment mechanisms leading to the finding of a geometrical shadowing effect (4.1.3.3). This theory is supported by simulations (4.1.3.4) and confirmed by all consecutive experiments.

By introducing special patterning strategies (spiral-out and interlacing in 4.1.3.5 and 4.1.4, respectively) a deeper insight of the deposition process and the need of a careful nozzle alignment is presented.

Experiments with a closed GIS eliminate the directional gas flux and elucidate the contribution of surface diffusion to the morphology (4.1.5). Vice versa, the diffusive component is turned off in simulations showing the impact of the directional gas flux to the shape (4.1.6).

As geometrical shadowing effects lead to disrupted and, more importantly, uncontrollable morphologies, two compensation strategies are applied which are discussed in chapter 4.1.8. By varying the beam current and pixel dwell times, the precursor working regime can be controlled which further confirms the existence of directional gas flux effects and its strong influence on final deposit shapes.

4.1.1 Gas flux simulation

As described in 3.1.2, one main component in the FEBID-process is the local balance between precursor molecules and potentially dissociating electron species. Therefore, we have to take a detailed look at the supply for our experimental setup which ultimately determines the replenishment situation. In order to investigate the laterally resolved precursor adsorption from the GIS, a simulation for the given geometry was performed. Friedli et al.[38,47,48] showed, that the

coverage is site specific and depends on several parameters like nozzle diameter or distance and angle to the surface. The experimental setup of our gas injection system (**GIS**) is summarized in Figure 27.
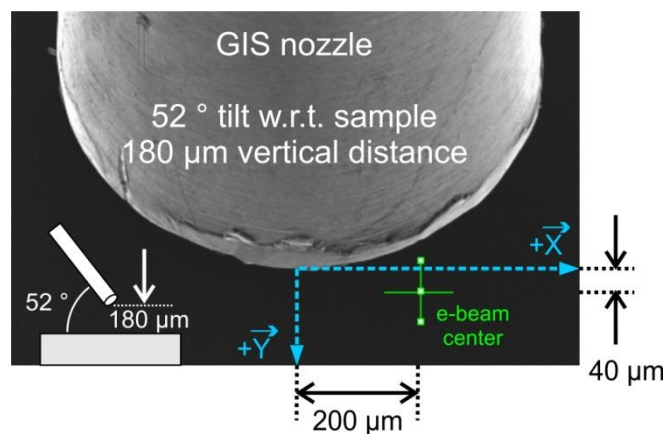
Figure 27: SEM picture of the GIS nozzle in top view. The green cross marks the position of deposition. For further discussion the direction along to the nozzle main axis is denoted as Y-axis with the X-direction in perpendicular arrangement. The bottom left inset schematically indicates the GIS alignment in a side view.[49]

The distance of the lower GIS edge to the surface was determined to 180±10 µm. The nozzle includes an angle of 52° with respect to the sample surface and has an outer diameter and an inner diameter of 830 µm and 500 µm, respectively. With a beam scan rotation of 41° the GIS nozzle was adjusted in such way, that the patterning Y direction coincides with the projection of the GIS main axis. The deposition area is on purpose shifted by 200 µm in X-direction and 40 µm in Y-direction with respect to the central GIS front (green cross in Figure 27). This off-axis geometry has been chosen to clearly demonstrate the influence of the gas flux direction on finally achievable deposit shapes as a main finding of this thesis.

Using this individual geometrical GIS arrangement as input parameter for the gas flux simulation by Friedli and Utke[47] the laterally resolved relative flux ratio J/J_{TOT} can be calculated. As shown in Figure 28, the impinging molecular flux is not radially symmetric. This entails two effects for the given deposition area indicated by the green cross: *1)* the radial adsorption rate shows a gradient of about 0,03 % per µm leading to *2)* isotropic diffusion gradients at the deposition area (gradient in X-direction: 0,009%, gradient in Y-direction: 0,028%. Therefore, a different strength of the X-component of the impinging molecular flux in comparison to the Y-component is expected. To calculate their ratio will be an important result of the following experiments (4.1.2.2).

4.1.2   Gas flux experiments

The last section has shown site specific coverage with precursor molecules via simulations, using the given GIS alignment. Before we can proceed, we have to compare the simulation results to real

conditions. For different reasons discussed below, free standing nano-pillars have been used for experimental comparison which are found in very good agreement with the simulations.

As a result, we introduce a gas flux vector (**GFV**) to describe the preferred direction of the molecular gas flux with respect to the deposits. Due to an on-purpose off-axis deposition site we will show, that it is reasonable to evaluate X and Y- components separately for a proper description of all observed effects discussed later.
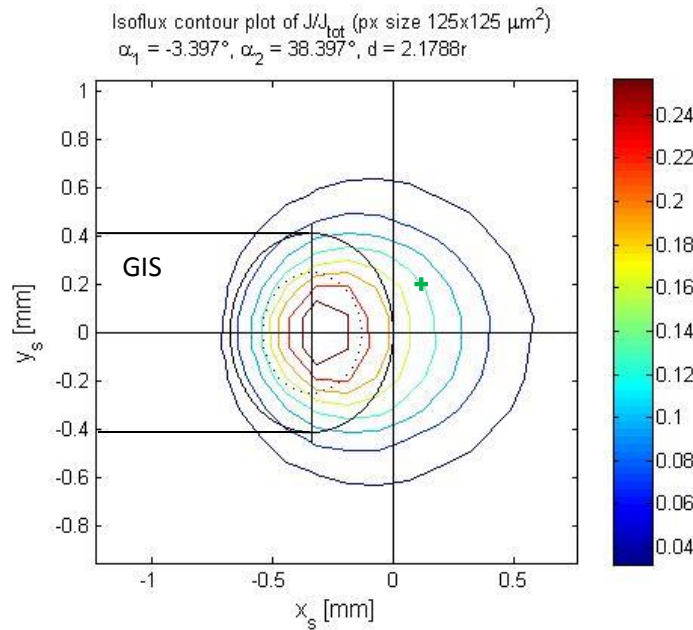

Figure 28: result of the gas flux simulation[47] for the given geometry, shown in Figure 27. As indicated, the GIS nozzle comes from the left side, the black ellipse indicates the projection of the nozzle on the surface, the green cross marks the deposition site.

4.1.2.1   Verification of Gas flux simulation results with experiments

Since the simulation describes only gas flux adsorption and ignores replenishment via surface diffusion, quasi 1-D nano-pillars can be used to mimic gas flux simulations: as shown by Plank et al.,[40] the volume growth rate changes dramatically during height increase, leading to a relative constant value after a certain growth time (Figure 29). Two effects explain the varying volume growth rate (**VGR**): *1)* the change of the interaction volume; and *2)* 2D-surface diffusion to the point of deposition. The former is related to the higher atomic number of the deposited material compared to the used Si substrate. The interaction volume gets gradually confined during early growth stages, leading to an increasing number of dissociating electrons per unit area on the surface. This explains the initial VGR increase in Figure 29 in agreement with previous studies.[40] Once the entire interaction volume has travelled from the substrate into the deposit, the number of dissociating electrons stays widely constant for the rest of the growth time. The second influence is related to the change of diffusion path towards deposition areas. While the precursor supply from the substrate to the pillar tip is only efficient for short pillars (2D-diffusion) the narrow pathway for increasing pillar heights (2D

→ 1D-diffusion) reduces the replenishment mechanism to gas flux adsorption from the gas phase as assumed during the gas flux adsorption.[5] This behaviour is reflected in the decreasing VGR trend in Figure 29 towards a widely constant non-zero VGR.
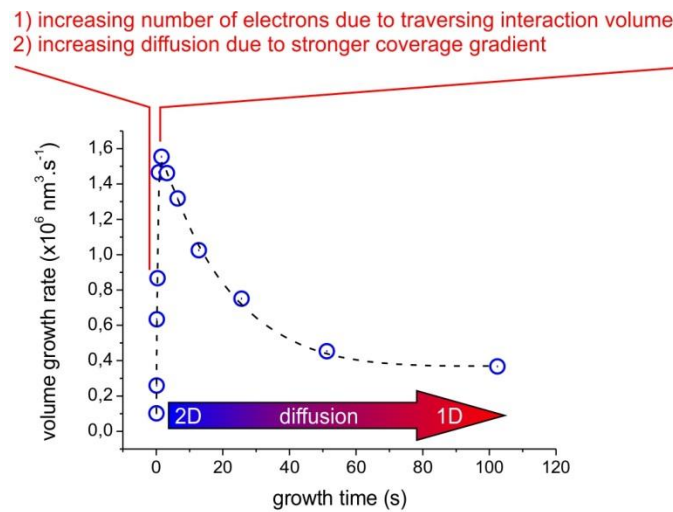

Figure 29: volume growth rate vs. growth time of a Pt-C nanopillar deposited at X = 200 μm and Y = 40 μm (5 keV, 98 pA).[49]

Considering this VGR behaviour, the experiments use only sufficiently tall pillars to ensure, that the observed height variations mainly originate from the varying gas flux adsorption and not from surface diffusion effects. In detail, 49 pillars (5 keV, 98 pA) were distributed equidistantly in an array of 120 x 120 μm according to the blue frame in Figure 30. Subsequently, their heights were measured and normalized to the highest pillar which is summarized in Figure 30b. Similar to the simulations, the pillar heights show a strong decrease in Y-direction while there is only a weak variation in X-direction. Please note, the grey square indicates the size of a typical deposition array (20 x 20 μm) in order to put the investigated area in relation to deposition areas practically used. A detailed comparison between experiments and simulations is shown in Figure 30b at the bottom. The height tendencies along the dotted black diagonal in Figure 30b show a good agreement with the matching line from the simulation (Figure 30a).

In addition, we tried to verify the gas flux simulation with 3D pads along X-direction (Y = 40 μm) starting from X = 100 μm to 300 μm as indicated by the red arrow in Figure 30a. Beam currents and dwell times were kept very low (25 pA, 1 μs) to minimize diffusion related influences driven by local depletion gradients. Again, the experimental data fits very well to the simulation as shown by a direct comparison in Figure 30c.

Due to the verification experiments above it can be stated, that the gas flux simulator can be used to predict *1)* the site dependent relative molecule flux J_X/J_{TOT} (pillar experiments); and *2)* the local coverage with precursor molecules (3D pads experiments). Furthermore, the latter result shows that for the areas of interest, the surface coverage is clearly below one monolayer (= 100 %) as expected (typically around 30 %).[17,20,50,51]

Please note, the concentration gradient originating from the gas flux distribution is very low (<1% in within a typical deposition area) and surface diffusion (without any irradiation) can be neglected in first approximation. For experimental validation, the heights of nine identical 2 x 2 μm pads were fabricated in a 3 x 3-matrix-arrangement with 5 μm spacing between the footprint borders. AFM height measurements reveal no tendencies concerning fabrication sequence or relative positioning within the typical deposition area.
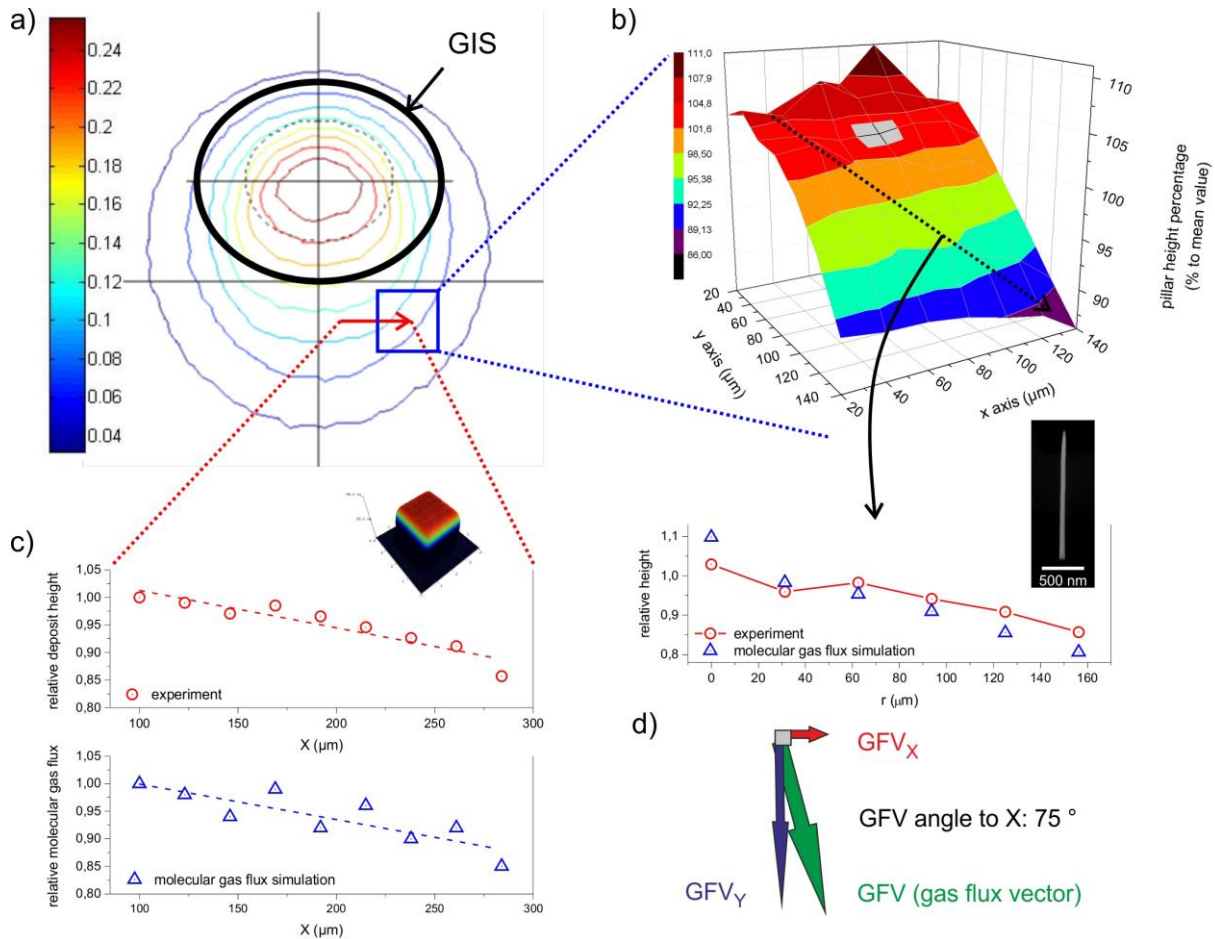
Figure 30: verification of the gas flux simulation (a) via nano-pillars (b) and 3D pad growth (c) which enables the definition of the gas flux vector GFV (green arrow) (d) to be approximately 75° with respect to the X-axis.[49]

4.1.2.2 Gas flux vector

For further discussion it is comfortable to introduce the gas flux vector (**GFV**) to describe direction and magnitude of the gas flux. It is defined as the tangent normal on the lines of equal flux ratios J_X/J_{TOT} (Figure 30a). With respect to the used deposition area (see Figure 28), the GFV includes an angle of 72° with respect to the X-axis based on the gas flux simulations.

For the following considerations, it is convenient to split the main gas flux vector GFV into its X and Y components **GFV$_X$** and **GFV$_Y$** as shown in Figure 30d. Evaluating the gradients in X – and Y- directions

derived from the pillar experiments above, a ratio of 1 : 3.8 is found which is equivalent to a GFV angle of 75°. This is in excellent agreement with the GFS results and rotation experiments discussed in detail later (see chapter 4.1.7).

4.1.3 Directional gas flux replenishment

As shown in the previous chapters, the molecular gas flux adsorption is laterally inhomogeneous and can be described via the GFV. In the following, the importance of the patterning direction with respect to the GFV is shown via experiments including rotated serpentine strategies (4.1.3.1). To interpret these results, we have to take a closer look at possible replenishment mechanisms (4.1.3.2) which emphasis on surface diffusion. As will be shown, the deposit generates a morphological barrier leading to geometrical shadowing effects for impinging precursor molecules (4.1.3.3) even for deposits heights below 100 nm. Dynamic growth simulations[49] by an external collaborator (Oak Ridge National Labs, USA) are then presented (4.1.3.4) which show excellent agreement with experiments giving further evidence of the directional gas flux component and its role during FEBID processing. The findings indicate the crucial importance of a careful patterning alignment with respect to the GIS arrangement to obtain high-fidelity deposit shapes.
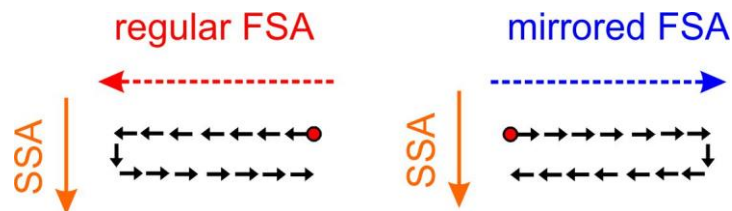

Figure 31: definition of regular (left) and mirrored (right) Fast Scan Axis (FDA) including the orientation of the Slow Scan Axis (SSA).

4.1.3.1 *Influence of scan direction*

Unless otherwise stated, 3D pads with a footprint of 2 x 2 μm were used, fabricated with a point pitch of 13 nm, a total exposure time of 1000 μs and an acceleration voltage of 5 keV. Further parameter for the first set of experiments were the serpentine scan strategy (**SP**, 3.4.1.2), a beam current of 1600 pA and a dwell time 1000 μs. The latter value is high enough to deplete the patterning point and its proximity in a radius of about 60 nm known from previous studies.[52]

For a simplified discussion throughout this thesis, we introduce the fast scan axis (**FSA**) as direction of consecutive scanning points and denote the direction perpendicular to the FSA as slow scan axis (**SSA**) as schematically shown in Figure 31.

With this set of parameter specified above, four 3D pads with different FSA directions relative to the main gas flux vector GFV were fabricated (see Figure 32) and subsequently characterized with atomic force microscopy (AFM). All deposits revealed widely flat surfaces as representatively shown in Figure 32c by an AFM height image. However, calculation of the according VGRs revealed strong

variation as shown by the red bars in Figure 32d. To interpret this behaviour we have to consider the scan-directions as well as the X / Y components of the GFV:
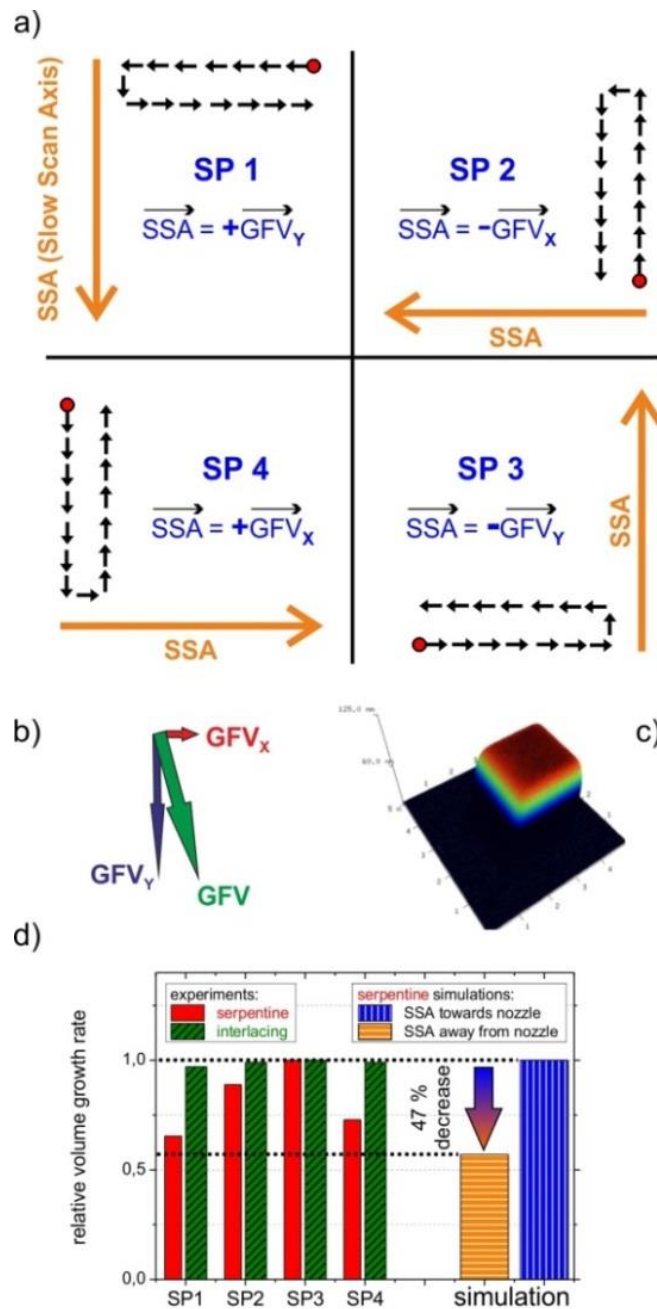
Figure 32: a) definition of the slow scan axis (SSA) and the four different patterning approaches (SP 1 - SP 4); b) Correct relative orientation of the GFV; c) 3D-AFM image of a deposit with serpentine strategy; d) shows the volume growth rate deviation from the maximum value for serpentine strategy and for interlacing strategy (see main text). Simulations of relative VGRs for SP 1 and SP 3 configuration reveals good agreement with experimental values.[49]

When the SSA heads towards the (strong) GFV$_y$ direction highest VGR is achieved, followed by the pads fabricated with SSA towards the weaker GFV$_x$ direction. When the SSA has the same direction as the GFV$_x$, the VGR gets even lower. The smallest value for growth arises while the SSA-patterning along the GFV$_y$ (Figure 32). To eliminate an influence of the direction of consecutive points within one scanning line (FSA) the same experiments with a reversed point sequence was performed (mirrored FSE, Figure 31). The results show the same tendencies, so the FSA does not affect the observed effect and we can reduce our discussion to the relation between the SSA and the GFV. However, before we can proceed to the interpretation, we have to take a look at the replenishment processes.

4.1.3.2 *Replenishment mechanism*

The long dwell times (**DT**) used in the previous experiments deplete the local coverage with precursor molecules in the proximity of a patterning point. On the one hand, this concentration gradient enhances the surface diffusion towards the deposition point. On the other hand, the directional gas flux from the GIS provides new precursor molecules.

Surface diffusion:

To describe diffusion, the specification of the *diffusion constant D_0* (*surface diffusion coefficient, 3.1.3*) is essential. This determination was done particular for our experimental setup via pulsed single dots experiments.[49] By varying the pulse duration, the resulting shapes are changing (Gaussian → Indent → Flat top) what indicates a change of the working regime.[22]
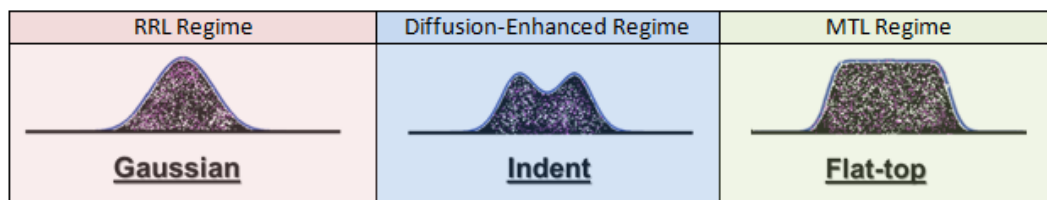
Figure 33: three different deposit shapes during single dot experiments are assignable to different working regimes.[49]

By using a defocused beam and different TETs, the transition from one shape to an other can be observed. These points of transition are necessary for calculating the diffusion constant via the continuum model.[17]

For our system, the diffusion constant was calculated to a value between 8.5×10^{-10} - 6.5×10^{-9} cm²/s and a typical *residence time τ* of $60 - 100$ µs before the precursor molecule desorbs again. According to, $\langle r \rangle = \sqrt{4 \cdot D_0 \cdot \tau}$ the *radial diffusion length $\langle r \rangle$* can be estimated between 2 and 25 nm, assuming 2D random surface diffusion.[22,49] Please note, the mentioned calculations have been done in collaboration with the EMPA (Thun, Switzerland).

The main point of the upper calculations is the fact, that most of the precursor molecules are not able to move for large distances. After maximum 25 nm (which is equal to a residence time of 100 µs) they desorb again. The replenishment of a depleted patterning point via surface diffusion is therefore only possible in a very limited action radius. We have to keep that in mind when talking about diffusive replenishment mechanism in the following chapter.

4.1.3.3   Geometrical shadowing

As discussed in chapter 4.1.1 and summarized in Figure 30 the simulations are valid for flat surfaces. By building up a morphological barrier during growth, it is therefore likely that the coverage will locally differ due to hindered electron paths. This effect, depending on the GIS alignment (tilt angle, lateral position of the deposition area) has basically been described before by Friedli et al.[38,48] The implication by a 3D deposit is geometrically explained in Figure 34: assuming straight molecule trajectories there is a shadowed region at the backside of the deposit. Evaluating the shadowed distance for our individual geometry reveals a minimum shadow radius Δr_S of 20% with respect to the deposit height. Figure 34b explains the possible replenishment mechanism for the shadowed areas:

1) **Surface related**: Diffusion of precursor molecules from surrounding substrate surface (surface related replenishment – diffusion, **SRR - D**). Considering the radial diffusion length $\langle r \rangle$ calculated in the previous section (2 - 25 nm), it is obvious, that despite the increased concentration gradient (who is the driving force for diffusion), many molecules desorb again on their way to the shadowed region. Especially, when the deposit gets higher (about 150 nm for the serpentine experiments), even the calculated minimal shadow radius Δr_S (30 nm) is larger than the maximal diffusive length. Please note, the 20% criterion for the shadow radius assumes the most beneficial angle while a majority of the trajectories show higher radii (red line in Figure 34a).

2) **Re-adsorbtion**: Desorbed precursors re-adsorb in the shadowed area indicated by the yellow arrow in Figure 34b (**SRR – RA**).

3) **Deposit related**: Physisorbed molecules on the surface of the deposit diffuse "downwards" to the shadowed area (deposit related replenishment **DRR**).

However, replenishment is crucial when SSA patterning away from the GFV$_Y$ is performed. In this case, the electron beam always exposes points in the shadowed region. Due to fewer available precursor molecules, the volume growth rate suffers and final deposit gets lower. This explains the experimentally found lower VGR value for the SP1-configuration (compare to Figure 32). In contrast, when SSA patterning towards the GFVY is performed (SP3 in Figure 32a, d) the beam works on the front side of the deposit and no shadowing effect affects the patterning process. Therefore, an enhanced VGR is expected and indeed validated experimentally. To explain the different VGRs for SP2 and SP4 configurations one has to keep in mind, that the GFV has also a component in X-direction. For the serpentine in SP4 setup (away from GFV$_x$) the shadowing effect appears even if the effect is smaller due to the weaker X-component.

By eliminating the X-component (rotating SSA parallel/perpendicular to main GFV or shifting deposition area to the main axis), these two configurations get the same VGR (see later experiments: 4.1.4.1 and 4.1.7).

We shortly want to summarize these very important findings, which explain many of the consecutive experiments. Behind a morphological barrier a shadowed region of minimum 20 % of deposition height appears due to the GIS arrangement. This area cannot be sufficiently replenished via surface diffusion due to the short diffusion length of about 25 nm. **The only supply with precursor molecules is related to downwards-diffusion from top areas and, to minor extent, backside re-adsorption.**
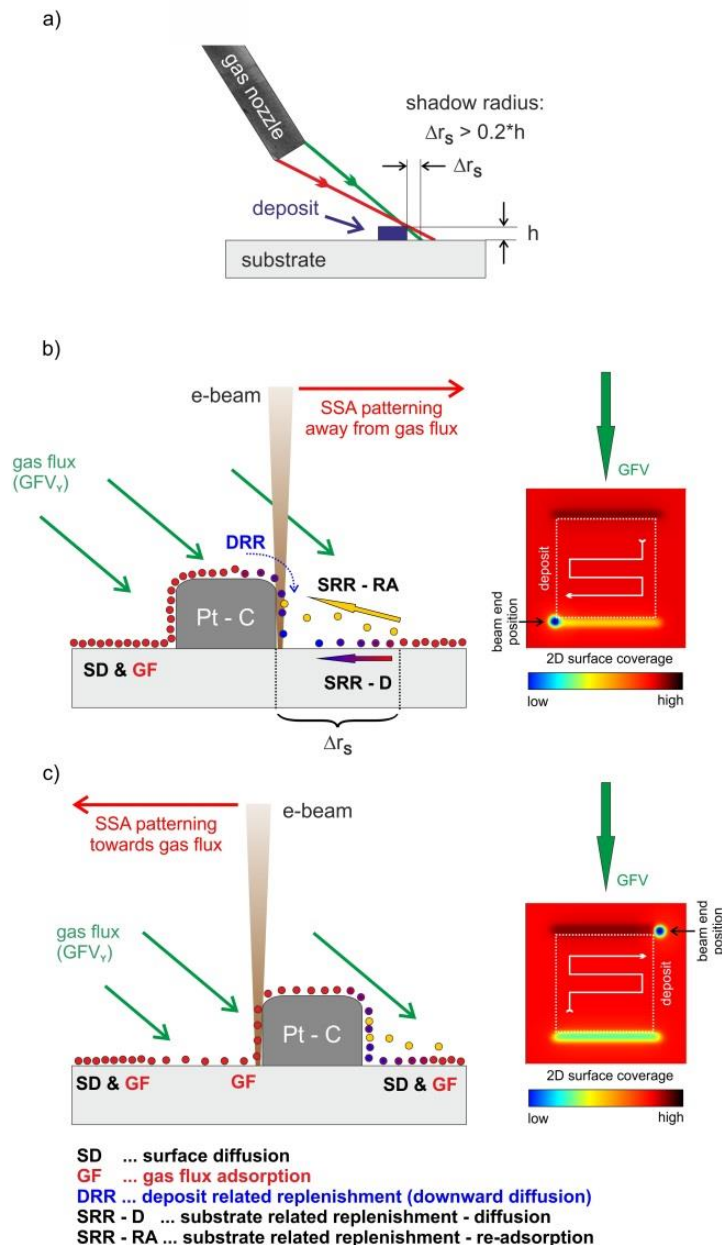

Figure 34: a) schematic explanation of the geometrical shadowing effect. b) SSA patterning away (in the shadowed area) and towards the GFV: replenishment mechanism and simulation of surface coverage are shown in b) and c) respectively. The simulation reveals a relative low coverage with precursor molecules at the backside and a high coverage in front of the deposit.[49]

4.1.3.4 Finite difference simulation

The previous explanatory models base on the evaluation of the final deposit. To reinforce this thesis, Jason Fowlkes supported the experiments with finite difference simulations.[21,49] For the simulation, the experimental settings (geometrical, process parameter) were imitated to provide comparability to the results. The calculation implements among other things the contribution of SE_1 and SE_2, the precursor dynamic (desorption, diffusion, based on the calculated diffusion coefficient $D_0 = 8.5 \times 10^{-10}$ cm²/s) and the impinging gas and electron flux. With this, mimicry of the dynamic growth and local precursor coverage can be visualized. The results are shown on the right sides in Figure 34b and c, revealing enhanced precursor coverage at the front side of the deposit (black areas) and the lack of precursor molecules at the shadowed backside (yellow areas) as suggested by the theory discussed above.

Comparing the simulated final height for SSA patterning towards and away the GFV respectively reveals a difference of 47 %, which is in good agreement with the experimental results for SP1 / SP3 configuration as can be seen by direct comparisons in Figure 32d.[49]

4.1.3.5 Rotation of interlaced patterns

As consequence of the previous section, the user has to take care of the correct alignment of his pattern in relation to the gas flux. In generally the SSA patterning towards the main GFV is preferable, because it provides the highest VGR.

When using the interlacing strategy, it is possible to overcome this careful alignment. The patterning sequence of an interlacing strategy was discussed in 3.4.1.3, an interlacing distance of 130 nm and a final point pitch of 13 nm was used. The main difference is the reduced degree of precursor depletion as the interlacing strategy uses large point pitches which reduces local consumption. Therefore, each single point has much longer time to replenish the area of new deposition even on the backside of the deposit via surface diffusion. Hence, the effect of geometrical shadowing is much less striking which should then lead to *1)* much more constant volume growth rates which are expected to be *2)* independent on the FSA orientation. Experiments, executed with same beam current, final point pitches and dwell times confirm this assumption as can be seen by the green bars in Figure 32d. Especially, when the deposition footprint is more complex than the simple square, the interlacing strategy is a very clever method to fabricate stable morphologies in a straightforward manner which minimizes unwanted effects from stemming from the directional gas flux components. However, it is needed to mention that the interlacing strategy is limited by the lens strengths of the DBM used. The exploitation of the limits is subject of ongoing research at the FELMI.

4.1.3.6 Consequences of the shadowing effect

As implications of the shadowing effect, first the geometrical setting of the GIS system has to be taken into account. Namely the nozzle tilt angle as well as the deposition area relative to the GIS need to be considered. The former should be steeper to reduce the shadowing radius Δr_s.

As the shadowing radius depends on the height difference between the morphological barrier and the surface behind it, the influence of the shadowing effect can be reduced by exactly lowering this level difference. There are two possibilities to achieve that: *1)* lowering the beam current, and *2)* lowering the dwell time. Both changes reduce the local growth at each patterning point and by that reduce the shadowing radius. For a detailed discussion, we refer to 4.1.8. Please note, another workaround to this shadowing problem is the usage of a bevelled nozzle (see Figure 15).

Additionally to the morphological effects, the shadowing effect might influence the chemistry. Due to the different coverage with precursor molecules when patterning in front of the deposit and within the shadowed area respectively, the working regimes are shifting. As discussed in 3.3.2, this results in different degrees of dissociation of the precursor complex and more or less carbon is implanted.

4.1.4   Special patterning strategies

To show the gas flux related effects stemming from the different scanning directions with respect to the GFV (see SP1-SP4 from the previous experiments) within one pad, we introduced the spiral-out (**SO**) patterning strategy (3.4.1.5). Please note, all process parameter were kept identical to the previous section, just the sequence of consecutive patterning points has changed from serpentine to spiral-out. Nevertheless, the resulting deposit shows a completely different morphology (Figure 35) than the flat surface via serpentine strategy in Figure 32c and is far away from the desired shape. Despite that, this strategy is perfectly suitable to investigate contributing effects.
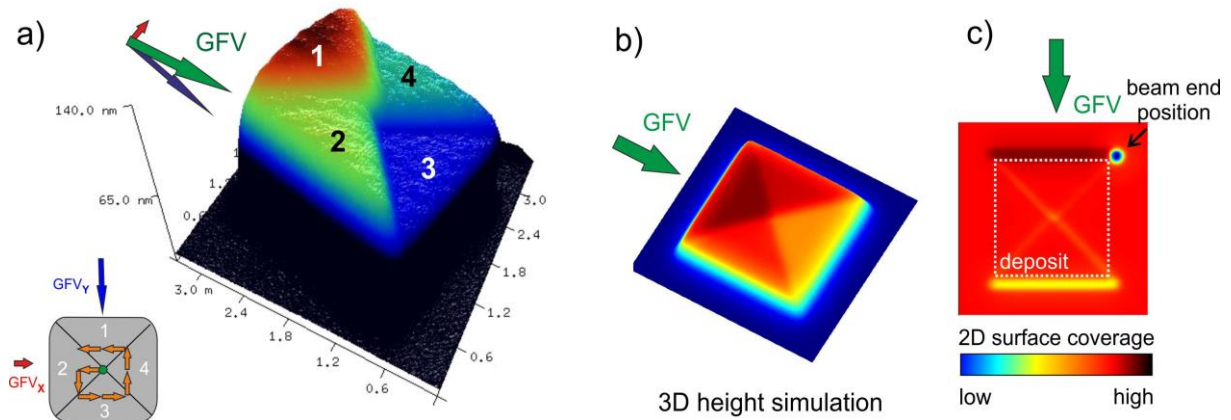

Figure 35: 3D-AFM image of a spiral-out pad (a) shows a terraced morphology with four different segment heights. The orientation of the GFV and its X/Y - components as well as the patterning sequence are indicated; b) simulated deposit heights showing similar terraced behaviour. Please note for reasons of simplification the x-component of the GFV from the experiments was neglected, leading to three different segment heights. c) coverage with precursor molecules after finishing the SO pattern.[49]

The four triangular terraces (nomenclature see Figure 35a) have different heights which again can be explained by the shadowing effect. Figure 35c schematically shows the different precursor coverage for SO patterning. As can be seen in Figure 36, the GFV$_Y$ directly replenish the growing front of sector

1, therefore this segment is the highest. In contrast, in the third sector the GFV_Y is shadowed by the deposition in sector 1, consequently the growth rate suffers. For the understanding of the different heights of quadrant 2 in comparison with quadrant 4, one have to consider the (weaker) gas flux component in X-direction. In analogy to the previous argumentation, the sector 4 is lower than sector 2 due to the shadowing action of the latter to the GFV_X.

Due to the introduced spiral-out strategy we can investigate all four rotational situations (SP 1 – SP 4, Figure 32) with one pad which eliminates eventual variations between two separate deposits. The different height tendencies due to the shadowing effect can therefore examined very clearly in one single fabrication step. The following experiments for example are only possible by using the spiral-out patterning strategy.
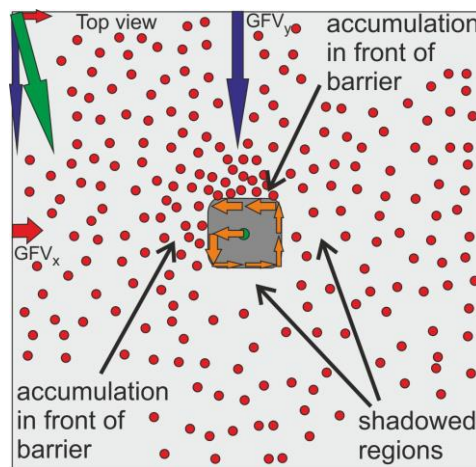

Figure 36: shadowing effects during spiral-out scan. The precursor densities at the GFV facing fronts (top and left edge) are higher than at the backside of the deposit. The red circles schematically indicates precursor molecules.

4.1.4.1 Axial experiments - Shifting deposition area

The experimental morphology of a SO-pad (Figure 35a) slightly differs from the simulation (Figure 35b) in the height of sector 2 and 4. Whereas the simulation[49] suggests an equal height level for sector 2 and 4 these two segments differs in height. The reason is the missing GFV_X component in the simulation. If it is possible to eliminate the GFV_X component in the experiments as well, we should end up with the same qualitative result. In practice, the size (and sign) of the GFV_X depends on the position of the deposition area in relation to the main axis of the nozzle (see Figure 27 and Figure 30a). Therefore, if we put the deposition site directly on the main axis, the GFV_X component should disappear for this symmetrical alignment.

We started from the standard deposition site (200 μm away from the main axis, Figure 37 pad in the middle) and located each following deposition position 25 μm closer to the main axis (200→175→150→125→100 μm away from the main axis). Due to technical limitation, it was not possible to go to the desired 0 μm ("on-axis") alignment. Nevertheless, the effect of a vanishing GFV_X

component already gets visible: As supposed, the left and the right sector get equal in height (Figure 37 top left).

In contrast, by moving further away from the standard deposition site (200→225→250→275→300 µm) the level difference between sector 2 and 4 increases (Figure 37 top right). Figure 37 bottom row demonstrate the gradually evolution of sector 2 and 4 while changing the X-coordinate of the deposition position.

Please note, similar shifting experiments were already shown in Figure 30c (top) for SP pads to validate the precursor coverage. Again, the advantage of the SO strategy gets obvious, showing not only the varying GFV_X component, but also reproducing the coverage results by measuring the height of sector 1.

Concluding the upper results, we could show, that the shadowing effect in Y-direction is still present, but can be eliminated in X-direction by selecting the deposition site on the main axis.
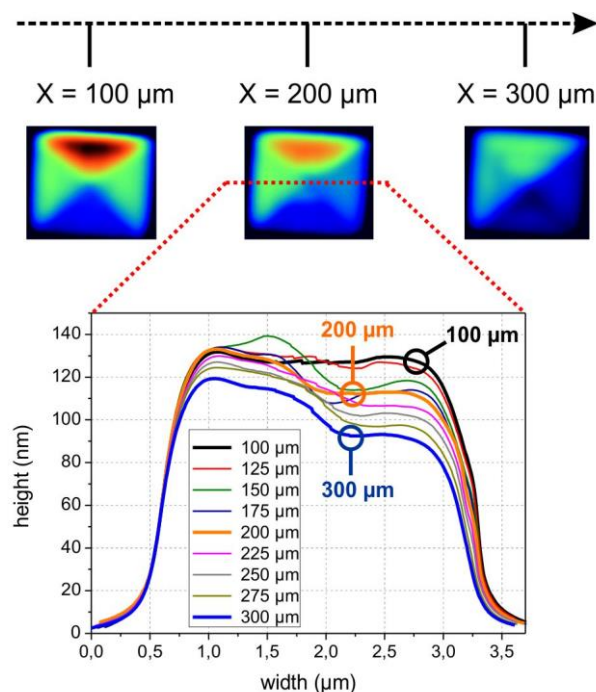
Figure 37: change of deposition site along the x-axis. The AFM-height measurements of the 9 SO-pads with 1000 µs DT, 5 keV and 1600 pA are shown at the bottom, the extreme values (100 µm, 300 µm) and the standard position (X = 200 µm) are marked and shown on the top. The pointed red line indicates the direction of the height measurement across sector 2 and 4. The differences in the left and right quadrant correspond to varying GFV_X value. The top edges are aligned perpendicular to the GFV_Y.[49]

4.1.5 Eliminating the directional gas flux adsorption

The former considerations identify the directional gas flux as the responsible component for the disrupted morphology for SO pads. In order to further test the hypothesis and to investigate additional effects which are screened by the predominant shadowing effect two main experiments have been performed: *1)* turning off the gas flux, and *2)* pattern rotation. The former will be discussed in this section while the latter will be the topic of chapter 4.1.7.

As a starting point the surface was brought into stable coverage equilibrium by sufficient gas flux exposure without e-beam irradiation (> 3 minutes before patterning). In the next step, the GIS-valve was closed, the GIS nozzle retracted and the patterning process started within less than 3 seconds. This procedure ensures, that no directional gas flux component from the nozzle acts on the deposition process and therefore no shadowing effect influences the structure growth. Please note, after closing the GIS valve there are a still a certain number of precursor molecules in the gas phase which, however, can adsorb on the surface from isotropic trajectories (no preferential directions).

For the first experiments the same set of spiral-out parameters has been used as for the experiments shown in Figure 35. As expected due to the proposed model, the final pad is flat and shows no terraced structure (Figure 38a) due to the elimination of a preferred directional flux component and the entailed shadowing effects (see chapter 4.1.3.3). However, due to the missing gas supply, the final pads have only heights of about 5 nm which can be seen by AFM height cross sections in Figure 38d (black curve).

To introduce higher barriers which should then reflect any tendency of a directional diffusion component, we increase the total exposure time to 5000 µs (Figure 38 b). Again, the morphology of all sectors is symmetrical and do not show any terraced structure. By starting in the center of the pad, most of the precursor molecules are consumed there. When the beam moves further outward, these areas are already depleted, fewer precursor molecules are available, which leads to a pyramidal shape. This can be seen by the AFM height cross sections in Figure 38d (blue curve). In addition to the depletion, many precursor molecules have already desorbed from the surface which explains the decaying tendency for outer areas.

The essential information, however, is that no lateral asymmetries in X or Y directions are found which proves a homogeneous surface diffusion situation for the area considered giving further indication that the directional gas flux is responsible for the terraced structure found for SO experiments in Figure 35.
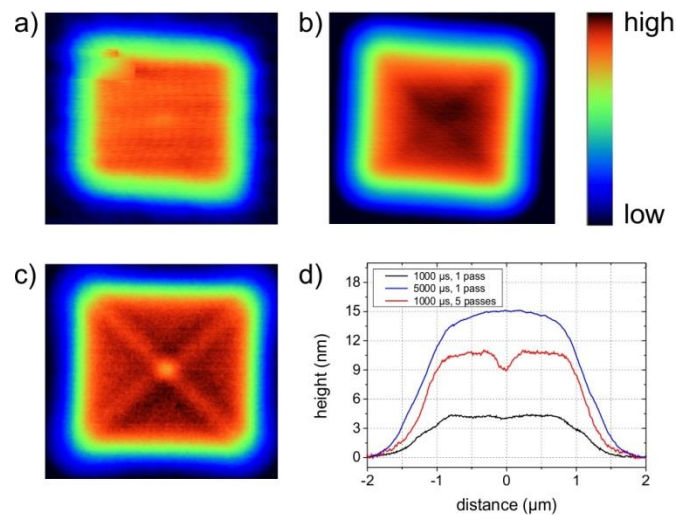
Figure 38: AFM height images for SO pads with closed GIS and different dwell times of 1000 µs (a) and 5000 µs (b). c) Spiral-out with 1000 µs Dwell time and five passes. d) AFM height cross section of all deposits measured from left to right over the central. Please note, the colored height scale bar (top right) was adapted for each picture to emphasize the morphological variations. Therefore, the images are not directly comparable to each other.[49]

By splitting up the TET of 5000 µs into 5 passes (DT = 1000 µs) another effect appears at the diagonals and the center (Figure 38 c). The depletion at these areas is related to the extended residence time of the electron beam at the diagonals: theoretically, only one pixel is exposed, but in practice due to the broad electron beam and the widely spread surface radius of the electrons, also the proximity of the pixel is affected. Along straight scanning paths, each patterning point is influenced by the same amount. However, for spiral-out strategies, the electron beam stays comparable long in the middle of the pad at the beginning which quickly depletes these areas. When consecutive patterning points are within this depleted area, the decreasing coverage leads to lower VGRs and by that to a central indent center. This can be clearly seen by the according AFM height cross section in Figure 38d (red curve). The same argumentation holds for the diagonals where the e-beam changes its direction which is equivalent to a longer local exposure leading to stronger depletion and by that to slight trenches at the diagonals. The absence of any lateral asymmetry shows furthermore that surface diffusion is capable to replenish the area isotropic which gives final indication that surface diffusion effects are not responsible for the levelled structures observed for the experiments in Figure 35.

From these experiments it can be concluded, that the different height levelled morphology is caused by the directional gas flux and not by an isotropic surface diffusion effect.

4.1.6   Eliminating surface diffusion

To strengthen the above discussed finding of a negligible influence of surface diffusion, the finite difference simulations discussed in chapter 4.1.3.4 has been repeated with varying surface diffusion coefficients.[49] In more detail, the diffusion coefficient D_0 was set to 6.5×10^{-9} nm^2/s and 1×10^{-11} nm^2/s

representing very high and practically no surface diffusion, respectively. For more details to the simulations (done by Dr. Jason Fowlkes at the Oak Ridge National Lab, Oak Ridge, TN, USA) and a movie showing the dynamic growth of the deposit we refer to the supplements in Winkler et al.[49] As can be seen by time resolved height simulations in Figure 39 (left), there is a negligible influence found between high and extremely low surface diffusion. Considering the 3D evolution including the depletion regions, shown in Figure 39 at the right for high (top) and very low diffusion (bottom), it is again evident that the surface diffusion is influencing neither the VGRs nor the asymmetric morphology.

In extension to the experimental findings in the previous section, also finite difference simulation suggest that the directional gas flux component together with shadowing effects are responsible for the destabilized morphologies while surface diffusion plays a minor role.[49]
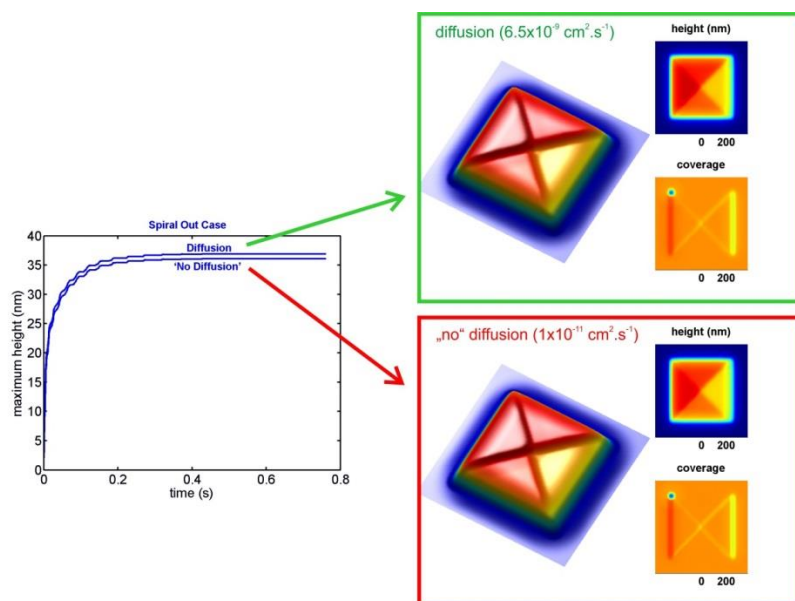

Figure 39: simulating a SO pad with diffusive replenishment (green box, D0 = 6.5x10-9 nm2/s) and "without" diffusion (green box, D0 = 1x10-11 nm2/s). There is quasi no difference in terms of morphology observable.[49]

4.1.7 Pattern rotation

Finally, the correlation between GFV direction and level distribution for spiral-out patterns has to be investigated. As discussed in chapter 4.1.2.2, the direction of the GFV was experimentally determined to 75° in good agreement to the value of 72° found via gas flux simulations. The following experiments show, that this values are not only valid for the single pillars simplification used before, but also valid for 3D-pads.
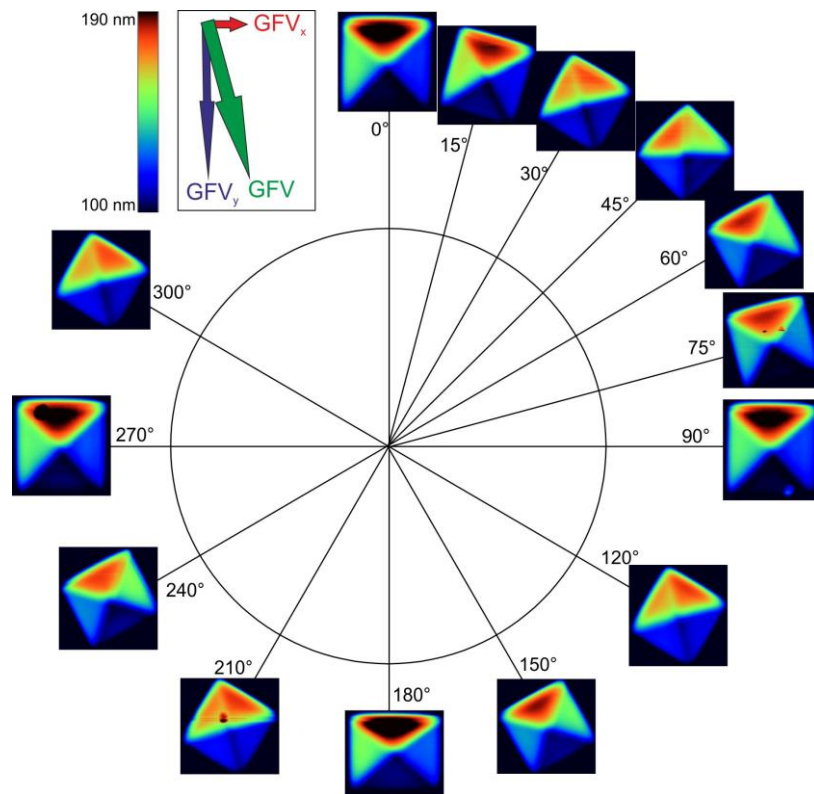
Figure 40: AFM height images of rotated SO pads. No morphological difference shows up by rotating for 90°. When the GFV direction correspond to the direction of an edge or a diagonal of the pad (~30° and 75°) two sectors show the same terraced height. Left top: GFV and its components; colour scale bar for all pads.

For this purpose we rotated a SO pattern in 15° steps clockwise up to 90° and in 30° increments up to 300° respectively afterwards (Figure 40). Two main insights could be gathered:

1) No morphological change is observed when rotating a pad for 90°. That is not in contradiction to the rotated serpentine experiments, because for SO strategy it does not matter in which of the four directions the beam starts, the growing deposit has always the same shape.

2) When one pad edge shows exactly in the direction of the main GFV we get the same qualitatively shape as simulated in Figure 35b. The sectors 2 and 4 have for this patterning rotation the same height, which is indeed the case for the pad with 75° in Figure 40. This result confirms the suggested direction of the main GFV.

Another symmetric situation shows up at a pad rotation of 30° where the two front segment and the two back sectors respectively shows the same height. At this rotation angle the main GFV is parallel to a pad diagonal. With a quick geometrical calculation, again one gains an angle of 75° of the GFV in relation to the X-axis.

These rotation experiments were also performed in opposite direction outwards (anticlockwise) and showed identical results. Even for reversing the total point sequence (spiral-in) the symmetrical situation for 75° and 30° was confirmed.

By that, it is clearly shown that the orientation of the GFV with respect to the deposit front ultimately determines the achievable symmetries due to the directional gas flux and the shadowing effects arising during growth.

4.1.8 Compensation strategies

In the previous chapters it was shown by experiments and simulations that the directional gas flux component in combination with morphological barriers induce shadowing effects which lead to strongly destabilized growth modes. It was also shown that surface diffusion is of minor relevance for the observed effects which allows consideration for compensation.

Hence, to avoid disrupted morphologies, the effect of the directional gas flux replenishment has to be reduced. This can be done by two approaches: *1)* reducing the height of the morphological barrier which eliminates geometrical shadowing; or **2)** establishing a precursor regime with very high molecule coverage where geometrical shadowing is of minor importance due to minimized replenishment demands. To account for both effects, we have systematically varied the beam currents (4.1.8.1) and the dwell times (4.1.8.2) while keeping the total exposure time constant.

4.1.8.1 Current variation

The experiments uses the same process parameter as before (SO, 2x2 µm footprint, 5 kV, 1000 µs DT, 13 nm PoP, single pass pattern of 24 s total exposure time) but with varying beam currents for each pad (5, 25, 98, 400, 1600 and 6300 pA). Figure 41 shows the expected decreasing deposit volumes (red, left axis) with decreasing beam current due to the decreasing number of electrons. In contrast, the deposition efficiency (blue, right axis) increases for decreasing beam current. This is in agreement considering the precursor working regime as for very high currents the working regime is strongly MTL (approaching a more stable value) while the situation gets more balanced for low currents (increasing volume growth rates).

More importantly, the morphology also changes with decreasing currents towards flat appearances as can be seen by the AFM height images in Figure 42. In particular, the height difference between sector 1 (highest front segment) and sector 3 (lowest back segment) is of main interest and plotted in Figure 42 (central graph). As can be seen for currents of 1600 pA and higher the height difference comes to a constant level of about 60 %. Decreasing the beam currents lead to less height differences which comes to zero for currents below ~ 25 pA.

To explain this behaviour we have to look at the replenishment mechanism of chapter 4.1.3.2 at the deposit backside again, considering the change of deposit heights. When the deposit gets very high, the shadow radius exceeds the diffusion lengths Δr_S leading to a reduced replenish by surface diffusion (surface related replenishment, SRR). According to the model in chapter 4.1.3.3 (summarized in Figure 35), it is obvious that most of the replenishment originates from surface adsorption and downwards diffusion (DRR) at the backside supported by re-adsorption effects (SSR – RA). This effect is facilitated by the fact that higher beam currents lead also to stronger depletion resulting in very strong replenishment demands. The saturation for high currents in Figure 42 (> 1600 pA) suggests that the direct gas flux adsorption and downwards diffusion is the exclusive replenishment mechanism as they are constant independently on the used beam currents (green bar on top of the graph in Figure 42).
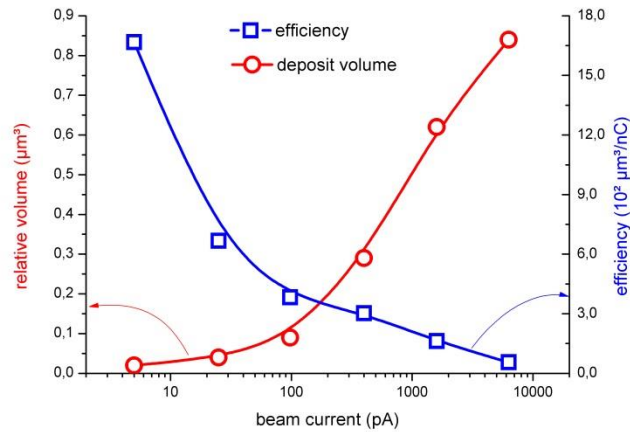
Figure 41: deposited volume (left axis) and efficiency (right axis) of spiral-out deposits for varying beam currents. All patterns used 5 keV, 13 nm point pitch, 1000 µs dwell time via single pass pattern using serpentine strategies (footprint 2x2 µm, total exposure time 24 s).

For very low beam currents the initial barrier is lower, therefore the shadowing radius Δr_S gets smaller than the diffusion length. Consequently, surface related replenishment (SRR) can contribute too (see Figure 42 top). Also the lower beam current reduces the local depletion resulting to lower replenishment conditions. This leads to the situation that surface coverage is always very high, replenishment requirements are very low and geometrical shadowing is of less relevance. Hence, for very low currents (< 25 pA) no segmentation is observable.

As the surface adsorption and downwards diffusion (DRR) is constant (green bar on top of the graph in Figure 42) the decreasing height differences for lower currents can be assigned to increasing surface related replenishment (SRR) effects which are qualitatively indicated by the blue bar on top of the graph in Figure 42.

From these results it can be concluded that two effects has to be established when aiming for flattest morphologies: *1)* low barrier heights to prevent geometrical shadowing; and *2)* low depletion to reduce replenishment demands during patterning. The problem, however, is the fact that both effects are entangled with each other which requires therefore a combined approach as will be discussed in the following chapter.
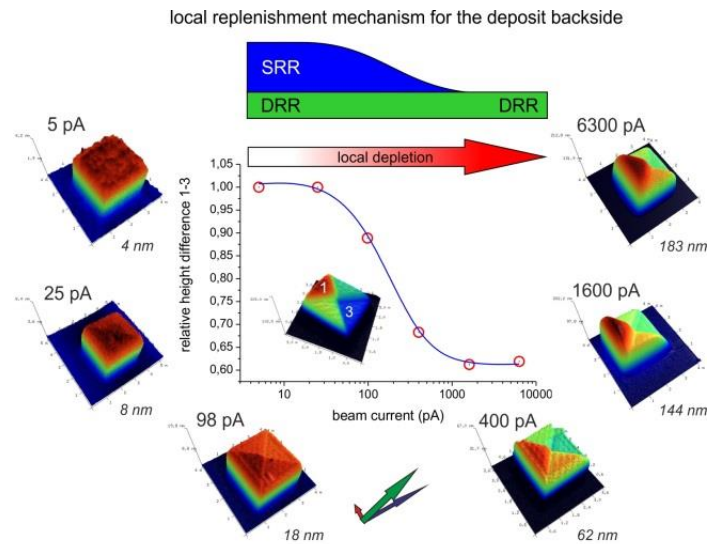
Figure 42: beam current variations for SO pads. The mean deposit heights change from 4 nm to 183 nm. With increasing beam current, the local depletion increases and the shape gets more and more segmented. The inset shows the height difference between sector 1 and 3 as a function of beam current. The contribution of different replenishment mechanism for the deposit backside is indicated schematically on top of the figure.[49]

4.1.8.2   Dwell time variation

As the final deposit height is often invariable due to the intended purpose a workaround has to be found. One approach is dividing a single pattern at high DTs into multiple patterns with short DTs which result then in lower barrier heights per patterning frame. This has also the advantage that the depletion is reduced due to the shorter single point exposure which should shift the precursor regime towards a more balanced situation.

Hence, we fabricated 7 SO-pads but varied the pixel dwell time DT for each pad (1, 5, 10, 50, 100, 500 and 1000 µs respectively). To provide comparability the total exposure time was kept constant to 1000 µs, therefore pattern with shorter DTs were looped several times (1000 passes for DT 1 µs, 200 passes for DT 5 µs, …).

The result of such a series is shown in Figure 43 by directly comparable AFM height images. As evident, reducing the DT from 1000 µs to about 50 µs, the levelled structure disappears as expected. When going to even shorter DTs an additional effect appears by means of a central indent and diagonal trench formation (see left hand side in Figure 43). These features emerge due to the decreasing frame times (= time until the electron beam returns to the same pixel), which reduces the prematurely diffusive replenishment. The same effect has been observed in chapter 4.1.5 and Figure 38c together with a detailed explanation about its origin.

A striking feature, however, is the fact that the asymmetry is only visible for highest dwell times as the consequence of the directional gas flux effects. For lowest dwell times, although destabilized, a symmetrical appearance is found which indicates that the destabilization is not caused by the directional gas flux but rather by strong depletion effects as described above. Hence it follows that the trench / intent formation should decrease if depletion is reduced which could be established via decreasing current. To investigate the system on this hypothesis, the same DT sweep has been

Master Thesis, Robert Winkler

performed for decreasing currents ranging from 1600 pA to 5 pA while deposition parameters have been kept constant.
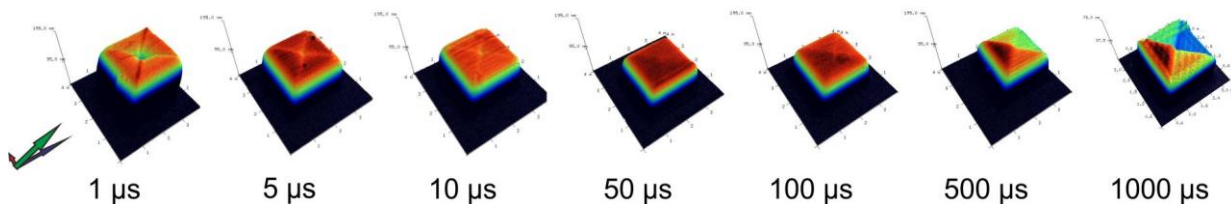

Figure 43: variation of the dwell time for SO pads with patterning conditions of 5 keV, 1600 pA and 13 nm PoP. To provide the same electron dose for each pad, the number of passes was adapted. When going to lower DTs the terraced structure disappears and trenches develop.[49]

Evaluation has been performed via AFM height analysis and its distribution by means of height histograms (Figure 44a). As seen before, for high DT (1000 μs) the top surface of the deposit is levelled in 4 sectors, therefore 4 peaks appears in the histogram. The deposit with 50 μs DT shows an equally high, flat surface, resulting in a very sharp peak in the histogram. The morphological instabilities for very short dwell times (trench, central indent) produce a broadened, asymmetric peak.

As the base width of the peak (Figure 44b) is related to the instability of the deposit it gets obvious that for extreme DT the morphology is disrupted, however due to different mechanisms (Figure 44c horizontal arrow). When the beam current is lowered (see legend), the precursor working regime is shifted from MTL to RRL conditions (Figure 44b vertical arrow), which reduces the depletion / replenishment related effects and therefore morphological instabilities are decreased (4.1.8.1).

The results of additional numerical calculations (done by Aleksandra Szkudlarek and Ivo Utke[49]) for a beam current of 1600 pA (Figure 44c) show the relation between the two main replenishment mechanism during a DT sweep. Assuming a constant impinging gas flux the relation will change due to the increasing contribution of the surface diffusion replenishment. At DTs of around 20 μs the diffusive replenishment has its maximum, which suggested more balanced conditions and coincides perfectly with the flat pads of the experimental results at this DTs (Figure 43). This is in very good agreement with the lowest height differences for all currents Figure 44b suggesting the most balanced situation. Further DT decrease results in less diffusive replenishment due to the lower concentration gradient. This leads to a coverage situation which is more sensitive to local depletion effects, preferably occurring at the center and at the diagonals as discussed in chapter 4.1.5 which is equal to more MTL like precursor conditions.

By that it can be concluded that for special pattern shape / strategy situation there exists two different MTL regime, however, based on different mechanism: *1)* directional gas flux effects for high DTs; and *2)* diffusive replenishment issues for low DTs.
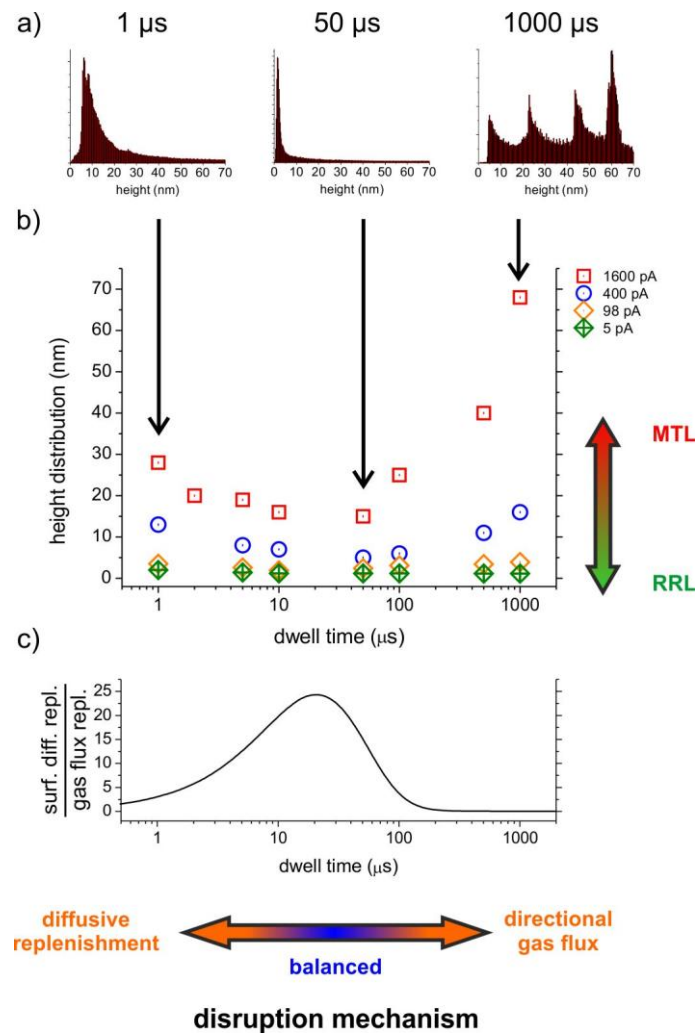
55

Figure 44: analysing morphological instabilities: a) Height histograms µs shows the most frequently measured heights for a beam current of 1600 pA for dwell times of 1, 50 and 1000 µs. The base width of each peak in the histogram is plotted in b) for all pads. c) numerical calculations to estimate the contribution of the different replenishment mechanism are in best agreement to the experimental results in b).[49]

4.1.9 Summary: directional gas flux effects

At this point we want to sum up the results gathered so far. First, we showed experimentally, that the gas flux simulator (4.1.1) provided by Friedli and Utke[47] is appropriate to describe the impinging molecular flux (4.1.2.1). By taking the individual deposition site into account, a gas flux vector GFV was introduced (4.1.2.2), whereby the Y-component was found 3.8 times larger than the X-component, which equals an angle of 75° of the GFV with relation to the X-axis in the given arrangement. The importance of the patterning SSA direction with respect to the VGRs was demonstrated by rotation experiments using serpentine strategies (4.1.3.1). The advantage of the interlacing approach because of its invariance to rotations got obvious in 4.1.3.5.

As a central finding, we could assign the shadowing effect to be responsible for most of the morphological effects (4.1.3.3). While the front side is always replenished directly via the directional gas flux, the shadowed backside of the deposit can mainly be replenished *1)* via molecular

downwards diffusion from the deposit surface; and **2)** via surface diffusion from surrounding areas. While the former effect is widely constant, the latter effect strongly decreasing for increasing deposit heights.

To make the contributing effects more obvious, the spiral-out patterning strategy was introduced, which shows a disrupted shape in experiments as well as in simulations (4.1.4). By shifting the deposition area towards the Y-axis, the size of the GFV_X was reduced (4.1.4.1), which emphasize the need of a correct GIS alignment. In addition, a steep nozzle and a deposition size close to the X-axis was proposed in order to reduce the shadowing effect (4.1.3.6).

But not only the geometrical alignment can be improved, we can adapt the current and dwell time as well to get stable deposition conditions (4.1.8). It was shown that for low currents the surface gets flat (4.1.8.1), however with the drawback of a low VGR. In experiments with varying dwell times it was demonstrated, that there is an optimum range, where the working regime is equal in each point of the patterning footprint (4.1.8.2).

With these achieved knowledge about the gas dynamics effects we can proceed to the aim of an optimized morphology, which will be the topic of the next chapter.

4.2   Morphology optimization

The main aim of the following chapters is the deposition of a perfect cuboid with a squared footprint (2x2 μm, height does not matter). Assuming an optimized GIS alignment, there are still many parameters left to improve for the best shape performance.

In a first step, we will compare different scan strategies (4.2.1) and discuss their individual problems. As will be shown, the serpentine patterning strategy is not perfect but nevertheless most preferable for the shape optimization.

After that, we take a closer look at the edges and corners of the deposit and will discover two fundamental effects: lateral base broadening (4.2.2.1) and top edge rounding (4.2.2.2). For latter we introduce a compensation procedure via a dynamic adaptation of the dwell time at edges and corners (4.2.2.3).

In a last step we investigate the morphologies for different parameter set for beam current and dwell time to find a balanced process window for an optimal shape performance (4.2.3).

4.2.1   Scan strategy

As demonstrated in the previous chapter, the scan strategy is very important for the shape performance. Therefore, we have first to identify the most beneficial strategy and try to find an optimized set of parameter. At first sight, the serpentine and the interlacing strategy seems to be suitable for stable morphologies, whereas the spiral-out strategy – although perfect for investigating fundamental effects - shows a disrupted surface if the parameters are not selected ultra-carefully.

4.2.1.1   Spiral-in

The spiral-in patterning strategy (**SI**) can be achieved by simply reversing the patterning sequence of the spiral-out pattern (page 29). Similar to the spiral-out strategy the spiral-in shows a disrupted morphology (Figure 45a) and is therefore not suitable for shape optimization purposes. However, the new structure gives us the opportunity to test our directional gas flux hypothesis.

In contrast to the 3D-pads fabricated via SO, the spiral-in strategy initially build up a fence of the footprint size (Figure 45b, Step 1). For the following inner spiral lines (Figure 45b, Step 2, deposit line number 7 and 9) different precursor densities are present due to the shadowing effect. Therefore, the front sector gets less high than the back sector. Similar explanations – considering the weaker gas flux component in X-direction – lead to the different heights of the right and left sector.
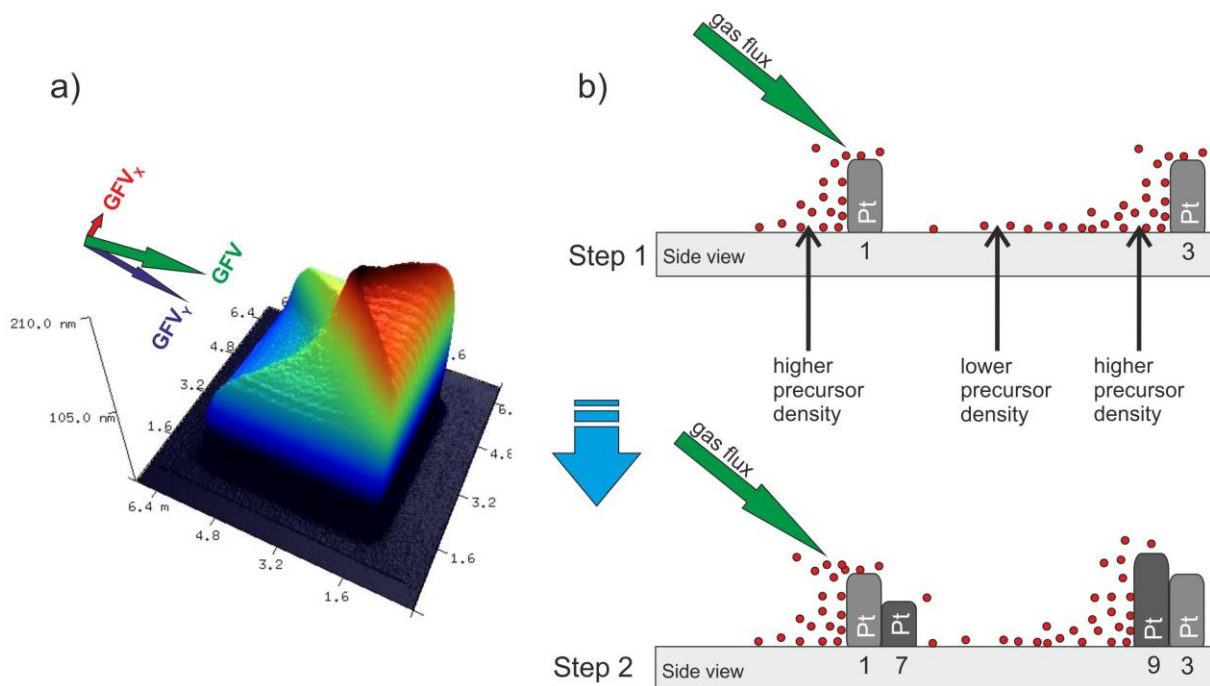

Figure 45: a) morphology of a spiral-in strategy (5 keV, 1600 pA, DT 1000 µs, footprint size 4 x 4 µm). b) Schematic explanation in two steps for the resulting shape by means of directional gas flux (shadowing effect).

In addition, Figure 45a shows the effect of upscaling of the footprint size (in general 2x2 µm → 4x4 µm), which makes the distortion of the surface even worse.

Hence, spiral strategies in combination with very high or very low dwell times are not suited for controllable high-fidelity morphologies. However, they are ideal to serve as very sensitive test-vehicle to visualize regime changes or directional gas flux effects.

4.2.1.2   Raster vs. Serpentine

The last patterning strategy considered was classical raster scanning (3.4.1.1). This patterning mode is implemented in the patterning engine of the DBM and routinely used in many cases. Therefore, it is essential to have a closer look at this strategy and compare it to the also often applied serpentine strategy. In Figure 46 (centre) the shape problems by using the raster strategy get obvious. The high ridge at the starting points of each line can be explained by the following considerations: the exposure of the first point deplete its proximity, especially the consecutive patterning point and the starting point of the next scanning line as well. The consecutive pixels have to deal with already depleted conditions and therefore VGR suffers. In the meanwhile, the depleted starting point of the next scanning line has enough time for replenishment until the electron beam returns. Therefore, the starting edge is always better replenished than other patterning points and the decaying behaviour along a single line can be understood as direct visualization of dynamic depletion. In comparison, a serpentine pad fabricated with the same process parameter is shown in Figure 46 on the right. Although not perfect, the shape performance is here much better but shows a downwards bow on both sides where the beam returns which will be discussed in chapter 4.2.3.3.

Concluding all investigated patterning strategies it can be stated, that for the purpose of stable morphologies and equal flat topologies the serpentine strategy is the most favourable. The interlacing strategy also shows good properties (invariant to patterning rotation, stable surfaces, applicable to more complex footprints), however interlacing distance and process parameter have to be mutually agreed, otherwise unwanted features destroy the aimed shape.

From that point of view the strategy of choice is the serpentine, which we will investigate in more detail in the following sections.
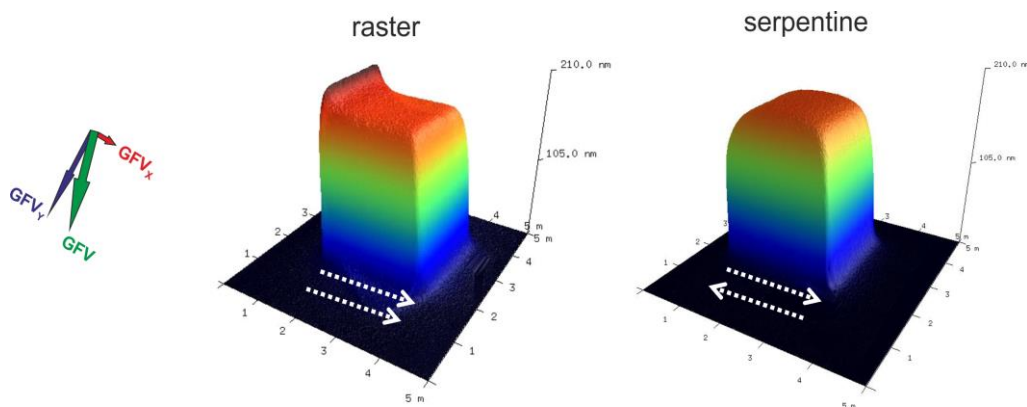

Figure 46: 3D-AFM image of a deposit fabricated via raster patterning strategy (middle) and a via serpentine patterning strategy (right). The used process parameter were in both cases 5 keV, 1600 pA, DT 1 µs and 1000 passes. On the right, the belonging gas flux vector for both cases is shown. The dashed white lines indicates the patterning directions (FSA).

4.2.2 Intrinsic shape effects

As it can be seen in Figure 46, there are still shape problems at the edges and at the base. Therefore, we have to identify the source of these deviations from ideal shapes. The problems arise from the fact, that the deposit is finitely and electrons can leave the intended deposition footprint. As these boundary surfaces are not avoidable, one speaks of intrinsic shape effects.

We can identify two different effects, one acting especially at the base and the side walls (4.2.2.1), the other explains the rounding of the top edges (4.2.2.2). Both are not completely avoidable, but for the second, a compensation approach is presented (4.2.2.3).

4.2.2.1 Lateral base broadening

By measuring the 3D-pads with the AFM, the first observation was a deviation of the patterning footprint of 2x2 µm. All deposits get 200 nm – 300 nm broader in X- and Y-direction. This value is too large to accuse the beam diameter or AFM-tip related problems. Drift issues during patterning or stage drift during AFM measurements can be excluded too.

To interpret this enlargement we have to consider electrons outside of the patterning footprint. Four sources of dissociating electrons are possible:

Electron beam diameter: as the electron beam is not infinitely small, the deposit itself is broadened by the beam tails. Once these additional areas grow they achieve their intrinsically minimum which is a complex interplay of electron trajectories and deposit chemistry[53]. For 5 keV and the used precursor this additional broadening lies in the range of about 20 nm per side.[53]

1) **Side walls: forward- / back-scattered electrons**: many electrons can exit the deposit at the sidewalls in forward or backward direction (FSE and BSE, respectively) triggering additional dissociation and by that contribute to further broadening. This effect is even stronger for MTL conditions due to the excess of electrons while for strong RRL conditions most of the electrons are "consumed" before they can lead to additional side wall growth.

2) **Surface BSE**: as mentioned in point 1, about 50 % of the electrons are outside the patterned area and they can enter the substrate. Based on its chemistry (Si for this study) the BSE radius is much larger (about 300 nm per side) where BSE and subsequent secondary electrons (SE) of type 2 (SE_2) can be generated which lead to additional deposition.

The BSE distribution can be simulated (Casino version 3.2.0.4)[54] by leading the electron beam from the center towards the deposition edge with the same PoP as used for the experiments. The simulation shows a qualitatively confirmation of the broadening effect, although the effect is not as pronounced as in the experiments (Figure 47 right). Additional to the enhanced number of electrons at the base we have to consider the enhanced number of available precursor molecules due to the fact, that these areas were not exposed before also replenished via surface diffusion. Both (high number of electrons and high number of precursor molecules) together leads to a very high deposition rate at the base. This explains the additional deposited material in the experiments. Please note, SE show the largest dissociation cross section, but for a qualitatively approximation it is convenient to investigate the trajectories of the BSE as they can trigger SE_2.

As the effect 1 and 2 discussed above geometrically depend on the deposit height, the broadening is supposed to be different for current variations. In contrast, the interaction volume dramatically changes when taking the different material of substrate (SiO$_2$, density = 1.74 g/cm³) and deposit (PtC$_5$, density = 7.96 g/cm³)[12] into account (Figure 48). For low deposit heights (e.g. for low currents) many electrons enter the low-density-substrate. Therefore, the surface radius of BSE is increased (Figure 48, top row) and the interaction volume effect mentioned above dominates. Even patterning points in quite a distance (BSE surface radius) to the edge can contribute to the lateral base broadening.
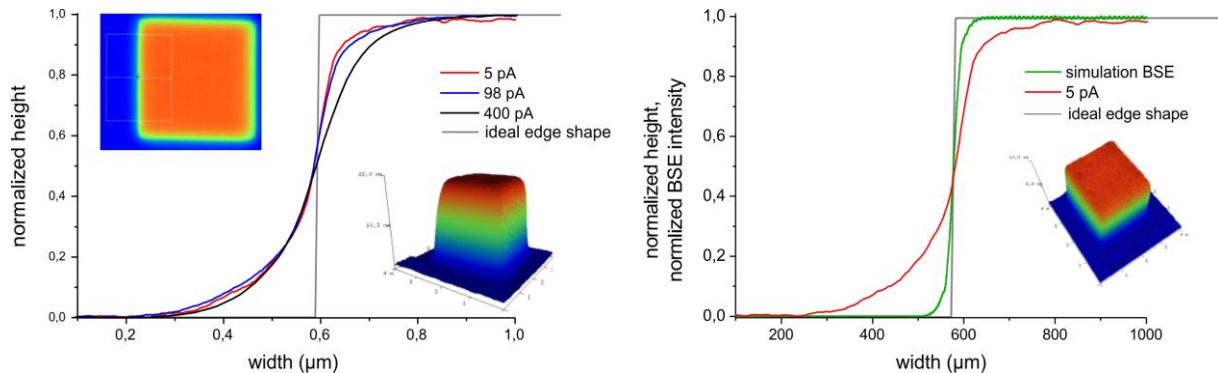

Figure 47: AFM height measurements of different deposit edges in comparison to the ideal edge shape and simulated BSE distribution. In the insert (top left) the evaluated area for the cross section is indicated. The graph on the left shows the deviation of an ideal edge shape in dependency of the beam current. In the graph on the right, the experimental normalized height data for a deposit with a beam current of 5 pA is compared to the ideal edge shape and the simulated BSE-distribution when the electron beam heads towards the edge. In all cases two intrinsic effects are observable: lateral base broadening and top edge rounding.

When the interaction volume is fully located inside the deposited material (e.g. for high currents after some certain growing time), most of the BSE are confined to a smaller area (Figure 48, bottom row). In addition, the backscattering coefficient increases from 0.11 (SiO$_2$) to 0.33 (PtC$_5$). Patterning points with more than 100 nm distance to the edge do not significant contribute to the lateral base broadening any more. However, the geometrical effects (mainly sidewall and FSE-effect) get even stronger.

Please note that the effects strongly also depend on the primary energy due to the strong dependency on the interaction volume. Schmied[6] already showed proximity effects in dependency of varying beam parameters in the FEBID process, where also a chemical change was observed.

Summing up, we found a lateral broadening of the deposit at the base (Figure 47). This behaviour was explained with the enhanced number of electrons, which was supported by simulations, and an increased number of available precursor molecules. As it can be seen in Figure 47, another effect appears at the top edges, which will be discussed in the following section.

4.2.2.2   Top edge rounding

In addition to the lateral broadening at the base, a top edge rounding effect on top appears (Figure 47). In contrast to the ideal shape, there is less deposition at patterning points close to the edge.

Responsible for that reduced volume growth at edges and corners is the reduced number of dissociating electrons coming from neighbouring patterning points (Figure 49). In addition to the Gaussian distributed intensity profile of the electron beam, we can define an action radius for dissociating electrons whereby the number of contributing electrons decreases radially. Descriptively an amount of initial electrons gets lost to the proximity. These electrons are one of the sources resulting in the lateral base broadening effect discussed before as they trigger a deposition, when they hit the surface again. The proximity effects during the FEBID process were investigated in more detail at our institute in the master thesis of Roland Schmied.[6]
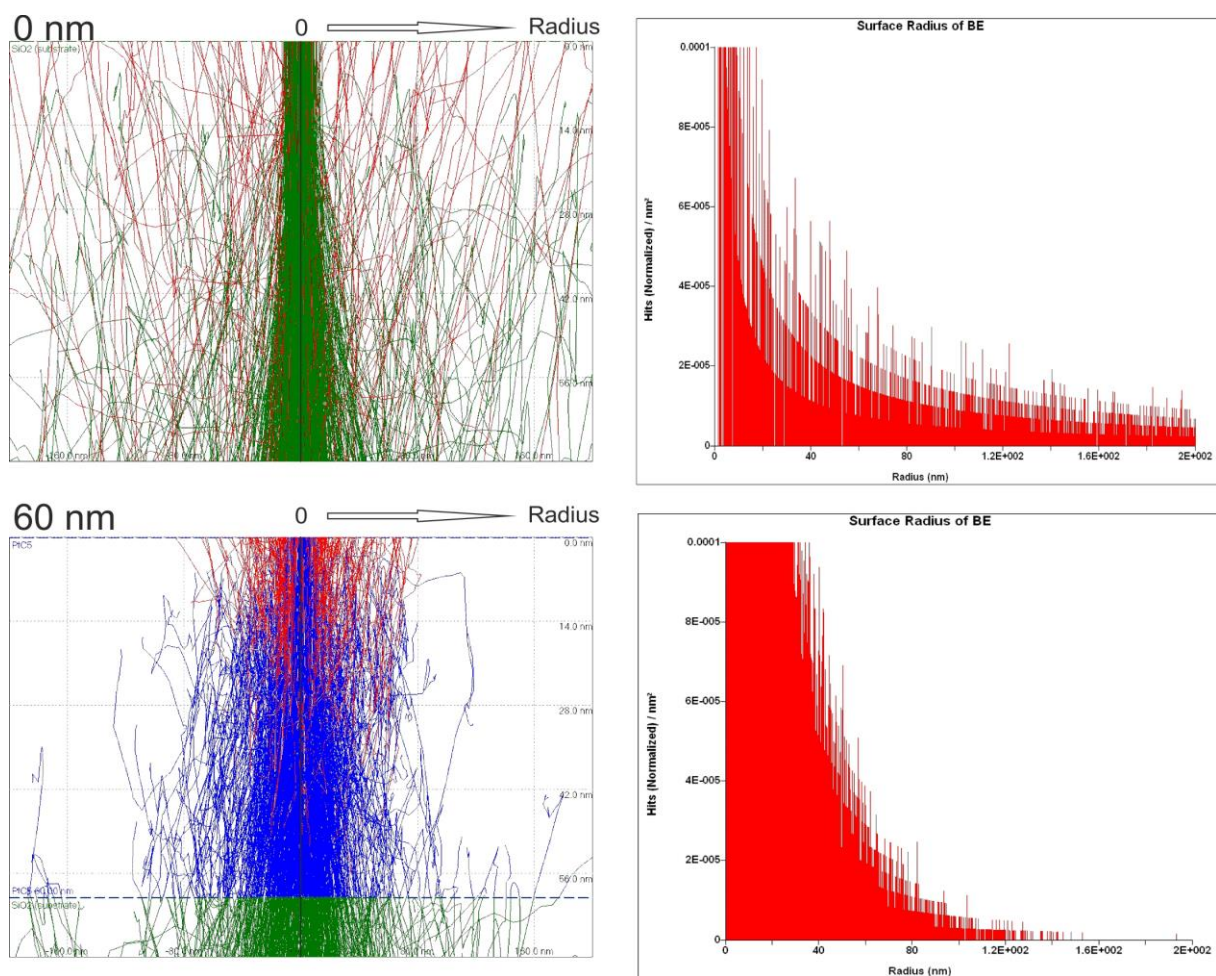

Figure 48: Monte Carlo simulation (Casino v.2.4.8.1)[12] of penetration depth and surface radius of the BSE for substrate (SiO$_2$, top row) and deposit with a height of 60 nm (PtC$_5$, bottom row). The red trajectories on the left indicate the electrons which re-exit the surface/deposit again (BSE). The graphs on the right sum up the number of the re-exiting BSE as a function of the radius starting from surface position 0 to radius (indicated in the left pictures).

Assuming a patterning point in the center of the footprint, electrons migrate to adjacent areas, but on the other hand, the same amount of lost electrons comes back from the neighbouring patterning points as shown schematically in Figure 49. The situation is different, if a patterning point at the edge of a 3D-deposit is exposed. As discussed above, many electrons leave the deposit at the sidewalls, but in contrast to a central point, fewer electrons return to an edge-patterning point due to the fewer neighbours.

This consideration is not only valid for the outer edge points, but also for patterning points within a distance to the edge smaller than the action radius. In particular, corners are affected to a high degree due to even less adjacent patterning points. The deviation from the ideal shape decreases by lowering the beam current as a more RRL working regime counteracts the top edge rounding effect due to enhanced diffusive replenishment (4.2.3.2). According to the changing interaction volume there is also a dependency on the primary energy and on the material of deposit and substrate, respectively.

If the patterning footprint is reduced, more relative pixels are EPP. Therefore the effects of the top edge rounding get even stronger. Therefore, it is obvious, that the top edge rounding effect gets very critical for narrow deposits. We identified the lack of electrons at the edges and corners as responsible for the rounding of the top corners. Fortunately, we can compensate that to a certain extent. In the following section, we will present the attempt to compensate the top edge rounding.
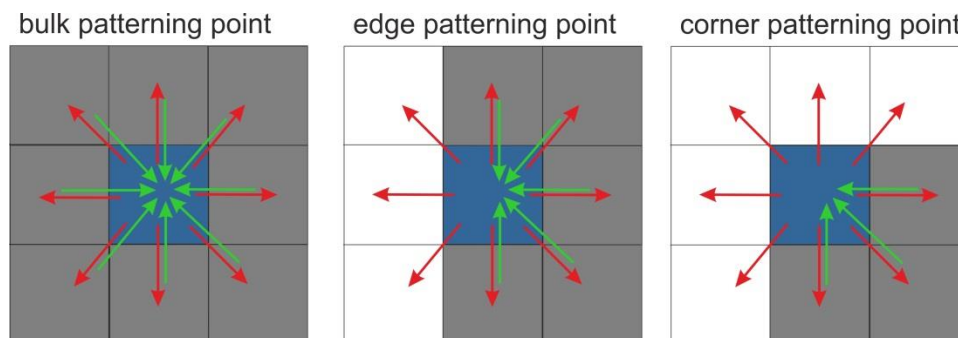

Figure 49: schematic explanation of the top edge rounding effect. The considered patterning point is shown as blue square, adjacent patterning pixels are grey, the white squares are areas outside of the patterning footprint (vacuum). The red arrows indicate electrons that get lost to neighbouring patterning pixels, the green arrows are electrons that origin from other patterning points but contribute to the considered pixel. It can be seen, that a patterning point within the bulk (left) statistically receive as much electrons to the neighbourhood that it has emitted. For edge patterning points (middle) and especially for corner patterning points (right) electrons are lost to the vacuum.

4.2.2.3 Top edge rounding compensation

There are two possibilities to compensate the top edge rounding effect:

1) **Diffusion enhanced working regime**: An enhanced surface diffusion counteracts to the top edge rounding effect. This method strongly depends on the process parameter and is therefore only applicable for a small range of parameter. The underlying effect is discussed in more detail in chapter 4.2.3.2.

2) **Dwell time correction for edges and corners**: The basic idea is to compensate the missing electrons at edges and corners with a longer dwell time. This method does not require ultra-careful parameter settings and is therefore rather easy for a general use. The following experiments show the effect of different dwell time correction approaches.

First task is the estimation of the action radius, which gives us an idea which points are affected. According to Figure 47 and Figure 48 (bottom row) a distance of at least 100 nm to the edge is influenced by the top edge rounding effect. This corresponds to about 7 patterning points with respect to the PoP of 13 nm.

The next considerations concern the lack of electrons for an edge patterning point (**EPP**) or a corner patterning point (**CPP**) in relation to a bulk patterning point (**BPP**). Assuming 8 nearest neighbours for BPPs, there are only 5 nearest neighbours for EPPs and 3 for CPP. Hence, the normalized electron dose for a BPP is equal to 8/8, for EPP 5/8 and for CPP 3/8. To achieve the same normalized electron dose for each patterning point one has to adapt the dwell time for EPP and CPP. For a more obvious demonstration we over-compensate the top edge rounding effect and chose the dwell time for EPP to 1.6 times the bulk-DT and the DT for CPP to 2.7 times the bulk-DT, respectively. Going towards the pad center, the multiplication factor decreases linearly from 1.6 to 1 for EPP (1.6 →1.51 → 1.43 → 1.35 → 1.26 →1.17 → 1.09 → 1; "edge corrected") and from 2.7 to 1 for CPP (2.7 →2.46 → 2.21 → 1.97 → 1.73 →1.49 → 1.24 → 1; "corner corrected").

To show the compensation process within on pad (and by that providing the same experimental conditions) we manipulated the DT of SP-pads (2x2 μm, 5 keV, 1600 pA, SP1 configuration) in such way, that one edges was edge-corrected, one corner was only edge corrected, whereas another corner was corner corrected (Figure 50). The remaining edges and corners were without correction. As can be seen the left edge is smeared out much more than the corrected edge on the right hand side. Same holds for the corrected and uncorrected corner top left and top right, respectively.
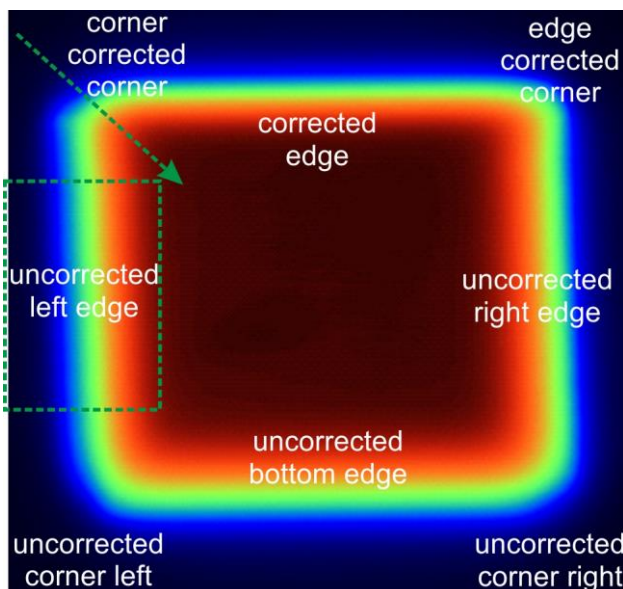
Figure 50: serpentine pad with corrected areas. The dashed green arrow and rectangle representatively indicate one area for the AFM-cross section measurements in Figure 51.

At first, a pad with the bulk DT of 1000 µs was fabricated and afterwards measured with the AFM. To exclude tip problems, the scan direction has been rotated from 0 to 270° in 90° steps and the cross section of the same corner and the same edge has been measured. In all four cases, the curves for the edge as well for the corner were quasi identic, which proves the reliability of the AFM-cross section measurements.

Figure 51 top row shows the edge and corner measurements. The corrected edge and corners are obviously improved, whereby the corner correction reveals in both cases slightly better results. The slope at the top is steeper than in the uncorrected case, however, the intrinsic lateral base broadening especially on the pad base can´t be avoided.

When the bulk DT is reduced to 1 µs (1000 passes to achieve the same TET) the optimization effect gets very clear (Figure 51 bottom row). Especially the corrected edge shows a perfect shape performance. For the corners a simple edge correction seems to be too less progressive, the corner correction reveals a perspicuous improvement. The worse optimization for high DT (1000 µs) in comparison to the low DT (1 µs) is a result of the already depleted situation. An increased DT for EPP and CPP does not make much sense, when the proximity is depleted already within the bulk DT. In contrast, for low bulk DTs the working regime is more shifted towards RRL and more precursor molecules are locally available for the additional electrons.
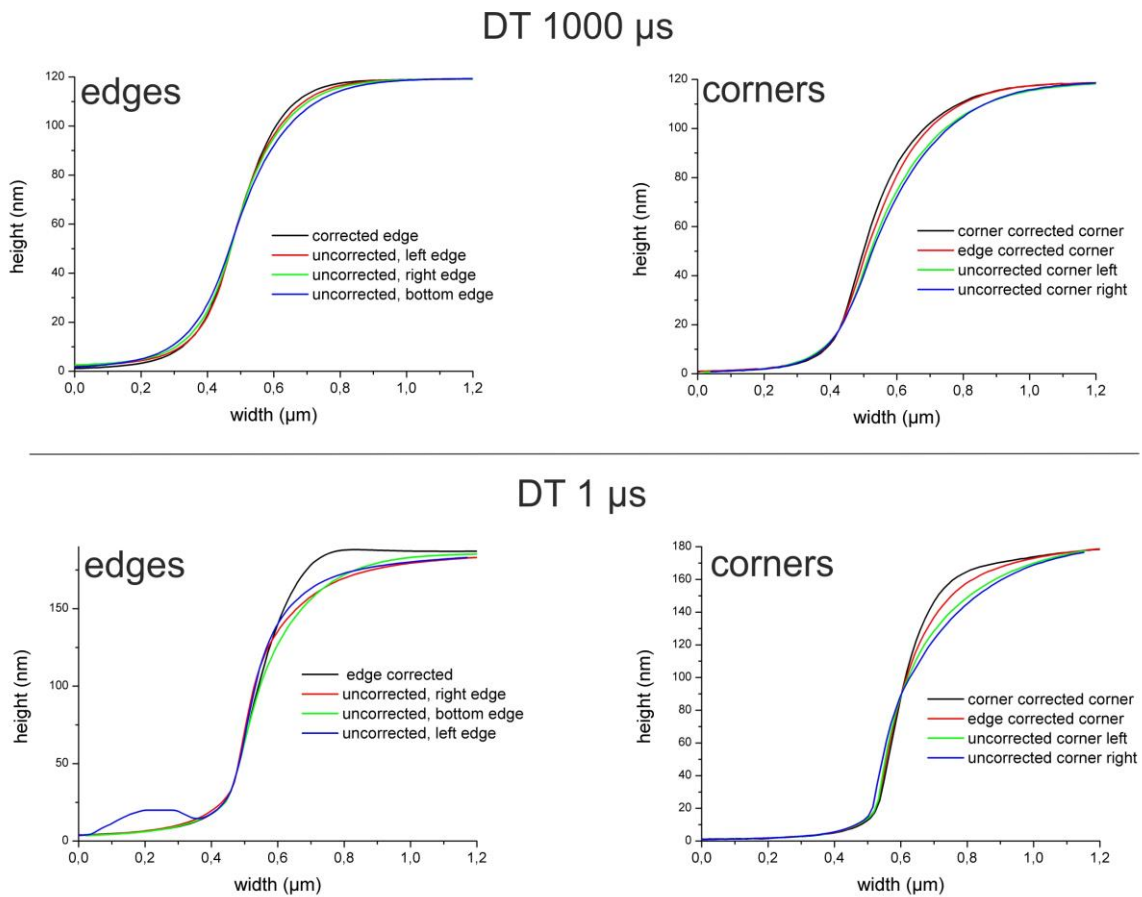
Figure 51: AFM cross sections for SP pads with dwell time 1000 μs (top) and 1 μs (bottom). The graphs on the left compare uncorrected edges to the corrected edge; on the right the uncorrected corners are checked against two different correction types: corner corrected and edge corrected, respectively.

Please note, the results are valid for a beam current of 1600 pA and a primary energy of 5 keV. For different beam currents the top edge rounding effect differs due to the change of the working regime. For details we refer to the next chapter.

4.2.2.4 Summary: shape broadening

By investigating the deposit side walls in more detail we found two intrinsic problems (Figure 47). First, a lateral broadening at the base appears (4.2.2.1), which is explained by electrons which escape at the side walls of the deposit. The second effect is a rounding of the top edges (4.2.2.2) for which missing electrons from proximity points are responsible. That it is possible, to compensate the top edge rounding by supplying additional electrons via adaption of the dwell time, was successfully shown in 4.2.2.3. Both effects are intrinsic and cannot be inhibited totally, but they can be reduced and compensated, respectively.

After the investigation of the borders, we are now interested in the top surface topology. We will see, that the shape can be optimized by selecting the appropriate combination of dwell time and beam current.

4.2.3   Distinctive morphologies in dependence of process parameter

4.2.3.1   Overview

The following sections investigate the different morphologies which appear, when DT or current is changing. The remaining parameters for serpentine patterning strategy stay constant. Primary energy: 5 keV, TET: 1000 µs and footprint size 2 x 2 µm.

Qualitatively four different shapes could be observed: bowl, tunnel, ramp and balanced, (see Figure 52) which can be assigned to different regions in the parameter space (Figure 52). When the patterning direction influences the top surface morphology, the effect is called patterning induced shape effect, otherwise it is called regime induced shape effect.
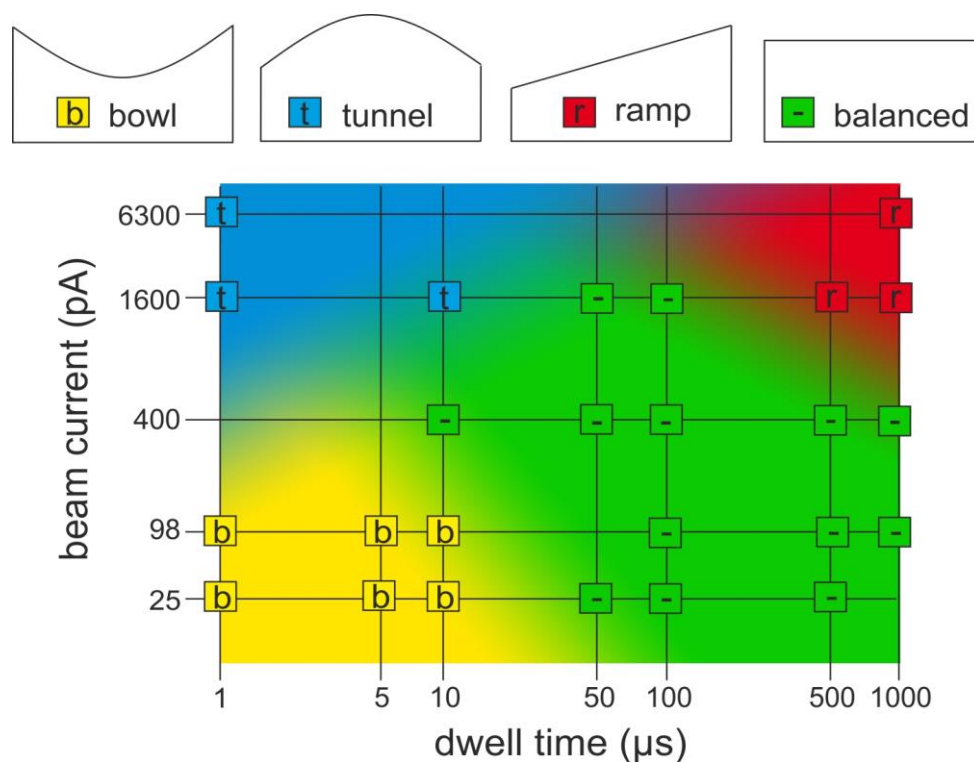

Figure 52: top row: schematic drawings of the four morphologies. Bottom: Overview of the investigated parameter space. Four distinctive morphologies for serpentine deposits (coloured squares) can be associated to different areas in parameter space (coloured regions).

4.2.3.2   Bowl

High corners and a rim at the borders of the footprint area characterize the bowl (bowled shape). This morphology is quite surprising when the effect of top edge rounding is taken into account, where the height tendencies were just reversed. As mentioned before, this counteracting bowl effect can be another possibility for shape optimization by carefully compensating the top edge rounding effect with the bowl effect. Figure 53a shows a 3D-AFM image of a bowl. This morphology is only

achieved, when the experiments were conducted with low beam currents and low DTs (Figure 52, blue area). In terms of working regime, we are located in the diffusion enhanced regime.

The occurrence of the bowl can be conceived by the following considerations: Initially, every patterning point has the same number of precursor molecules. As the electron beam pulses at the same position for subsequent loops, the proximity gets more and more depleted. The main difference between bulk patterning points and EPPs or CPPs is the surface related replenishment. The surface outside of the footprint is fully filled with precursor molecules and due to the concentration gradient the physisorbed molecules start to diffuse towards the deposition area. Before they are able to replenish the central parts of the deposit they are dissociated at the edges and corners or desorbed again (Figure 53b).

In particular, corners are replenished even more efficiently than edges due to two different supply directions. Hence, corners show a higher coverage which therefore leads to a higher deposition rate and finally to the bowled shape.
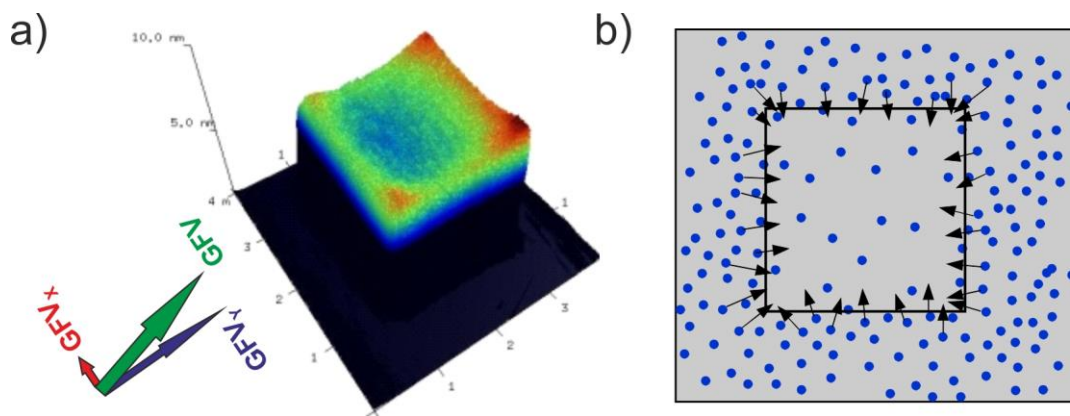

Figure 53: a) 3D height image of a bowled shaped serpentine (25 pA, DT 1µs); b) schematic explanation of the precursor diffusion which leads to the bowl. The black square marks the deposition footprint, the blue dots indicate precursor molecules which diffuse towards the edges and in particular to the corners.

As this theory requires a different replenishment after every loop, the bowl shape is only observable for many loops (and by that for short DTs). Additionally the beam current must not be too high, otherwise the shape would change to a tunnel, which is explained in the next section.

4.2.3.3 Tunnel

As the beam current increases, the deposition height increases too. Therefore, it gets harder for the precursor molecules to get on top of the deposition area and the diffusive effect that generates the bowl disappears and an other morphology is observed.

As it can be seen in Figure 54, there is a curvature outwards, parallel to the FSA. The characteristic tunnel shape suggests locally different depletion/refreshment at the middle of each scanning line and the point of return.
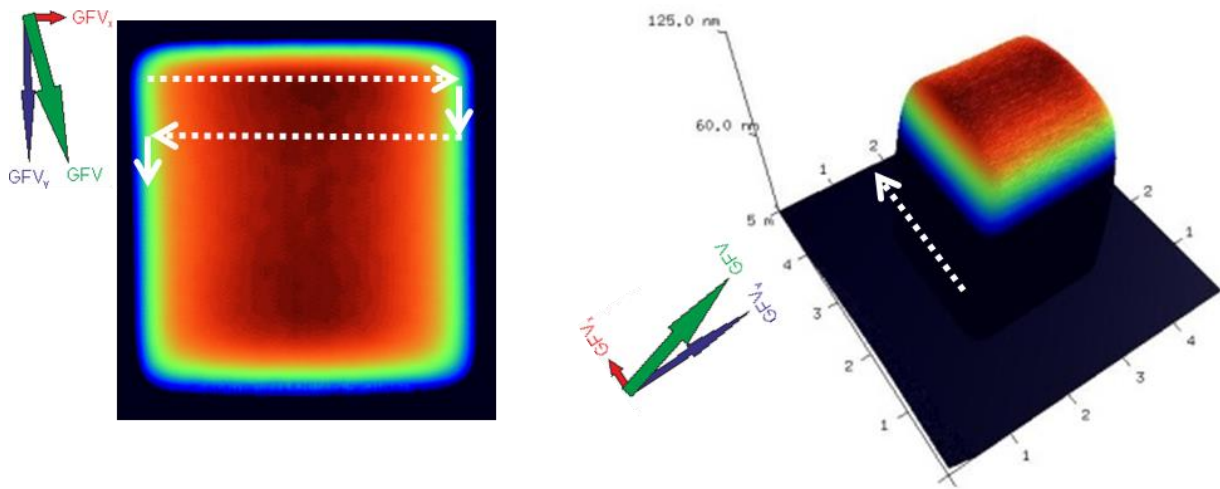

Figure 54: tunnel shape. Height image of a serpentine deposit (left) with DT 1 μs, 1000 passes, 1600 pA and 5 keV. Right: associated 3D-AFM-image. The dotted white lines indicate FSA, the solid line the SSA. The gas flux direction is shown on the left of each AFM image.

As the electron beam scans along the FSA, he leaves a line of depletion. The former patterning points are replenished after a period. After the point of return, the first points of the consecutive scanning line can not be refilled just in time and have still lower precursor coverage. When the beam arrives at the center of the deposition footprint, sufficient replenishment is received, which explains the enhanced growth in comparison to the left and right edge in Figure 54 left.

This enhanced depletion effect at the first patterning points of each line is in principal expected for all serpentine patterns, but two conditions have to be fulfilled at the same time for a tunnelling shape:
1) High currents. Otherwise hardly any depletion happens and no tunnel shape will emerge.
2) Adequate DT. The DT is connected with the scanning speed. If the velocity is to low (long DTs), only few patterning points of the consecutive scanning line are depleted while the other have already enough time to replenish.

This explains, why the tunnel morphology only appears for high currents (1600 pA, 6300 pA) with short DT (1-10 μs). As the position of the curvature depends on the SSA direction, the tunnel effect is a patterning induced shape effect.

4.2.3.4   Ramp

Other extreme settings for parameters are high currents together with long DT, in terms of working regime we are therefore located strongly in the MTL regime. One reveals an ascending top surface (Figure 55), the so-called ramp shape. The height slightly increases in SSA direction. This effect is independent of the gas flux direction but depends on the patterning direction as it can be shown in the rotated SP experiments (4.1.3.1) where the higher part of the ramp always shows up at the last scanning line. Therefore, the ramp is (similar to the tunnel shape) a patterning induced shape effect.
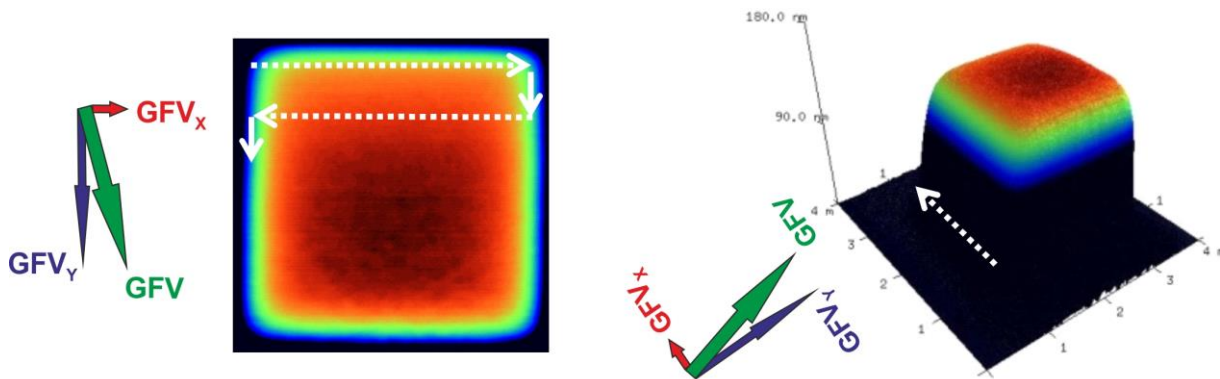

Figure 55: ramp shape. Height image of a serpentine deposit (left) with DT 1000 µs, single pass, 6300 pA and 5 keV. Right: associated 3D-image. The dotted white lines indicate FSA, the solid line the SSA. The dark area within the deposit shows the greater height.

For the ramp effect we suggest an explanation, which differs to the theories above. In contrast, here the working regime plays a minor role; the shape-forming factor is the increased number FSE in combination with a fully covered surface. The electron dose per patterning point generates a relatively high initial deposition, where the replenishment is fully governed by the deposit related replenishment in the proximity of the patterning point (4.1.8.1, Figure 42). During growth, many electrons are forward scattered onto the patterning footprint. As the electron beam has not irradiated these areas yet, they are fully covered with precursor molecules and material is deposited there. Therefore, consecutive patterning lines already start at a higher base level than former ones and finally an ascending shape in FSA direction is revealed.

4.2.3.5   Balanced

For a mid range of parameters (see Figure 56) a relatively flat surface is revealed. This desired shape is only achieved, if the working regimes are equal for each patterning point. The designation "balanced shape" reflects this balanced working regime situation.

This balanced ratio between impinging electrons and precursor coverage/replenishment also coincide with the SO experiments and their resulting estimations given above (Figure 44). Therefore, it is recommended, to use the very critical and sensitive SO strategy to find a good set of parameters and apply these settings to the more advantageous serpentine strategy afterwards.
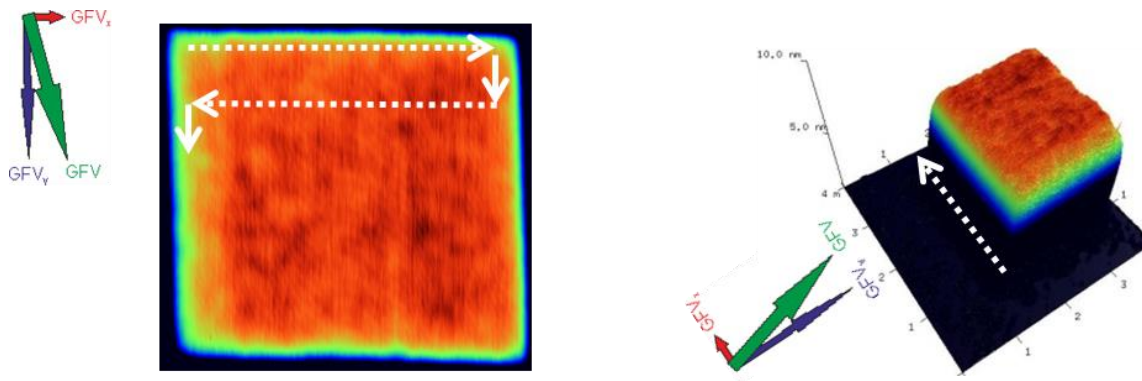
Figure 56: balanced shape. Height image of a serpentine deposit (left) with DT 50 µs, single pass, 25 pA and 5 keV. Right: associated 3D-image. The dotted white lines indicate FSA, the solid line the SSA. The top surface shows no morphological instabilities. The surface shown above seems fairly rough, however please note the very low height scale (10 nm), so in reality the morphology and roughness is quite perfect.

4.2.3.6   Summary: intrinsic surface characteristics

By varying the process parameters dwell time and beam current, 4 distinctive surface topologies were found (4.2.3.1): bowl, tunnel, ramp and balanced shape. All other morphologies have to deal with an inhomogeneity of the precursor coverage during the patterning process and show therefore different heights on the top surface: **1)** bowl shapes (4.2.3.2) arise from the enhanced surface diffusion replenishment at the edges and corners and appears for short dwell times and low currents. **2)** tunnel shapes (4.2.3.3) are caused by different refresh times for patterning points within a scan line and appears for short dwell times and high currents. This morphology is asymmetric and depends therefore on the patterning direction. **3)** ramp morphologies (4.2.3.4) are found for high dwell times and high currents (MTL) and are explained by forward scattered electrons onto a fully filled deposition footprint. **4)** when the precursor coverage is kept constant for all patterning points, the balanced shape is achieved (4.2.3.5). The parameter range for this desired shape, however, is found for intermediate dwell times (shown in Figure 52) which complicates the optimization as simple straightforward maximization / minimization of process parameters can not be used to achieve ideal shapes.

Compensation for the unwanted broadening is possible but still limited which is mainly because the used electron beam is not infinitely small. Hence, the base broadening is unavoidable and can be only corrected by using slightly smaller patterning footprints. Nevertheless, it should be kept in mind that the related broadening shows strongly decaying heights and is found in the range of maximum 20 – 30 nm laterally.

In contrast, the top edge / corner rounding can be compensated by dynamic variation of exposure times at edge / corner regions which clearly improves the finally achievable shape performance. By that this part of the thesis helps to improve the ultimate performance of FEBID based nanofabrication.

4.2.4 Summary: directional gas flux

In short conclusion, we have demonstrated four effects which influences the deposit morphologies on the nanoscale:

1. **Directional gas flux effects**: this effect gets dominating when a geometrical shadow region is induced during growth which changes the replenishment rates on different deposit sites. The result are varying growth rates and morphological instabilities which might also lead to chemical variations and by that to different functionalities on different deposit areas → **avoidable**

2. **Surface bending**: induced by scanning strategies and its entailed variation in surface coverage. It could be shown that all effects can be classified into four different shapes: bowl, tunnel, ramp and balanced → **avoidable**

3. **Top edge / corner rounding**: this effect originates from laterally varying electron re-emission (BSE and SE_2) due to varying number of contributing neighbours → **compensable**

4. **Base broadening**: caused by the non-zero electron beam diameter leading to deposit broadening according to the beam tails → **unavoidable but minimizable**

Beside the identification of the mentioned effects, different strategy guides (directional gas flux and surface bending) and compensation approaches (top edge / corner rounding and base broadening) has successfully been introduced. As the future potential of FEBID depends not only on novel applications and controlled functionalities but also on the reproducibility during nanofabrication, the results found in this master theses represents an essential step forward towards the intrinsic limitations of FEBID based processes.

4.3 Freestanding 3D structuring

From the last chapter we gathered deeper insights in the deposition process and the fundamental influence of the gas dynamics on the shape performance (4.1 and 4.2). Using this knowledge we can proceed to more complex structures.

With the FEBID process it is also possible to fabricate deposits that take off the surface so they get free standing[55] (4.3.1). These filigree 3D-structures are of high interest for possible applications for e.g. resonator concepts to detect gases. Latter is topic of a current master thesis done by Martin Stermitz[56] at the FELMI.[46] Also further devices (e.g. nano-coils, antennas, electron emitters) are under consideration for future work.

In contrast to other techniques, the fabrication via FEBID can be done within a single step on selective positions. To exploit the full potential (e.g. high aspect ratios, features size on nanoscale) the need of an enhanced beam/parameter/working regime-control is absolutely necessary. Based on the findings in chapters 4.1 and 4.2 and intensive work on full beam control via stream files (3.4.1) we will show in the following the challenges (4.3.2), the workarounds for a appropriate set of parameters (4.3.2.3) and some representative nano-architectures (4.3.3) to indicate the possibilities.

4.3.1 Principle

In principle it is quite simple to fabricate freestanding FEBID-structures as schematically shown in Figure 57. After the exposure of one patterning point for a certain dwell time the beam is shifted for a short distance (**PoP**). If the dwell time is long enough and the point pitch not too large, the following deposits build up on the corners of the previous point and the consecutive points lift off the surface.
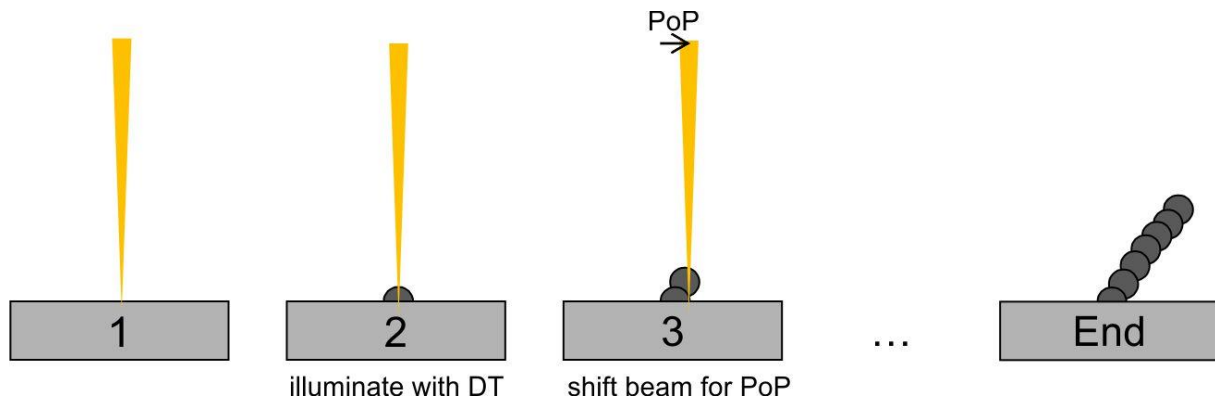

Figure 57: how to fabricate freestanding FEBID-structures.

As it has been shown in 4.1.2.1, the supply with precursor molecules gets more difficult when height increases due to decreasing diffusion from the surface. At a certain height, the replenishment is fully supported by adsorption of precursor molecules close to the tip of the deposit. To get stable deposition conditions even at high structures one has to take care of the appropriate working regime. The resulting pillar diameter depends on beam- and patterning parameter. Diameters smaller than 50 nm have successfully been demonstrated as will be shown below.

4.3.2 Parameter optimization

The principle for freestanding FEBID structures, as discussed above, sounds quite simple. However, the process window to achieve the desired shapes is quite narrow. The take off angles of the deposits sensitively depends on the working regime, so one has to carefully combine primary energy, beam current, dwell time and point pitch as well (4.3.2.1 and **Fehler! Verweisquelle konnte nicht gefunden werden.**).[19] In section 4.3.2.3 we will present a procedure to optimize these parameters in a comfortable way.

4.3.2.1 *Beam energy and number of electrons*

We start the parameter optimization considering the primary energy of the electrons followed by the number of electrons (beam current).

A) beam energy:

When using high acceleration voltages the average penetration depth (Z value of the interaction volume) is much larger than the thickness of the deposited horizontal bars (see also Figure 4). Therefore, many electrons leave the thin bars again at the downside, hit the surface (which is fully loaded with precursor molecules) and lead there to an unwanted deposition (Figure 58, left). Also forward scattered electrons contaminate the surrounding surface[55]

Therefore, high electron energies seem to be disadvantageous and we have to work low primary energies. Figure 58 shows a comparison between the interaction volume for high beam energies (30 kV, left) and for low beam energies (5 kV, right) within an assumed horizontal deposition bar of 80 nm.

Pre-experiments revealed that using 5 keV represents a good compromise between small interaction volumes and high efficiencies. Hence, unless otherwise stated, all experiments have been performed with a primary electron energy of 5 keV at varying beam currents.
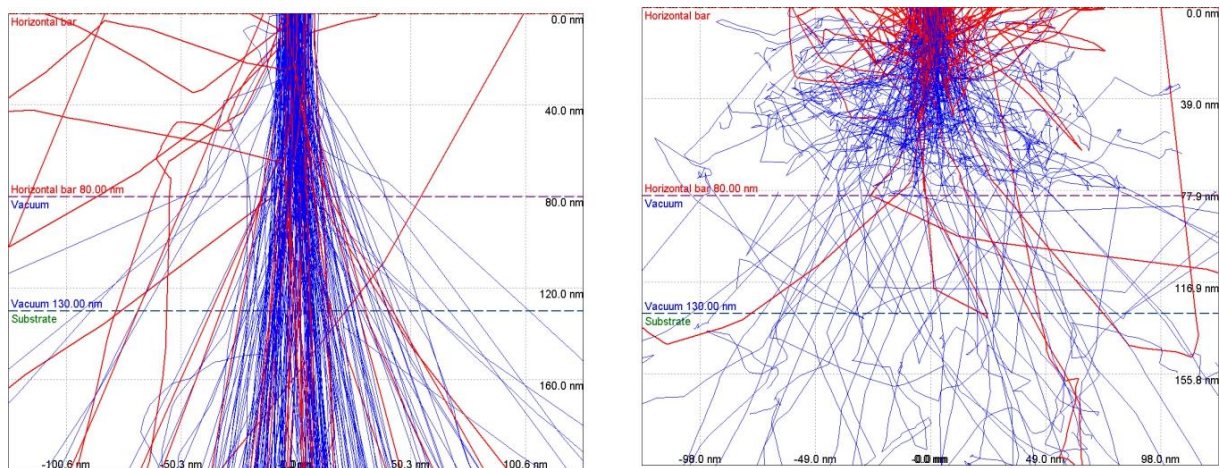

Figure 58: Monte Carlo simulation[12] of electron trajectories through a horizontal bar (deposit material: PtC$_5$) for different acceleration voltages 30 kV (left) and 5 kV (right). Please note, that almost all electrons can leave a deposit with a thickness of 80 nm again for 30 kV, while for 5 kV the majority is located within the deposit. The red trajectories belong to BSE, the blue trajectories to PE.

B) number of electrons:

In order to maintain a constant working regime, the appropriate selection of the beam current is crucial. Two different approaches are possible: *1)* eliminate diffusive component by dissociation of nearly every precursor molecule that is attached close to the deposit site (strongly MTL-regime); *2)* keep a constant ratio between diffusive replenishment and irradiative depletion. High currents lead to case 1 with the disadvantage that many electrons leave the intended deposition and lead to unwanted dissociation on the substrate surface (Figure 59 left). If the current is too low, the volume

growth rate is poor and therefore the duration for one structure rather long which entails drift problems. Good results were achieved for a primary energy of 5 keV and beam currents of 5 pA (Figure 59 right).
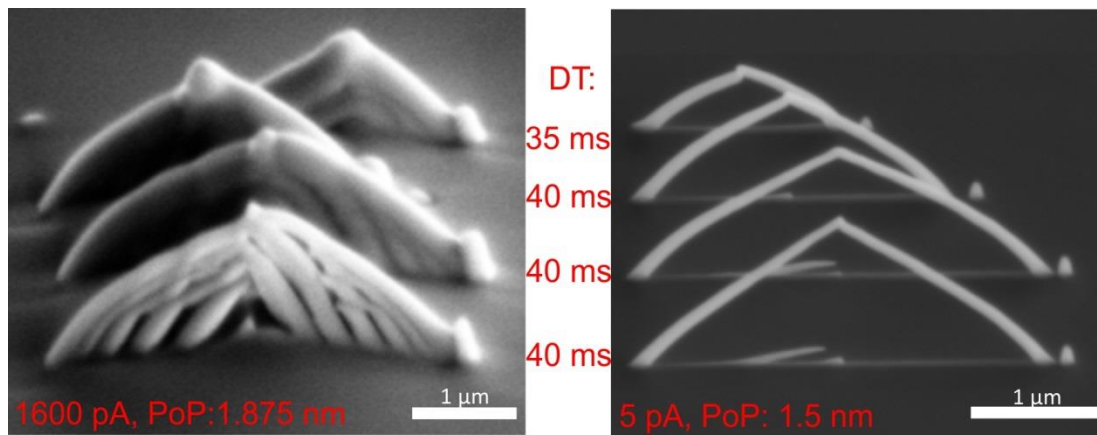

Figure 59: bridges with 5 keV primary voltage; left: current 1600 pA; right: 5 pA. It gets obvious, that the thickness of the branches depends on the beam current.

4.3.2.2   Writing speed

After some rough pre-tests concerning beam voltage and beam current (5 keV and 5 pA respectively were chosen), the next task was to examine the writing speed or patterning velocity. The velocity consists of two independent selectable parameters: *1)* point pitch PoP and *2)* dwell time DT. If the point pitch is too high and/or the dwell time too short, the horizontal bar breaks down or cannot even develop. On the other hand, if the patterning velocity is too small, the angle to the surface gets steeper. In addition, long dwell times slightly broadens the deposited bar. Figure 60 shows 16 diving boards (see page 30) with different combinations of PoPs (0.5, 1, 1.5 and 2 nm) and DTs (20, 40, 60 and 80 ms).
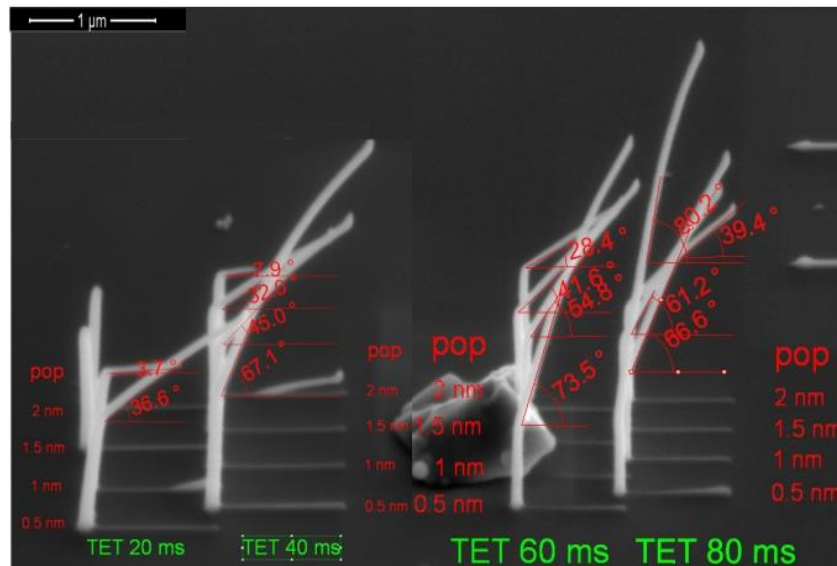
Figure 60: SEM-image of pre-tests with varying PoP and dwell time to examine the correlation between angle and writing speed.
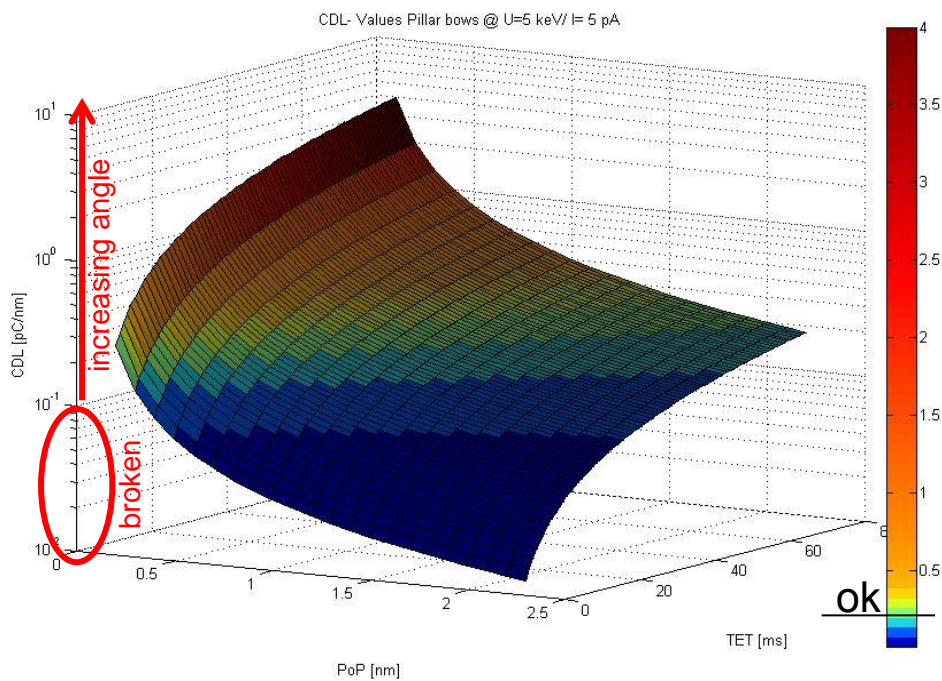

Figure 61: CDL-plot arising from experiments with diving boards. The current is 5 pA, the acceleration voltage 5 keV. To achieve a horizontal bar with a low take off angle only a small parameter range is possible. For this the point pitch (PoP) and the total exposure time (TET) have to be coordinated with each other at a given beam current.

Evaluating the angles in several similar experiments, a small range of parameters was found, where the horizontal bar was not broken, but not too steep either. In the literature the patterning speed is connected with the beam current which leads to the so-called **CDL**-value (charge deposited per unit length)[17]

$$CDL = \frac{beam\ current}{patterning\ velocity} = \frac{beam\ current * dwell\ time}{point\ pitch}$$

In Figure 61, the CDL values are plotted versus the main parameters PoP and DT including an indication where the structures are still intact or broken. It becomes also evident how finest process parameters (see PoP values) influences the CDL behaviour which makes the demand for a very careful parameter adaption very obvious as described in detail in the following.

4.3.2.3 Fine tuning of parameters

Even with a careful beam and stage alignment (lens errors, eucentric height, GIS alignment, …) it is sometimes impossible to fully reproduce same angles with same parameters (e.g. due to changing gas and chamber pressure). Based on the common used parameter for beam current (5 pA), primary electron energy (5 keV) and a point pitch of 1 nm, a sweep for the dwell time is performed.

For this purpose, the "diving board" strategy is beneficial (see 3.4.1.6). The following procedure is proposed:

A) Generate several stream files using the strategy "diving board" with different dwell time for the horizontal bar in the expected parameter range.
B) Load the stream files, start the deposition process and follow the current through the specimen (end point monitor graph).
C) The resulting shape of the diving board and therefor the optimal dwell time can be directly determined by watching evolution in the end point monitor which measures the electrical current through the specimen.

As shown in Figure 62 left, the dwell time of 10 ms and 11 ms were too short for developing a horizontal bar and a line on the surface has been deposited instead. In the according end point monitor graph (Figure 62 right) a strong increase of resistance appears while the vertical pillar is developing until a constant level is reached. When the beam spot shifts to the first patterning points of the horizontal bar, the primary electrons impact on the surface and the resistivity falls to its minimum level again.

For a dwell time of 12 and 13 ms, the horizontal bar has started to develop, but broke too early (Figure 62). For a dwell time of 14 ms the horizontal bar has developed, in the end point monitor graph the current does not fall to the minimum level immediately. An analogue behaviour is observed for higher dwell times.
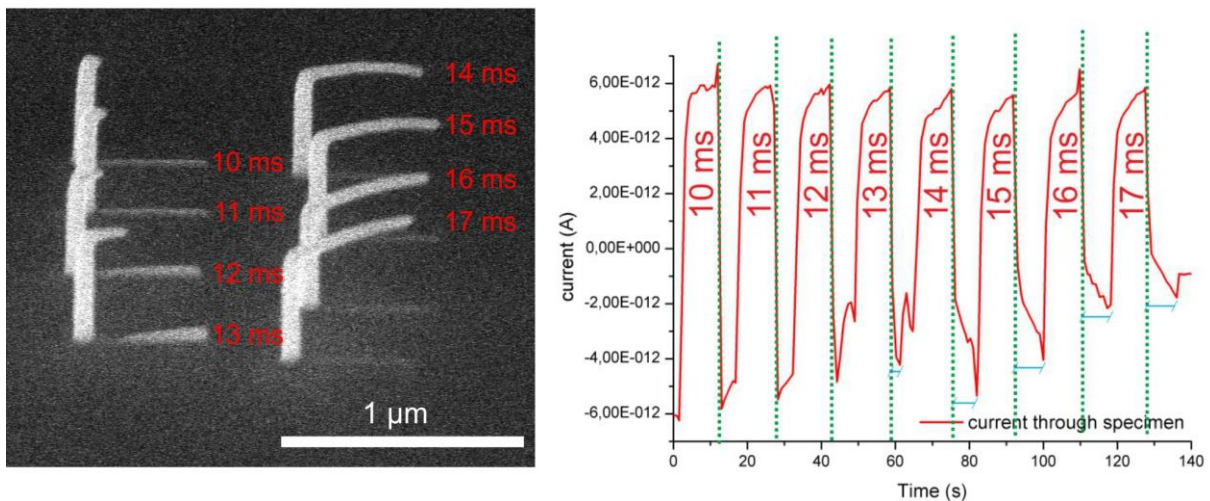
Figure 62: diving board procedure to find appropriate set of parameter. Left: Set of diving boards with variable dwell times for horizontal structuring. PoP = 1 nm; U = 5 keV, I = 5 pA. Right: Associated end point monitor graph. The dotted green lines indicate the moment, when the pillar is finished and a horizontal movement of the electron beam starts. If no horizontal deposit develops, the current through the specimen immediately falls to the base level (10-12 ms). If the resistivity stays on a higher level, a branch was built (13-17 ms). The length of the blue bar reflects the fabrication time of a horizontal structure. As it can be seen for 13 ms, the length of the blue bar is shorter which coincides with the shorter length of the horizontal branch in the SEM-micrograph on the left.

The position of the minimum level (= maximum current through specimen) indicates, whether the structure has been broken or not. If the minimum peak is shifted (see blue markers in Figure 62 right) the selected dwell time is sufficient to develop a horizontal structure. With this method, the user is able to see in the point monitor graph directly the correct dwell time for his experiments. Please note, thinnest and flattest angles can be achieved by using the lowest possible dwell time. However, structures with longer dwell times are more robust and should be applied for higher architectures.

4.3.3 Some examples

As described in 3.4.1 a lot of effort was placed on the optimization of the beam motion for customized purposes. For that reason the several strategies (single pillar, diving board, T, bridge, bridge with antenna, circle and circle on pillars; see 3.4.1.6) have been generated. Due to replenishment and drift problems for tall features the alternating point sequence was introduced. Figure 63 to Figure 73 show some examples of FEBID-based nano-architectures, the utilized strategies are listed in the respective figure caption. Please note, fragile pillars are bended by an imaging electron beam, as indicated in the insert of Figure 70. The efforts have finally led to a software package which allows to generate according streamfiles for direct fabrication of the mentioned structures as they represent the main shapes of interest at the moment with respect to optical applications, electron emitters and free standing sensor concepts.
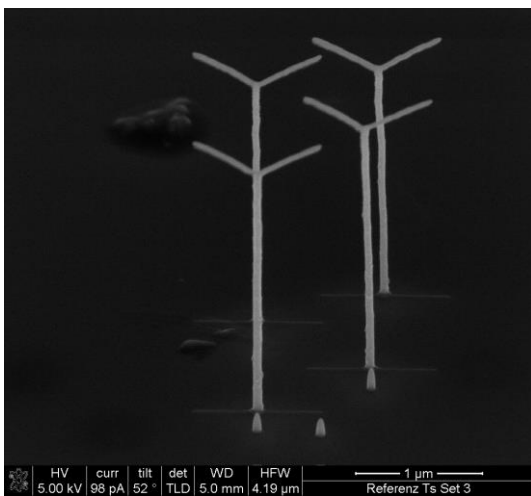

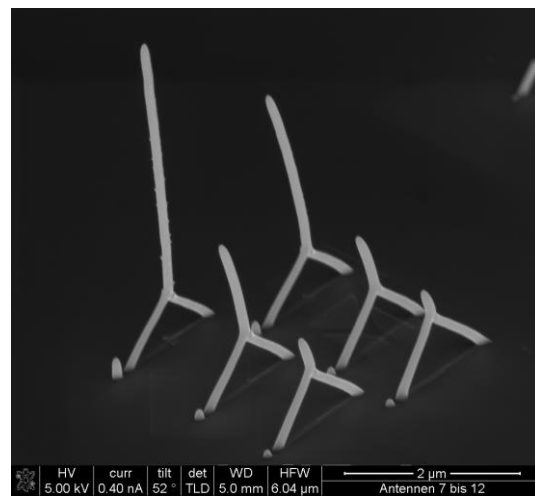**Figure 63: antennas with different dwell times (14 -17 ms). Fabrication with "T"- strategy.**

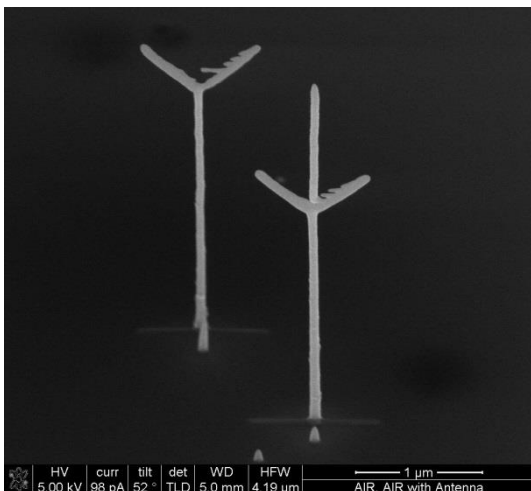**Figure 65: antennas using strategy "multiple bridges with antenna".**

Figure 64: "fork"-antennas, fabricated with T-strategy and single pillar.

Figure 66: antennas fabricated with T and bridge strategies.

Figure 67: institute logo. F: two diving boards, E: single line and two diving boards, L: single line and pillar, M: two bridges, I: single pillar.

Figure 69: lassos with radii 500 nm and 1 µm respectively. Fabricated with pillar bow strategies and single pillar (center).
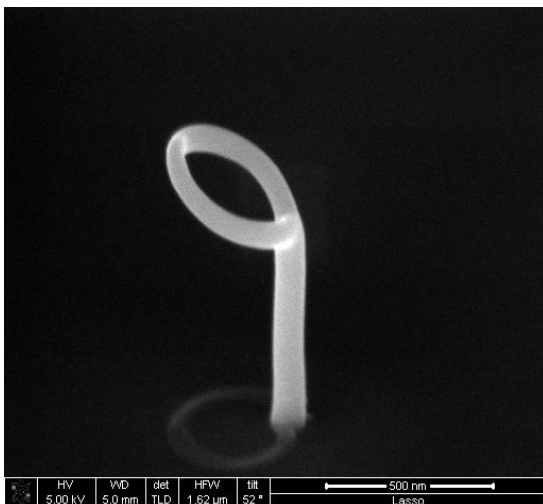

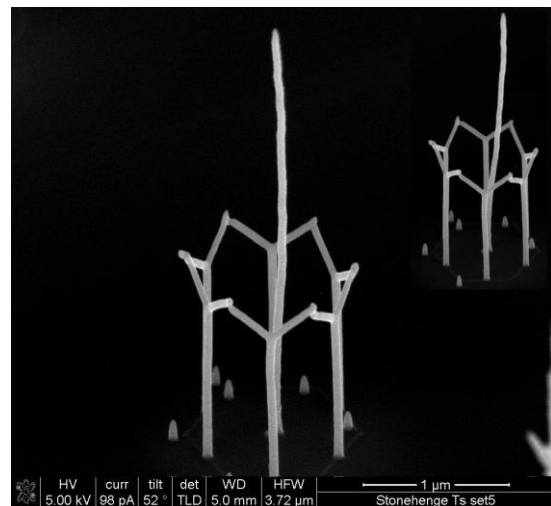**Figure 68: small Lasso: Fabrication with "pillar bow"-strategy with radius of 150 nm.**

Figure 70: nanoarchitecture consisting of 6 "T" and a single pillar. Long pillars are bended by the electron beam very easily as shown in the insert top right.
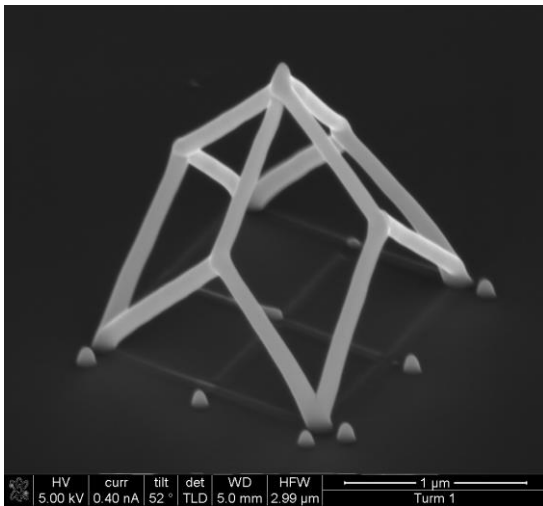
Figure 71: nano-cage consisting of 6 bridges. The arrangement of these 6 bridges can be seen at the surface, where electrons have penetrated the branches.
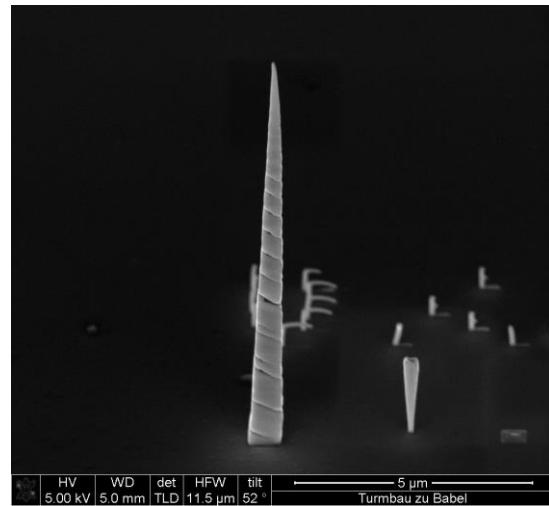
Figure 72: hollow tower (left front) and nozzle (right front): these structures have been fabricated with spiral-in and spiral-out strategy respectively. The footprint is a square as shown in the right corner.
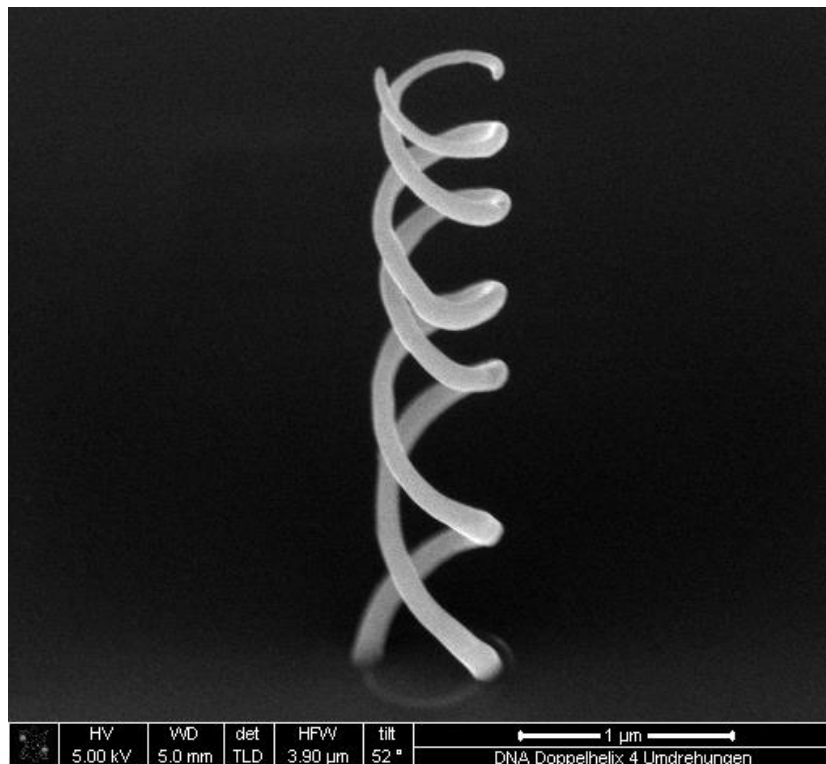
Figure 73: double Helix: in contrast to the other structures shown before, the patterning sequence of the original stream file (circle strategy with 3 turns) has been manipulated. A second circle (B) starts on the opposite side of the circle, the electron beam jumps alternating between circle A and B.

5   Summary and Outlook

Main aim of this master thesis was to investigate the influence of precursor dynamics on the morphology of functional (nano)structures during focused electron beam induced deposition (**FEBID**) using MeCpPt^{IV}Me$_3$ precursor. As could be shown, the molecular gas flux, surface diffusion, process parameters and patterning strategies imply different growth modes leading to morphological deviations from the intended shape.

In a first step it was shown via simulations and experiments that the molecular adsorption rate is strongly site dependent. Based on these primary investigations, a gas flux vector was defined for convenient description of the preferred gas flux direction with respect to the growing deposit. Systematic investigations of varying patterning directions revealed the existence of a geometrical shadowing effect caused by the growing deposit itself which can be understood as morphological barrier. The astonishing result of these investigations was the fact that these effects seem to occur even for deposit height of less than 50 nm.

Adapted scan routines (spiral-out, spiral-in, and interlacing) in combination with switched off gas flux allowed decoupling of gas-flux and surface-diffusion related influences. As a result, the latter effect could be proven to be of minor relevance which allows assignment of the directional gas flux together with the shadowing effect as key issue for the disrupted morphologies. In more detail, the problems occur due to incompletely replenished areas which changes local growth rates. Furthermore, this varying degree of coverage is inhomogeneously distributed across the pattern and depends on the patterning directions with respect to the gas flux vector. To verify this complex interplay which is dynamically changing, according finite difference simulations have been performed together with our collaboration partners (Oak Ridge National Labs; University of Tennessee, TN, USA) were found in excellent agreement with experimental results, further supporting the proposed growth model.

Based on these results, specific experiments have been designed to establish a laterally constant replenishment situation. By that it could be shown that the effect can be compensated by proper adaption of process parameters and patterning strategies to eliminated gas flux related anisotropies.

Although the most striking effects have been eliminated during the first step, a closer look to the deposit shape revealed further deviations on the nanoscale which can be a knock-out criteria for high resolution applications. In this second step we could identify two fundamental effects: *1)* a broadening of the deposit base; and *2)* a rounding effect of edges and corners on top of the structures. While the former is found to be unavoidable but minimizable, the second effect could successfully be suppressed by the introduction of a smart patterning adaption.

Apart from optimized bases, edges and corners, the deposit flatness on top have been investigated as third step in this master thesis. Similar to the gas flux related problems, different surface shapes can appear in dependency on patterning sequence and process parameters. But even for the most favourable scan strategy (serpentine) four different surface shapes could be found: *i)* bowl; *ii)* tunnel; *iii)* ramp and *iv)* balanced (flat). All growth modes can be explained by site specific variation of the precursor-to-electron ratio which can be tuned via carful process parameters adaption. Therefore, it was possible to demonstrate the existence of a stable regime where gas flux related influences are

eliminated (laterally homogeneous morphologies), surfaces are extremely flat (sub 1-nm roughness), and edges /corners reveal high-fidelity characteristics. In order to simplify the optimization, combined software package are planned as future work on the FELMI.

As a final step, the gained knowledge about the precursor surface dynamics and its influences on final deposits was used to focus on the critical fabrication of freestanding 3D-nanostructures, as FEBID is one of the very few techniques which allow such architectures in a straightforward manner. It is successfully demonstrated that 3D structures with diameters down to 50 nm can be fabricated in a direct-write manner which enables new types of applications such as 3D nano-photonics or free standing sensor concepts. Current joint efforts with our collaboration partners are focused on the development of patterning generators which allow straightforward fabrication of very complex structures based on our base work presented in this study.

In summary, this thesis represents an essential step forward by investigating the influence of molecular gas flux effects which has widely been ignored in the past. By that it was possible to unravel the origins of unstable growth rates or disrupted morphologies of observed before. Together with the demonstrated 3D possibilities, the content of this thesis improved the fundamental understanding of FEBID processes and pushed this technique a further step towards its full capabilities.

References

1. van Dorp WF, Hagen CW, Crozier PA, van Someren B, Kruit P. One nanometer structure fabrication using electron beam induced deposition. *Microelectron Eng*. 2006;83(4-9 SPEC. ISS.):1468-1470.

2. Van Dorp WF. The role of electron scattering in electron-induced surface chemistry. *Phys Chem Chem Phys*. 2012;14(48):16753-16759.

3. Perentes A, Bachmann A, Leutenegger M, Utke I, Sandu C, Hoffmann P. Focused electron beam induced deposition of a periodic transparent nano-optic pattern. *Microelectron Eng*. 2004;73-74:412-416.

4. Kolb F, Schmoltner K, Huth M, et al. Variable tunneling barriers in FEBID based PtC metal-matrix nanocomposites as a transducing element for humidity sensing. *Nanotechnology*. 2013;24(30).

5. Plank H, Haber T, Gspan C, Kothleitner G, Hofer F. Chemical tuning of PtC nanostructures fabricated via focused electron beam induced deposition. *Nanotechnology*. 2013;24(17).

6. Master Thesis by DI Roland Schmied, Institute for Electron Microscopy, Graz University of Technology, 2011.

7. Goldstein J, Newbury D, Joy DC, et al. *Scanning electron microscopy and X-ray microanalysis.* 3rd Edition ed. New York: Springer Scienes+Business Media, Inc.; 2003.

8. Leng Y. Materials characterization: Introduction to microscopic and spectroscopic methods. *Mater Charact : Introd to Microsc and Spectrosc Methods*. 2010.

9. George GS. *Engeneering physics.* Pune: Techn. Publ. Pune; 2007.

10. Private communication with FEI.

11. Satoh H, Kawata S, Nakane H, Adachi H. Studies on the ZrO/W(100) surface by means of low-energy electron diffraction and X-ray photoelectron spectroscopy. *Surf Sci*. 1998;400(1-3):375-382.

12. Drouin D, Couture AR, Joly D, Tastet X, Aimez V, Gauvin R. CASINO V2.42 - A fast and easy-to-use modeling tool for scanning electron microscopy and microanalysis users. *Scanning*. 2007;29(3):92-101.

13. Reimer L. *Scanning electron microscopy: Physics of image formation and microanalysis.* Vol 45. 2 completely rev a updat ed. Berlin ; New York: Springer; 1998:527. http://www.loc.gov/catdir/enhancements/fy0812/98026178-d.html.

14. García, R. C. Amplitude modulation atomic force microscopy, Weinheim, Chichester: Wiley-VCH, John Wiley 2.

15. Courtesy of Dr. Harald Plank, Institute for Electron Microscopy and Nanoanalysis, Graz University of Technology, Austria, 2013.

16. Godehardt R, Lebek W, Adhikari R, et al. Optimum topographical and morphological information in AFM tapping mode investigation of multicomponent polyethylene. *Eur Polym J*. 2004;40(5):917-926.

17. Utke I, Russel PE. *Nanofabrication using focused ion and electron beams: Principles and applications.* 1st ed. New York: Oxford University Press; 2012:840.

18. Engmann S, Stano M, Papp P, Brunger MJ, Matejcík Š, Ingólfsson O. Absolute cross sections for dissociative electron attachment and dissociative ionization of cobalt tricarbonyl nitrosyl in the energy range from 0 eV to 140 eV. *J Chem Phys*. 2013;138(4).

19. Utke I, Hoffmann P, Melngailis J. Gas-assisted focused electron beam and ion beam processing and fabrication. *J Vac Sci Technol B Microelectron Nanometer Struct*. 2008;26(4):1197-1276.

20. Smith DA, Fowlkes JD, Rack PD. Understanding the kinetics and nanoscale morphology of electron-beam- induced deposition via a three-dimensional monte carlo simulation: The effects of the precursor molecule and the deposited material. *Small*. 2008;4(9):1382-1389.

21. Fowlkes JD, Rack PD. Fundamental electron-precursor-solid interactions derived from time-dependent electron-beam-induced deposition simulations and experiments. *ACS Nano*. 2010;4(3):1619-1629.

22. Szkudlarek A, Gabureac M, Utke I. Determination of the surface diffusion coefficient and the residence time of adsorbates via local focused electron beam induced chemical vapour deposition. *J Nanosci Nanotechnol*. 2011;11(9):8074-8078.

23. Porrati F, Sachser R, Schwalb CH, Frangakis AS, Huth M. Tuning the electrical conductivity of pt-containing granular metals by postgrowth electron irradiation. *J Appl Phys*. 2011;109(6).

24. Miyazoe H, Utke I, Kikuchi H, et al. Improving the metallic content of focused electron beam-induced deposits by a scanning electron microscope integrated hydrogen-argon microplasma generator. *J Vac Sci Technol B Microelectron Nanometer Struct*. 2010;28(4):744-750.

25. Roberts NA, Fowlkes JD, Magel GA, Rack PD. Enhanced material purity and resolution via synchronized laser assisted electron beam induced deposition of platinum. *Nanoscale*. 2013;5(1):408-415.

26. Mulders JJL, Belova LM, Riazanova A. Electron beam induced deposition at elevated temperatures: Compositional changes and purity improvement. *Nanotechnology*. 2011;22(5).

27. Utke I, Friedli V, Purrucker M, Michler J. Resolution in focused electron- and ion-beam induced processing. *J Vac Sci Technol B Microelectron Nanometer Struct*. 2007;25(6):2219-2223.

28. Lassiter MG, Liang T, Rack PD. Inhibiting spontaneous etching of nanoscale electron beam induced etching features: Solutions for nanoscale repair of extreme ultraviolet lithography masks. *J Vac Sci Technol B Microelectron Nanometer Struct*. 2008;26(3):963-967.

29. Liang T, Frendberg E, Lieberman B, Stivers A. Advanced photolithographic mask repair using electron beams. *J Vac Sci Technol B Microelectron Nanometer Struct*. 2005;23(6):3101-3105.

30. Roberts NA, Noh JH, Lassiter MG, Guo S, Kalinin SV, Rack PD. Synthesis and electroplating of high resolution insulated carbon nanotube scanning probes for imaging in liquid solutions. *Nanotechnology*. 2012;23(14).

31. Utke I, Hoffmann P, Berger R, Scandella L. High-resolution magnetic co supertips grown by a focused electron beam. *Appl Phys Lett*. 2002;80(25):4792-4794.

32. Utke I, Jenke MG, Röling C, et al. Polarisation stabilisation of vertical cavity surface emitting lasers by minimally invasive focused electron beam triggered chemistry. *Nanoscale*. 2011;3(7):2718-2722.

33. Huth M, Porrati F, Schwalb C, et al. Focused electron beam induced deposition: A perspective. *Beilstein J Nanotechnology*. 2012;3(1):597-619.

34. Fernández-Pacheco A, De Teresa JM, Córdoba R, et al. Domain wall conduit behavior in cobalt nanowires grown by focused electron beam induced deposition. *Appl Phys Lett*. 2009;94(19).

35. Serrano-Ramón L, Córdoba R, Rodríguez LA, et al. Ultrasmall functional ferromagnetic nanostructures grown by focused electron-beam-induced deposition. *ACS Nano*. 2011;5(10):7781-7787.

36. Gavagnin M, Wanzenboeck HD, Belic D, Bertagnolli E. Synthesis of individually tuned nanomagnets for nanomagnet logic by direct write focused electron beam induced deposition. *ACS Nano*. 2013;7(1):777-784.

37. Gabureac MS, Bernau L, Boero G, Utke I. Single superparamagnetic bead detection and direct tracing of bead position using novel nanocomposite nano-hall sensors. *IEEE Trans Nanotechnol*. 2013;12(5):668-673.

38. Friedli V, Utke I. Optimized molecule supply from nozzle-based gas injection systems for focused electron- and ion-beam induced deposition and etching: Simulation and experiment. *J Phys D*. 2009;42(12).

39. Botman A, Mulders JJL, Hagen CW. Creating pure nanostructures from electron-beam-induced deposition using purification techniques: A technology perspective. *Nanotechnology*. 2009;20(37).

40. Plank H, Gspan C, Dienstleder M, Kothleitner G, Hofer F. The influence of beam defocus on volume growth rates for electron beam induced platinum deposition. *Nanotechnology*. 2008;19(48).

41. The FEI Company. Manual FIB Nova 200. Eindhoven, The Netherlands, www.fei.com.

42. The FEI Company. Patterning engine specification. Eindhoven, The Netherlands, www.fei.com.

43. Code::Blocks. Release 10.05 www.codeblocks.org.

44. Courtesy of DI Roland Schmied, Institute for Electron Microscopy and Nanoanalysis, Graz University of Technology, Austria, 2013.

45. Orthacker A, Schmied R, Chernev B, et al. Chemical degradation and morphological instabilities during focused ion beam prototyping of polymers. *Phys Chem Chem Phys*. 2013.

46. Stermitz M, Nau S, Orthacker A, et al. Free standing quasi 1D nanoresonators for sensing applications. *in preparation*. 2014.

47. Friedli V, Utke I2, http://www.empa.ch/GISsimulator.

48. Friedli, V. Focused electron- and ion-beam induced processes: in situ monitoring, analysis and modelling PhD Thesis Ecole Polytechnique F´ed´erale de Lausanne, 2008.

49. Winkler R, Fowlkes J, Szkudlarek A, Utke I, Rack PD, Plank H. The nanoscale implications of a molecular gas beam during electron beam induced deposition. *submitted to ASC Appl Mater Interfaces*. 2013.

50. Van Dorp WF, Hagen CW. A critical literature review of focused electron beam induced deposition. *J Appl Phys*. 2008;104(8).

51. Alkemade PFA, Miro H, Van Veldhoven E, Maas DJ, Smith DA, Rack PD. Pulsed helium ion beam induced deposition: A means to high growth rates. *J Vac Sci Technol B Microelectron Nanometer Struct*. 2011;29(6).

52. Córdoba R, Baturina TI, Sesé J, et al. Magnetic field-induced dissipation-free state in superconducting nanostructures. *Nat Commun*. 2013;4.

53. Arnold G, Timilsina R, Fowlkes J, et al. Fundamental resolution limitations during electron induced direct write synthesis. *submitted to ACS Nano*. 2014.

54. Demers H, Poirier-Demers N, Couture AR, et al. Three-dimensional electron microscopy simulation with the CASINO monte carlo software. *Scanning*. 2011;33(3):135-146.

55. Bret T, Utke I, Hoffmann P, Abourida M, Doppelt P. Electron range effects in focused electron beam induced
deposition of 3D nanostructures. *Microelect Eng*. 2006;83:1482-1486.

56. Master Thesis by DI Martin Stermitz, Institute for Electron Microscopy, Graz University of Technology, 2014. .